Destruction and Defluorination of Ultrashort-Chain and Short-Chain Perfluoroalkyl Substances in Continuous Flow Alkaline Hydrolysis

Kinetics, Product Distributions, and the Mechanistic Origin of Incomplete Defluorination

Anmol Laxmankumar Purohit

A dissertation submitted in partial fulfillment of the requirements for the degree of

Doctor of Philosophy

University of Washington

2026

Reading Committee:

Igor Novosselov, Chair
John Kramlich
Brian Pinkard

Program Authorized to Offer Degree:

Mechanical Engineering

University of Washington

Destruction and Defluorination of Ultrashort-Chain and Short-Chain Perfluoroalkyl Substances by Alkaline Hydrolysis

Anmol Laxmankumar Purohit

Chair of the Supervisory Committee: Professor Igor Novosselov
Department of Mechanical Engineering

Abstract

Per- and polyfluoroalkyl substances persist in the environment due to the strength of the carbon-fluorine bond; in particular, ultrashort- and short-chain species are hardest to treat because of their high mobility, as they cannot be captured by most conventional methods. This dissertation examines the end-of-life treatment of three such compounds, C-1 trifluoromethanesulfonic acid (TFMS), C-3 perfluoropropanoic acid (PFPrA), and C-4 perfluorobutanoic acid (PFBA), under a high-temperature, alkaline environment in a continuous-flow reactor. The dissertation describes mechanistic insights and an evaluation of differences in their destruction and defluorination.

For TFMS, two expanded operating regimes were developed that utilize phase transition of the subcritical water rather than increasing the hydroxide concentration, to enhance destruction and defluorination. (i) Superheated ionically modulated alkaline hydrolysis (SIM-AH) raises the critical point of pure water (374 °C and 22.1 MPa) by electrolyte amendment, e.g., to 406.6 °C and 29.7 MPa with 3 wt% NaCl. (ii) Distillation alkaline hydrolysis (DAH) uses high-temperature, low-pressure operation to force phase separation, concentrating alkali in the liquid/brine phase. SIM-AH reached above 99.9% destruction of TFMS at 2 M NaOH and DAH at 0.5 M NaOH whereas conventional alkaline hydrolysis requires 5 M NaOH to achieve similar destruction efficiencies. Mechanistic insights were provided by experimental findings and are supported by density functional theory, which identifies heterolytic carbon-sulfur bond cleavage as the rate-

determining step, with a competing thermal pathway that becomes significant only when hydroxide is limited, evidenced by fluoroform detected in the absence of base.

For the two perfluorocarboxylic acids (PFCAs), ultrashort-chain PFPrA and short-chain PFBA, degradation and defluorination are shown to occur sequentially. Parent compound destruction is independent of alkali concentration, exceeding 99.9% by 225 °C for PFBA and PFPrA at every alkali concentration including zero, so the initial scission step is thermally driven. That scission yields volatile fluorinated fragments whose mineralization cannot proceed without hydroxide. The mineralization rate of the volatile fragments relative to the residence time governs defluorination efficiency. Carbon and fluorine balances, gas-phase product identification, and computed elimination barriers inform the pathways and the fate of the decarboxylation product. The three-carbon fragment is re-activated by hydroxide and returns to the degradation cascade, while mineralization of the two-carbon fragment (pentafluoroethane) requires higher activation energy; the computed base-assisted barrier difference between the two fragments is 7.5 kcal/mol.

The experimental and computational analysis suggests that defluorination of these PFCAs is limited not by the degradation of the parent compound but by the mineralization of the reaction byproducts. In both classes, the hydroxide-dependent step sets the limit. For TFMS that step is cleavage of the carbon-sulfur bond; for the PFCAs it is reactivation of the fluorinated fragment, set by the fragment’s elimination barrier.

Table of Contents

List of Figures

List of Tables

Acknowledgments

I am deeply grateful to my advisor, Professor Igor Novosselov, for the opportunity to carry out this work and for his steady support and guidance throughout my time in his lab.

I thank Professor John Kramlich for the courses that laid the foundation of this research and for the teaching assistantships he entrusted to me. I am grateful to Dr. Brian Pinkard for his mentorship, which shaped both this work and my development as a researcher. I also thank Professor Avin Vijay for agreeing to serve as the Graduate School Representative on my committee.

I am grateful to Professor Timothy Strathmann for reviewing my work and for his thoughtful suggestions. I thank Professor Shubham Vyas and Ben Payton for the density functional theory work that strengthened the mechanistic arguments in this dissertation, and Dr. Ji Feng for many valuable brainstorming discussions.

I am thankful to my labmates Stuart Moore, Conrad Austin, Almond Lau, Shuyuan Bai, Holle Lam, Mrityunjai Verma, and Dzaki Pahlevi for their help and camaraderie along the way. I also thank the undergraduate researchers Ameya Kulkarni, Vivaan Kothari, and Sol Badeaux for their assistance and hard work.

Finally, I thank my wife for being by my side throughout this journey, and my parents for their never-ending support.

I wish to remember Professor Philip Malte, who first inspired me to pursue a doctoral degree. He is no longer with us, but his encouragement set me on the path that led to this work, and for that I remain deeply grateful.

Chapter 1: Introduction

1.1 Background and Motivation

Per- and polyfluoroalkyl substances (PFAS) owe their persistence to the carbon-fluorine bond, among the strongest single bonds in organic chemistry. Manufactured since the 1950s and built around that bond, PFAS have become ubiquitous in water, soil, wildlife, and human tissue worldwide, and the same chemical inertness that makes them useful renders them essentially immune to the natural and engineered processes that break down ordinary organic pollutants. [1, 2] They are now regulated in drinking water at the nanogram-per-liter level, yet the technologies that remove them from water, such as sorbents, ion exchange, foam fractionation, and membranes, only concentrate them into residual streams that still require their end-of-life treatment.[3, 4] The central practical problem is therefore not only to separate PFAS from water but to break the carbon-fluorine bonds that make them persistent in the environment, and doing so at a cost and scale that treatment of real waste streams can bear.

This dissertation addresses end-of-life PFAS treatment, and specifically the hydrothermal chemistry in high-pH water. The challenge differs across PFAS families, as chemical routes depend on molecular structure and type of degradation approach. Some of the most recalcitrant compounds are also the least studied, including ultrashort- and short-chain species that dominate current contamination and pass-through conventional treatment.[5, 6] Understanding how such compounds are destroyed is the scientific challenge that this work addresses.

The scale of the problem is what makes it urgent. PFAS have been detected in the majority of tested drinking-water systems, including an estimated 45% of United States tap water.[7] Any technology proposed for the resulting residual stream treatment must therefore do three things: cleave the carbon-fluorine bond completely, yield products that are benign and quantifiable, and

operate at a cost the waste stream can support. Among the available options, alkaline hydrolysis has the potential to meet these requirements.

1.2 Regulatory Landscape and the Need for Destruction

The scientific consensus on PFAS persistence and toxicity has driven increasingly stringent regulation, culminating in the first enforceable United States drinking-water limits for several PFAS in 2024, set in the low ng/L range, see Chapter 2.[4] For the purposes of this introduction, the salient point is a distinction that regulation makes unavoidable: regulation of drinking water creates demand for treatment; however, the "treatment" and end-of-life destruction are not the same thing.

The technologies mostly used to meet regulatory limits separate PFAS from the water stream, e.g., granular activated carbon adsorption, anion exchange, and high-pressure membranes such as reverse osmosis and nanofiltration, rather than destroying them.[3, 8] Foam fractionation, similarly, concentrates PFAS into a small-volume foam concentrate.[9] Each of these separation processes generates a PFAS-laden residual waste, such as spent adsorbent, exhausted resin, membrane reject, or foam concentrate, that still contains the intact fluorinated compounds and therefore still requires a final destruction step.[3] Landfilling and deep-well injection merely relocate the problem, and the designation of certain PFAS as hazardous substances has increased the liability associated with disposal without destruction. As a result, there is an urgent and growing demand for destruction technologies that can mineralize PFAS in these concentrated residual streams at practical scale.[10]

1.3 The Ultrashort- and Short-Chain Challenge

Most treatment and toxicology research to date has focused on the long-chain legacy compounds PFOA and PFOS.[6] However, the phase-out of these compounds drove a shift toward shorter-chain replacements, which were adopted on the assumption that reduced bioaccumulation would make them safer. These shorter compounds present their own problems. Ultrashort-chain PFAS, those

with one or two perfluorinated carbons, are highly soluble in water and adsorb poorly to organic matter and to the activated carbon and ion-exchange media used in conventional treatment, so they break through separation processes that capture their long-chain homologs.[8, 11]

A growing body of monitoring data shows that these compounds are widespread and often present at higher concentrations than longer-chain PFAS. A comprehensive global analysis of more than 3,500 concentration records confirmed that ultrashort-chain perfluoroalkyl acids frequently occur at levels exceeding those of the regulated long-chain compounds, yet they remain largely outside current measurement protocols and regulatory limits.[5] Trifluoroacetic acid (TFA), a C_1 perfluorocarboxylic acid (PFCA), has been detected in precipitation and surface waters on multiple continents at concentrations that have risen steadily over three decades, including in remote Arctic and oceanic systems, demonstrating both long-range atmospheric transport and resistance to natural degradation. [6, 12, 13] Ultrashort-chain PFAS are also frequently the terminal products of the environmental and treatment-plant transformation of larger precursors, which means they accumulate as other PFAS degrade.[5]

The ultrashort- and short-chain PFCAs perfluoropropanoic acid (PFPrA) and perfluorobutanoic acid (PFBA) and the ultrashort-chain perfluorosulfonic acid (PFSA) trifluoromethanesulfonic acid (TFMS) are representative of this understudied group. TFMS, in particular, has been ranked a high-priority contaminant on persistence, mobility, bioaccumulation, and toxicity metrics, with an integrated hazard score exceeding that of PFOS, and it is widely detected in impacted groundwater, in drinking water, and in human tissue.[14] Despite this, few studies have reported the destruction of ultrashort-chain PFAS, and treatment methods effective across the full range of chain lengths are needed.

PFAS comprise thousands of structures, of which the perfluoroalkyl acids treated here are a small subset. Figure 1.1 shows the accepted classification. [15] The first division separates polymers from nonpolymers. The polymeric branch, which includes the fluoropolymers, the side-chain fluorinated polymers, and the perfluoropolyethers, is of limited concern for water treatment because these materials are large, insoluble, and immobile, although their manufacture and degradation can release smaller compounds. The nonpolymeric branch divides again into the polyfluoroalkyl precursors, which are not themselves fully fluorinated but transform in the environment into compounds that are, and the perfluoroalkyl acids, which are the terminal products of those transformations and the compounds that persist.

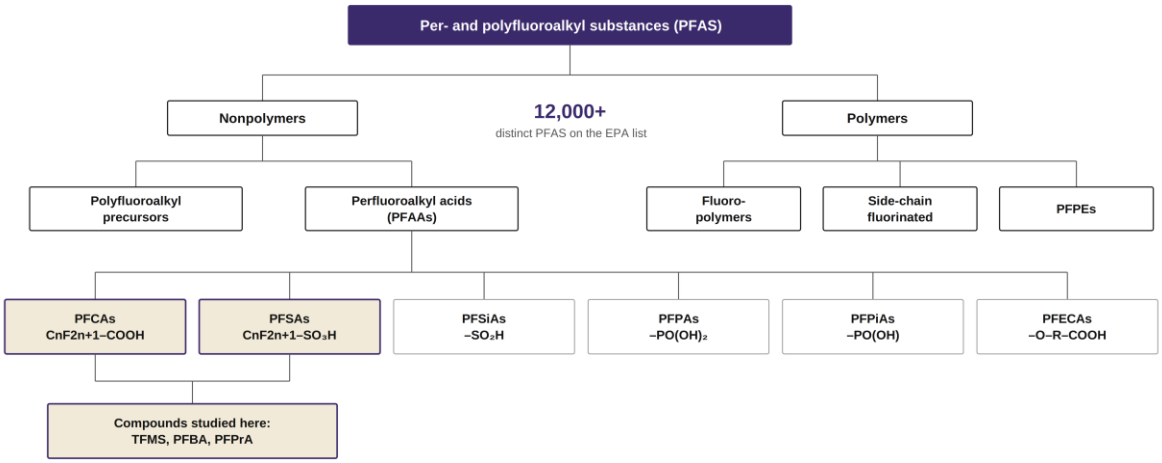

Figure 1.1: Classification of per- and polyfluoroalkyl substances. Shading marks the two perfluoroalkyl acid classes examined in this work, the PFCAs and the PFSAs, from which the three study compounds are drawn. Adapted from ITRC (2022) and Buck et al. (2011). [15, 16]

The perfluoroalkyl acids are subdivided by head group, and six classes are recognized. This dissertation addresses the two that dominate both the regulatory and the occurrence record: the PFCAs, with a carboxylate head group, and the PFSAs, with a sulfonate head group. The three compounds studied here are drawn from these two classes. The distinction matters more than it may appear, because the head group governs the first step of destruction. A carboxylate

decarboxylates readily to give a perfluoroalkyl carbanion, whereas a sulfonate must undergo carbon-sulfur cleavage, and the two routes impose different conditions.

Figure 1.2 sets the perfluoroalkyl acids out by carbon number and by head group, with the PFCAs on the left and the PFSAs on the right.

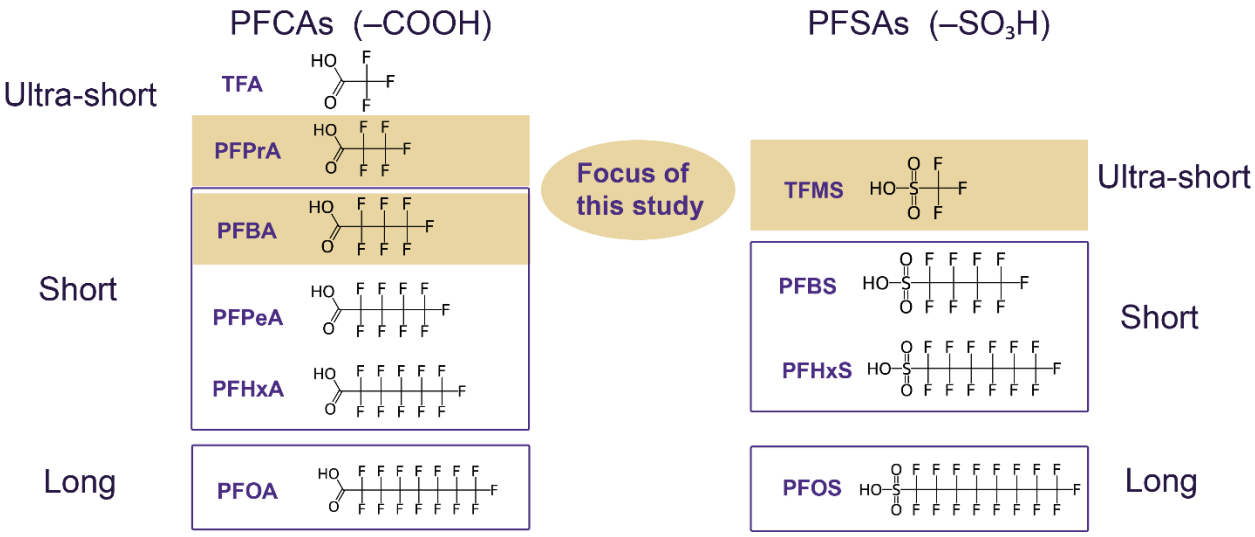

Figure 1.2: Perfluoroalkyl acids classified by chain length, showing PFCAs (head group -COOH) on the left and PFSAs (head group -SO_3H) on the right. The rows group the acids by chain length: ultrashort (TFA and PFPrA on the left, TFMS on the right), short (PFBA, PFPeA, and PFHxA on the left, PFBS and PFHxS on the right), and long (PFOA on the left, PFOS on the right). Shading marks the three compounds studied in this work, TFMS, PFBA, and PFPrA, which span the ultrashort- and short-chain classes.

1.4 Destruction Technologies and the Case for Alkaline Hydrolysis

A range of destruction technologies has been developed to cleave the carbon-fluorine bond. Electrochemical oxidation, plasma treatment, sonochemical cavitation, and photochemical and photocatalytic reduction all achieve defluorination in aqueous systems, but each is limited by some combination of byproduct formation, difficulty of scale-up, and slow or matrix-sensitive kinetics.[17-22] Mechanochemical milling achieves near-complete defluorination at ambient temperature but is a solid-phase process, better suited to sorbent-bound wastes than to the aqueous and concentrated liquid streams that dominate PFAS remediation.[23, 24] Supercritical water oxidation mineralizes PFAS rapidly and has been validated at pilot and full scale, but operating

above the critical point of water collapses inorganic salt solubility, so precipitation and the associated plugging and corrosion limit reactor life. [25-30]

Alkaline hydrolysis (AH), also referred to in the literature as hydrothermal alkaline treatment (HALT), can be a favorable technology in certain applications. By operating in the subcritical regime under high pH, water retains its high density and ionic solvation on which hydroxide-mediated chemistry depends while avoiding the salt-precipitation region of supercritical operation, and it fully mineralizes PFAS to fluoride, carbonate, and sulfate. [9, 31-36] It has been demonstrated for treating aqueous film-forming foam (AFFF), contaminated groundwater and soil, foam-fractionation concentrate, spent granular activated carbon, and other complex matrices. Several reports closed the fluorine mass balance for ultrashort-, short-, and long-chain PFAS, motivating further studies in this dissertation.

AH can destroy PFCAs under comparatively mild conditions, whereas the PFSAs require temperatures near 350 °C and NaOH loadings of 1 to 5 M to convert to fluoride, carbonate, and sulfate.[35, 37, 38] The high alkaline demand raises reagent cost, accelerates corrosion, and creates a substantial downstream neutralization and effluent-management burden. It also reflects a broader point: the conditions required for destruction depend on the structure of the target compound. Despite the growing use of AH, the destruction kinetics, product distributions, and defluorination behavior of many individual fluorinated compounds, particularly the ultrashort- and short-chain species, remain incompletely characterized. That gap is the starting point for this dissertation.

1.5 Research Objectives and Hypotheses

The overall objective of this dissertation was to characterize hydrothermal transformation of fluorinated compounds in continuous-flow systems amenable to process scale-up, for a range of PFAS classes, i.e., head groups and chain lengths, to identify the reaction products and kinetics,

and to obtain mechanistic insights into the differences in defluorination observed among them. Three specific objectives are defined, each framed around a hypothesis tested experimentally and, where appropriate, computationally. For every compound, destruction and defluorination were measured as functions of temperature and alkalinity, the liquid- and gas-phase products were identified, apparent activation energies were extracted where the data permitted, and density functional theory was used to distinguish among competing pathways.

1.5.1 Objective 1: Destruction Mechanism of an Ultrashort-Chain PFSA

The objective was to establish the destruction and defluorination behavior of TFMS and to identify the transformation pathways.

Hypothesis 1: *TFMS is destroyed under hydrothermal alkaline conditions by nucleophilic substitution at the carbon-sulfur bond, and a competing thermal pathway becomes significant only when hydroxide is limited.*

TFMS was processed across temperature and NaOH concentration, with parent-compound destruction quantified by LC-MS/MS and defluorination by ion chromatography. Sulfur and carbon products were speciated to close the mass balance, and the gas phase was analyzed for volatile fluorinated species. Density functional theory was used to separate homolytic from heterolytic bond cleavage and to identify the rate-determining step.

1.5.2 Objective 2: Destruction of TFMS in Modified Subcritical Water Regimes

The objective was to characterize TFMS destruction under two operating regimes that alter the subcritical water medium rather than the reagent dose.

Hypothesis 2: *Delaying the transition to supercritical conditions with a dissolved electrolyte, or inducing phase separation that concentrates NaOH in situ, achieves destruction comparable to conventional treatment at a lower initial alkali loading.*

Superheated ionically modulated alkaline hydrolysis (SIM-AH) adds a non-reactive electrolyte to delay the transition to supercritical conditions. Sodium chloride dissociates in water, and the Na^+ and Cl^- ions form hydration shells that require greater energy to overcome, so the critical temperature rises. For a 3 wt% NaCl solution, the critical point rises to 406.6 °C and 29.7 MPa, so operation at 400 °C and 30.0 MPa remains in the subcritical single-phase liquid region. [39, 40] NaCl is used rather than NaOH because it is not consumed in the reaction and its concentration therefore remains constant. Distillation alkaline hydrolysis (DAH) instead operates at reduced pressure and elevated temperature to enter the two-phase vapor-liquid region, where water partially evaporates while the non-volatile ionic species, including NaOH and the TFMS anion, remain concentrated in the residual liquid. Because the NaOH enrichment in DAH is transient and local to the reactor, it cannot be measured in the effluent and was inferred from destruction and product data. Both regimes are reported as characterized conditions under which the TFMS data were obtained, not as an engineering objective of this work.

1.5.3 Objective 3: Chain-Length Dependence of Defluorination in Ultrashort- and Short-Chain PFCAs

The objective was to identify the step that limits defluorination of the ultrashort- and short-chain PFCAs and to explain why PFBA is defluorinated nearly completely while PFPrA does not under the same conditions.

Hypothesis 3: *PFBA and PFPrA are destroyed with comparable ease, and the difference in their defluorination arises after decarboxylation, in whether the fluorinated fragment reacts within the residence time or is released unreacted at depressurization.*

PFBA and PFPrA were processed under conventional single-phase alkaline hydrolysis across temperature and NaOH concentration. Carbon balances were constructed from speciated organic

acids, carbonate, and residual parent compound, and were closed against the fluorine balance. Volatile fragments were collected and identified by gas chromatography-mass spectrometry, and carbon-13 and fluorine-19 NMR were used to confirm the liquid-phase intermediates. Density functional theory provided the elimination barriers of the fragments formed after decarboxylation.

1.6 Model Compounds and Scope

Three PFAS were chosen, characterized by their head-group and chain length while keeping the destruction chemistry tractable. TFMS is an ultrashort-chain PFSA that is used as a mechanistic probe for the regulated PFSAs it structurally resembles. Because it bears a single perfluorinated carbon and offers no sites for carbon-carbon bond cleavage, TFMS represents an extreme case of PFSA recalcitrance and therefore a stringent test of the proposed regimes.[41] PFBA and PFPrA are ultrashort- and short-chain PFCAs that extend the analysis to the carboxylic head group and allow tracking of degradation intermediates such as glycolate, tartronate, and oxalate.

Under comparable conditions the two acids reach similar parent-compound destruction, yet PFBA approaches complete defluorination by 225 to 250 °C while PFPrA at the same NaOH loading reaches only 41% at 250 °C and requires a further 50 °C to approach comparable values. That difference is explained here through closed carbon and fluorine mass balances and computed pathway energetics.

The scope has two boundaries. The expanded operating regimes were applied to TFMS alone; PFBA and PFPrA were studied under conventional single-phase alkaline hydrolysis, where the scientific question is the destruction chemistry and the chain-length dependence of defluorination rather than the operating regime. The computational work is of two provenances. The TFMS pathway calculations were performed by a collaborator to separate homolytic from heterolytic thermal degradation routes and are used here as supporting evidence. The PFBA and PFPrA

elimination-barrier calculations were performed as part of this dissertation, which constitute an original contribution of this dissertation.

1.7 Dissertation Organization

Chapter 2 reviews the shared foundation for the dissertation, from PFAS occurrence and regulation through the destruction technologies, the mechanism of alkaline hydrolysis, and the phase behavior that underlies the two regimes. Chapter 3 describes the shared experimental apparatus, analytical methods, kinetic treatment, and computational methods used throughout the dissertation. Chapter 4 presents the experimental results for TFMS and the two expanded regimes. Chapter 5 presents the ultrashort- and short-chain PFCAs, PFBA and PFPrA, together as a matched pair, with the compound-specific background needed to interpret their chemistry. Chapter 6 synthesizes findings across the three compounds, draws out the mechanistic and engineering implications of the SIM-AH and DAH regimes, and identifies directions for future work.

Chapter 2: Literature Review

This chapter establishes the foundation on which the experimental chapters rest. It then surveys the technologies proposed for destroying PFAS, develops the mechanism and operating envelope of alkaline hydrolysis, and establishes the phase behavior of the water-sodium chloride system that underlies the two regimes examined for TFMS. It closes with the mechanistic literature on PFAS degradation pathways and the specific gaps this dissertation addresses.

2.1 PFAS: Structure, Occurrence, Persistence, and Regulation

2.1.1 Structure and Properties

Though the definition varies depending on the source, here PFAS is defined as a class of compounds containing at least one perfluoroalkyl moiety, a carbon chain in which the hydrogen atoms bonded to carbon are replaced by fluorine. [1] They have been manufactured since the 1950s and are valued for a combination of properties that few other chemical families provide: thermal and chemical stability, resistance to oxidation, and surfactant behavior arising from the pairing of a hydrophobic and oleophobic fluorinated tail with a polar head group. These properties have led to their incorporation into aqueous film-forming foams used to extinguish hydrocarbon fires, non-stick cookware coatings, water- and stain-repellent textiles and paper, chrome plating, and a range of semiconductor and pharmaceutical processes. [1, 42]

The reason for the utility and the persistence of PFAS is the carbon-fluorine bond. At 105.4 kcal/mol it is the strongest single bond in organic chemistry, and its dissociation energy rises with fluorine substitution at the same carbon, reaching 116 kcal/mol (485 kJ/mol) in tetrafluoromethane.[43] Fluorine is the most electronegative element, and among the smallest, so the three lone pairs on each fluorine form a dense, electron-rich sheath around the carbon backbone that sterically and electronically shields it from nucleophilic and oxidative attack, while the large

difference in electronegativity gives the bond substantial ionic character that further strengthens it. The cumulative effect along a perfluorinated chain is a molecule that resists the hydrolytic, photolytic, oxidative, and microbial degradation pathways that degrade ordinary organic contaminants.[2]

2.1.2 Environmental Occurrence and Persistence

PFAS persist in the environment for years to decades; the short-chain species migrate readily in groundwater owing to their high water solubility and low sorption, while the long-chain species sorb to solids and accumulate near sources, and accumulate in soil, surface water, wildlife, and human tissue, which is the basis of the common mentions of PFAS as forever chemicals. [2, 44] They have been detected across the globe, including in remote Arctic and oceanic systems far from any point source, which demonstrates long-range atmospheric and oceanic transport in addition to local contamination. [13, 44] A 2023 United States Geological Survey study estimated that at least 45% of tap water in the United States contains one or more PFAS, illustrating the breadth of human exposure through drinking water alone.[7] Contamination is especially concentrated near sources such as fluorochemical manufacturing facilities, military installations, and airports where aqueous film-forming foams were used in fire training, landfills, and wastewater treatment plants, which act as ongoing secondary sources as precursor compounds transform. [42]

2.1.3 Human Health Concerns

Human exposure to PFAS has been associated with a range of adverse health outcomes. The most influential body of evidence came from the C8 Health Project, a large study of a population in the mid-Ohio Valley exposed to perfluorooctanoic acid (PFOA, historically called C8) through drinking water, whose science panel reported in 2012 probable links between PFOA exposure and high cholesterol, thyroid disease, ulcerative colitis, pregnancy-induced hypertension, and kidney and testicular cancer.[45] Subsequent work has added evidence for immunotoxicity, including

suppressed antibody responses to childhood vaccines associated with elevated serum PFAS, and for consistent associations with elevated serum cholesterol.[46] The state of the epidemiological evidence is not uniform: more recent reviews with improved exposure assessment and confounding control have questioned the strength of some of the earlier probable-link conclusions, particularly for kidney and thyroid cancer, so the field continues to refine which associations are causal.[14] What is not in dispute is that health effects are observed at low concentrations, which is why regulatory limits are set in the nanogram-per-liter range.

2.1.4 Regulation

The scientific consensus on persistence and toxicity has driven increasingly stringent regulation. In April 2024 the United States Environmental Protection Agency finalized the first national primary drinking-water regulation for PFAS, establishing enforceable maximum contaminant levels of 4.0 ng/L for PFOA and perfluorooctane sulfonic acid (PFOS), and 10 ng/L for perfluorohexane sulfonic acid (PFHxS), perfluorononanoic acid (PFNA), and hexafluoropropylene oxide dimer acid (HFPO-DA, known as GenX), together with a hazard-index limit for mixtures of these and perfluorobutane sulfonic acid (PFBS).[4] The maximum contaminant level goals for PFOA and PFOS were set at zero, reflecting the agency position that no level of exposure to these two compounds is considered safe.[4] The framework has continued to evolve, with proposals in 2025 and 2026 to retain the enforceable PFOA and PFOS limits while extending compliance deadlines toward 2031 and reconsidering the limits for the additional compounds.[1, 3, 14] The trajectory of regulation is clear, and because the compounds removed from water by adsorption, ion exchange, or membranes are concentrated rather than destroyed, tightening drinking water limits directly creates demand for destruction technologies capable of mineralizing PFAS in concentrated residual streams.

2.2 PFAS Destruction Technologies

The destruction technologies differ in the mechanism used to overcome the bond strength, in the matrices they suit, and in the byproducts they generate.

2.2.1 Electrochemical Oxidation

Electrochemical oxidation destroys PFAS at an anode surface, with substantial effort devoted to electrode selection, among which boron-doped diamond (BDD) anodes are the most studied, through a combination of direct electron transfer at the anode and attack by electrogenerated reactive species such as hydroxyl and sulfate radicals.[18] Reported energy per order of magnitude of removal is as low as 5.1 to 6.7 kWh/m³ in flow-through reactive electrochemical membranes, with fluoride mass balances of 76 and 69% for PFOA and PFOS.[18] Two limitations are prominent. First, in chloride-containing waters the same oxidative conditions generate toxic chlorate and perchlorate byproducts, which can require a downstream biological or chemical polishing step to reduce back to chloride before discharge. The electrode question remains open. BDD gives high oxidation rates but is costly and difficult to produce at the sizes scale-up requires; SnO_2-based and PbO_2 anodes are inexpensive but suffer short service lives or risk release of toxic Sb and Pb. Magnéli-phase titanium suboxide (Ti_4O_7) ceramics, conductive, chemically inert, and inexpensive to produce, have outperformed the other anode families in both conversion and defluorination, reaching greater than 95% defluorination of PFOA and 81% of PFOS, with oxidation rates exceeding those of Ce-doped PbO_2 and BDD electrodes, and have treated ion-exchange still-bottom waste at high chloride and organic loadings.[47] Those results were obtained at high conductivity and high initial PFAS concentration, and confirmation in real contaminated water is outstanding; in natural groundwater on BDD, PFOA and PFOS treatment rates were within a factor of two of those in synthetic electrolyte.[48] Electrooxidation is therefore best positioned for concentrated, conductive matrices, and its short-chain performance is an open question rather than

a solved one.[17] Second, structure-reactivity studies at BDD anodes find that shorter-chain PFAS are more difficult to break down than longer-chain compounds, for example a defluorination ordering of PFBA below GenX below PFOA, a chain-length dependence that recurs across destruction technologies and is directly relevant to the short-chain compounds studied in this dissertation. [49]

Quantitative performance is anode- and matrix-dependent. On a nanocrystalline boron-doped diamond anode at current densities of 3 to 50 mA/cm², chloride and the hydroxyl-radical scavenger tert-butyl alcohol reduced PFOA and PFOS removal and defluorination rates by less than 20%, indicating that the reaction proceeds by direct electron transfer at the anode rather than through bulk radical chemistry; treatment of natural groundwater at 0.3 and 0.6 mg/L was compared against electrolyte solutions at 15 and 10 mg/L.[48] Magneli-phase Ti_4O_7 ceramic anodes achieve comparable mineralization at lower cost than boron-doped diamond.[47]

Two limitations recur. Chloride in the feed is oxidized to perchlorate, an endocrine disruptor, and the anodes with the highest activity toward PFAS also produce the most perchlorate; adding at least 50 mM hydrogen peroxide suppresses perchlorate formation without loss of PFOA or PFOS destruction.[17] More broadly, the reported literature is dominated by small-scale batch systems and synthetic electrolytes, and because PFAS are surfactants whose adsorption and electrosorption depend strongly on concentration, experiments at elevated initial concentration or high supporting-electrolyte conductivity are likely to overstate performance at environmental levels.[18]

2.2.2 Plasma Treatment

Plasma treatment generates an electrical discharge between a high-voltage electrode and the water surface, and the reductive species formed there, free and solvated electrons and argon ions, carry the PFAS chemistry; argon bubbling transports the surfactants to the plasma-liquid interface,

which is the reactive zone.[50] Degradation yields shorter-chain PFCAs, organic acids, and fluoride, so defluorination is incomplete and short-chain products accumulate.[19] The first pilot-scale field demonstration, at an AFFF-impacted fire training site, reduced long-chain perfluoroalkyl acids and precursors by at least 90% in a single pass and brought PFOA and PFOS below the then-applicable advisory level within three cycles at a treatment cost near $7 per 3800 L. Short-chain acids, however, were removed to between 0 and 95%: they are generated during treatment of the long chains, and they accumulate poorly at the interface where the chemistry occurs, requiring a cationic surfactant amendment to reach 88% removal.[51] The technology is therefore effective for the long chains and weakest exactly where the compounds of this dissertation lie.

Reported performance spans a wide power range. In 1.4 L of solution, PFOA was reduced by 90% in 30 min at 76.5 W input power and by 25% at 4.1 W, and the low-power configuration degraded PFOS in groundwater without significant interference from co-contaminants; only about 10% of the parent was converted to shorter-chain products. [50]

The byproduct inventory is the better-characterized aspect of this route. Operated deliberately slowly to allow intermediates to accumulate, plasma treatment yields linear C4 to C7 perfluorocarboxylic acids from both PFOA and PFOS, with PFOA, perfluorohexanesulfonate, and perfluorobutanesulfonate additionally formed from PFOS; trifluoroacetic, acetic, and formic acids are also produced, and gas-phase byproducts account for less than 2.5% of the initial fluorine. [19] At pilot scale on AFFF-impacted groundwater, long-chain perfluoroalkyl acids and precursors were reduced by at least 90% in a single pass at 2.4 to 8.4 L/min, whereas short-chain acids with five or fewer fluorinated carbons were removed to between 0 and 95% because they partition less favorably to the plasma-liquid interface.[51] That interfacial dependence makes the method least effective on precisely the chain lengths studied in this dissertation.

2.2.3 Sonochemical Treatment

Sonolysis drives PFAS destruction through acoustic cavitation: transient bubble collapse reaches vapor temperatures near 5000 K, and PFOS and PFOA, resistant to radical oxidation, instead decompose pyrolytically at the bubble-water interface, with half-lives of 17 to 26 min at 358 to 618 kHz and mineralization essentially concurrent with parent decomposition.[52] The interface mechanism gives the process an unusual robustness to matrix: in diluted AFFF, PFOS degradation followed interface-saturation kinetics and was essentially unaffected by a fifty-fold excess of other organic carbon, because the perfluorinated surfactants outcompete the hydrocarbon surfactants for interfacial sites.[20] The same interfacial dependence is the limitation: rates fall with concentration below interfacial saturation, and the energy cost per mole rises as the feed becomes dilute, so sonolysis suits concentrated streams and has not advanced past bench scale.

Sonolysis has been demonstrated on real matrices rather than only on spiked solutions, including dilute aqueous film-forming foam, where degradation rates remained within a factor of two of those in clean water despite a fifty-fold excess of organic components, although fluoride release fell well below stoichiometric in the foam matrix.[20] Because the reaction is driven by transient cavitation rather than by a chemical oxidant, the energy demand scales with the volume treated rather than with the contaminant load, which is the principal barrier to application at the dilute concentrations typical of contaminated groundwater.[52]

2.2.4 Photochemical and Advanced Reduction Processes

Photochemical reduction generates the hydrated electron, most commonly by UV photolysis of sulfite, and is the most strongly structure-dependent of the destruction routes: defluorination depends on head group and chain length, the PFSAs resisting while PFCAs of two or more fluorinated carbons degrade at similar rates regardless of chain length.[53, 54] Sequential or integrated oxidation and reduction can bring defluorination of PFCAs and fluorotelomer acids to near-

quantitative levels.[55] The structural dependence differs under other mechanisms, a contrast examined in Chapter 6.

The structural dependence has been mapped across 34 PFAS. Perfluorocarboxylates from two to ten fluorinated carbons decay and defluorinate at similar rates, whereas fluorotelomer carboxylates and perfluoroalkyl sulfonates show a marked chain-length dependence; most structures defluorinate incompletely, and trifluoroacetate is the exception that reaches 100% defluorination. Computed carbon-fluorine bond dissociation energies relate the rate and extent of defluorination to the head group, the chain length, and the position and number of weak carbon-fluorine bonds. They do not account for trifluoroacetate, whose carbon-fluorine bonds are all high-energy primary bonds; its complete defluorination, despite parent decay slower than every longer perfluorocarboxylate, is assigned to a decarboxylation-hydroxylation-elimination-hydrolysis pathway rather than to direct carbon-fluorine cleavage.[53]

The limitation of the reductive route is chemical rather than energetic. Carbon-hydrogen bonds formed in the transformation products strengthen the remaining carbon-fluorine bonds and arrest defluorination short of completion, and the ethylene linker of the fluorotelomers insulates the fluorinated chain from the head group. Pairing hydroxyl-radical oxidation, which converts fluorotelomers to a mixture of perfluorocarboxylates while cleaving 35 to 95% of the carbon-fluorine bonds, with subsequent UV-sulfite reduction achieves near-quantitative defluorination that neither step reaches alone.[55] Across the advanced reduction processes the degradation pathway is governed principally by the head group, with chain length a secondary variable.[54] Under hydroxide the chain-length dependence differs, and Chapter 6 examines the contrast.

2.2.5 Mechanochemical Destruction

Mechanochemical destruction by ball milling offers a solvent-free, non-thermal route that is well suited to solid and sorbent-bound wastes. Co-milling PFAS with an alkaline hydroxide or a piezoelectric or mineral co-reagent under mechanical impact cleaves the carbon-fluorine bond at ambient temperature. With KOH, the most effective of the screened co-milling reagents, PFOA is destroyed completely within 3 h of milling with fluoride recovery above 97%, and PFOS reaches 99.88% destruction by 6 h; sulfate recovery leads fluoride throughout, placing desulfonation before defluorination, and the milled products are KF and K_2SO_4 by X-ray diffraction. Piezoelectric ball milling with boron nitride extends the approach to undiluted aqueous film-forming foams at ambient conditions with near-complete defluorination. [6, 24, 56] Studies have established that the co-milling reagent is decisive: potassium hydroxide is markedly more effective than sodium hydroxide or the oxide and silicate media screened; fluoride recovery falls as the potassium hydroxide to PFAS mass ratio is reduced from 95:1 to 5:1, and the milled products of PFOS degradation are potassium fluoride and potassium sulfate by X-ray diffraction.[24] Near-complete defluorination of PFOS and PFOA has been achieved, with fluoride recoveries of roughly 88 and 97% after 4 h of milling.[24] Mechanochemistry is effective and low-energy but is fundamentally a solid-phase process, less directly applicable to the aqueous and concentrated liquid streams that dominate PFAS remediation, and it generates a spent solid matrix requiring disposal.

The co-milling reagent determines both the extent of defluorination and the reaction sequence. With potassium hydroxide, sulfate is recovered ahead of fluoride, placing dissociation of the sulfonate head group before defluorination of the chain, and infrared spectra show loss of the terminal trifluoromethyl group as milling proceeds.[24] Persulfate and alumina act by different routes: alumina anchors the carboxylate through coordination to aluminium and weakens the

adjacent carbon-fluorine bonds, while persulfate supplies hydroxyl radicals. Either reagent alone converts PFOA to 1H-perfluoroheptene or to dimers with defluorination below 20%, whereas the combination gives 100% defluorination and 98% mineralization within 2 h of milling, and the same result extends to the C3 to C6 homologues.[23]

2.2.6 Supercritical Water Oxidation

Supercritical water oxidation (SCWO) destroys PFAS by operating above the critical point of water (374 °C, 22.1 MPa), where water becomes a low-polarity, low-viscosity medium in which organics and oxygen are fully miscible, enabling rapid and complete oxidation. [25, 26, 28, 29, 57, 58] SCWO has been validated at pilot and full scale for PFAS-containing wastes and spent treatment media and achieves high destruction and defluorination.[57, 58] Recent vendor-scale demonstrations provide the most relevant performance data. Three independent SCWO systems treating dilute aqueous film-forming foam each achieved greater than 99% reduction of the targeted PFAS, with PFOS reduced from 26.2 mg/L to 240 µg/L, from 30.4 mg/L to 0.310 µg/L, and from 190 mg/L to 8.57 µg/L across the three units.[25] Field deployment on reverse-osmosis concentrate at a military installation has since been reported.[59]

One of the main drawbacks is a direct consequence of the supercritical state: above the critical point, the solubility of inorganic salts is very low, so ionic compounds precipitate and, together with aggressive fluoride and chloride species at high temperature, cause reactor plugging and corrosion that limit operating life and drive up cost.[27, 60, 61] This limitation is avoided in subcritical alkaline hydrolysis due to the polar nature of liquid water.

2.2.7 Incineration

Thermal incineration is the incumbent disposal route for concentrated PFAS wastes and for fluoropolymer products. Fluorine in municipal waste is 0.010 to 0.035 wt% of dry solids in

Germany, and regulation caps total halogen in the feed at 1 wt%.[62] Complete thermal decomposition of PTFE is reached at 800 °C, below the 900 to 1100 °C attained at the pyrolysis and combustion fronts of a waste bed, so the nominal margin is large.[63]

At the BRENDA rotary kiln incinerator, PTFE destruction at 870 °C with a 4 s residence time and at 1020 °C with 2.7 s converted the polymer principally to hydrogen fluoride and carbon dioxide, and paired t-testing of flue gas sampled where the temperature fell from 850 to 1000 °C to below 300 °C found no statistically significant formation of the PFAS screened, at procedural quantitation limits of 0.3 to 6 µg/m³ for the short-chain PFCAs and 0.4 µg/m³ for trifluoroacetic acid.[62] A later campaign used mixed fluoropolymers at 860 and 1095 °C, both at 2 s and representing the minimum European conditions for municipal and hazardous waste incineration, respectively, and placed the reduction rate for products of incomplete combustion above 99.99%, with only perfluorooctanoic acid detected in stack gas at 0.20 ng/m³ against a quantitation limit of 0.09 ng/m³, attributed to external contamination. [63]

That work also makes a methodological point that bears on how destruction technologies are compared: destruction efficiency of the parent compound is not an acceptable measure of mineralization, because it places no constraint on the byproducts, and products of incomplete destruction must be measured directly. [63] The same distinction between parent compound removal and fluorine fate is emphasized throughout this dissertation.

It is unclear if the pilot studies' findings transfer to handling heterogeneous feed, and whether they extend to PFAS other than the fluoropolymers tested; that gap sustains the regulatory and public scrutiny incineration continues to face. [1] The uncertainty over incineration byproducts is one reason why aqueous-phase destruction routes, which deliver fluoride in a recoverable form and permit a closed fluorine balance, have attracted attention.

2.3 Alkaline Hydrolysis

2.3.1 Reaction Conditions and Foundational Work

Early work suggests that AH destroys PFAS through nucleophilic attack by hydroxide under subcritical or near-critical water conditions, typically 200 to 350 °C and pressures above the boiling curve, with strong alkali amendment raising the pH above 13.[31, 35] Destruction and defluorination of PFOS in batch reactors was demonstrated by Prof. Strathmann's group at Colorado School of Mines. Wu et al. screened a wide range of amendments and found that the most effective, regardless of chemical type, were those that shifted the solution to highly alkaline pH, pointing to a base-promoted mechanism. [31] The screen spanned acids, alkalis, oxidants, and reductants and returned defluorination extents from 0 to 80% after 90 min at 350 °C, with NaOH, $NaBH_4$, and K_2FeO_4 all exceeding 70%; the common property of the effective amendments was solution pH above 9. For NaOH, PFOS degradation followed a second-order rate law, first order in each of NaOH and PFOS with k2 of 0.052 ± 0.004 M^{-1} min^{-1} at 350 °C, and fluorine-19 NMR confirmed near-complete conversion of carbon-fluorine bonds to fluoride within 40 min at 1 M NaOH. Short-chain PFCA intermediates never exceeded 1.5% of the initial PFOS, placing sulfonate cleavage as the rate-limiting step ahead of rapid sequential decarboxylation, and octanoic acid, the unfluorinated analogue of PFOA, was unreactive at 250 °C without amendment, where more than 99% of PFOA degraded, showing that the fluorinated chain rather than the carboxylate alone controls hydrothermal reactivity. [31] This established the two central features of AH: the hydroxide dependence of the rate and the completeness of mineralization.

Subsequent work established that the reaction survives real matrices. In two aqueous film-forming foam formulations, all 109 identified PFAS degraded, most to nondetectable levels within 15 min and the most recalcitrant perfluoroalkyl sulfonates within 30 min at 5 M NaOH, with defluorination independent of dilution from 1:2 to 1:1000 and no stable volatile organofluorine

detected in the reactor headspace.[32] In foam-fractionation concentrates derived from AFFF-impacted groundwater, all 62 identified PFAS exceeded 90% degradation and defluorination within 90 min at 1 M NaOH, rate constants for the recalcitrant sulfonates were unchanged by dissolved organic carbon to 4.5 g/L and chloride to 325 mg/L, and defluorination exceeded 90% relative to the total organic fluorine; roughly 15% of the non-fluorinated organic carbon resisted treatment, consistent with a nucleophilic mechanism that leaves non-electrophilic organics untouched.[9] Continuous-flow processing of fire-training-pond water in this laboratory reduced PFOS below detection within 1.6 min at 5 M NaOH, destroyed the PFCAs even at 0.1 M, and left the short-chain sulfonates PFBS and PFPeS requiring the full 5 M loading; the fluorine balance was not closed in that study, which is among the gaps the present work addresses.[35] For the ultrashort chains, hydrothermal treatment of trifluoroacetic acid in the same reactor showed thermally driven decarboxylation independent of NaOH with an activation energy of 191.1 ± 7.8 kJ/mol, fluoroform partitioning to the gas phase without alkali, and a fluorine balance closed at 100 ± 6% once NaOH met the stoichiometric requirement, with the explicit hypothesis that longer PFCAs would release the corresponding 1H-perfluoroalkanes as volatile organofluorine species.

Subsequent work extended AH from single-compound solutions to complex, real-world matrices. Hao et al. demonstrated rapid degradation of all of more than one hundred PFAS identified in two aqueous film-forming foam formulations, including recalcitrant PFSAs and precursor compounds, at 350 °C with 1 to 5 M NaOH, and further applied AH to contaminated groundwater and soil, to foam-fractionation concentrate, and to spent granular activated carbon, where it both destroyed the adsorbed PFAS and regenerated the adsorbent.[9, 32-34, 37] Work on high total-dissolved-solids solutions subsequently closed the fluorine mass balance across ultrashort-, short-, and long-chain

PFAS simultaneously, which is essential to demonstrate true mineralization rather than mere loss of the parent compound.

Kinetics under alkaline hydrothermal conditions are second order overall. For PFOS between 200 and 350 °C, P~2 - 16.5 MPa, the rate follows minus d[PFOS]/dt equals k2 times the hydroxide and PFOS concentrations, with k2 of 0.052 plus or minus 0.004 $M^{-1}min^{-1}$ at 350 °C, and fluorine-19 NMR shows complete conversion of carbon-fluorine bonds to fluoride within 40 min at 1 M NaOH for a 2.5 g/L PFOS feed. A screen across acids, alkalis, oxidants, and reductants gave defluorination ranging from 0 to 80% after 90 min, and the effective amendments were those that raised the solution to pH 9 or above regardless of type, which identifies the reaction as base-promoted rather than oxidative or reductive.[31]

The approach extends to complex mixtures without loss of rate. All 109 PFAS identified across two AFFF formulations, one sulfonate-based and one fluorotelomer-based, fell below detection within 15 min at 350 °C and 16.5 MPa in 1 to 5 M NaOH, with the recalcitrant perfluoroalkyl sulfonates requiring 30 min at 5 M, and no stable volatile organofluorine was detected in the reactor headspace.[32] In foam fractionation concentrates containing all 62 PFAS identified as cations, anions, and zwitterions, degradation and defluorination both exceeded 90% within 90 min at 1 M NaOH, and the sulfonate rate constants were unchanged by an initial perfluorohexanesulfonate concentration of 0.55 g/L, dissolved organic carbon to 4.5 g/L, or chloride to 325 mg/L; approximately 15% of the dissolved organic carbon resisted treatment.[9] Matrix insensitivity of this kind is unusual among the destruction technologies reviewed above and is the principal practical argument for the method.

Most of this work is in batch reactors. Continuous-flow operation on AFFF-impacted fire training pit water has been demonstrated and gives faster parent-compound destruction than batch systems

at matched temperature and alkali loading, which is the configuration used throughout this dissertation.[35]

2.3.2 Head-Group Dependence and the Alkaline-Demand Problem

A consistent finding across the literature is that destruction efficacy depends strongly on the PFAS head group. PFCAs are destroyed and defluorinated under comparatively mild conditions, near 200 °C with alkaline amendment as low as 0.1 M NaOH, because the carboxylate readily decarboxylates to a reactive intermediate. PFSAs are more recalcitrant in an AH environment, requiring temperatures ~350 °C and NaOH concentrations of roughly 1-5 M for complete mineralization, because the carbon-sulfur bond must be cleaved and there are fewer facile activation routes.[31, 37] Another general observation is that defluorination lags parent-compound destruction at lower alkalinity and lower temperature, indicating that fluorinated organic intermediates form first and require sufficient alkali concentration to complete mineralization; this lag is reduced as temperature and hydroxide increase.

The high alkaline demand of more recalcitrant PFSAs is the main practical limitation of conventional AH. High NaOH loading raises reagent cost, accelerates corrosion of reactor alloys, and creates a substantial downstream neutralization and effluent-management burden, since the effluent must be neutralized and its elevated dissolved solids managed.[35, 38] Prior work has largely accepted this alkaline demand as an unavoidable cost. The question of whether it can be reduced by manipulating the properties of the subcritical water medium rather than by adding reagent motivates the research into expanded AH regimes. These regimes exploit the water phase transition under electrolyte amendment. This dissertation examines the efficacy of AH regimes in PFAS destruction using TFMS as a model compound.

2.4 Subcritical Water Properties and the H_2O-NaCl System

2.4.1 Properties of Sub- and Near-Critical Water

The properties of water change significantly as it approaches its critical point at 374 °C and 22.1 MPa. The existence of a supercritical fluid state has been recognized since Baron Cagniard de la Tour reported his high-pressure experiments in 1822, and the critical point of a substance was described by Thomas Andrews in 1869. [64-66] In the subcritical compressed-liquid region relevant to AH, water retains a high density, so it continues to coordinate and dissolve ionic species and to support hydroxide-mediated hydrolysis, while the elevated temperature accelerates reaction kinetics and the ion product of water rises, increasing the availability of hydroxide. [27, 67, 68] Above the critical point, density and dielectric constant fall steeply and ionic solubility collapses. The loss of solvating power is the origin of the salt precipitation described in Section 2.2.6, and the reason subcritical operation is chosen here.

These changes are given quantitatively below, because the operating envelope of this work was chosen against them. Figure 2.1 gives the relative permittivity and the density of water computed from the IAPWS-95 formulation.[69, 70] Permittivity is the property that governs whether an electrolyte remains solvated: it falls from 79 at ambient conditions to 28 at 250 °C and to 15 at 350 °C, so across the range examined here water is progressively less able to support dissolved ions, although it remains an electrolyte solvent throughout. The decline tracks falling density. Molecular dynamics simulations of aqueous NaCl from ambient to supercritical conditions show that ion association increases sharply over this range: single ions fall from 63% of the solute inventory at ambient conditions to 13% near the critical temperature, and the sodium hydration number falls from 4.8 to 2.8 as chloride replaces water in the first hydration shell.[71] Lower permittivity also lengthens the Bjerrum separation, so ion pairing becomes favorable at conditions where it is negligible at ambient temperature. Sodium salts precipitate at the upper end of this

range. The phase boundary used in this work is taken from the Driesner and Heinrich correlations rather than from a permittivity threshold, and it separates alkaline hydrolysis from supercritical water oxidation.

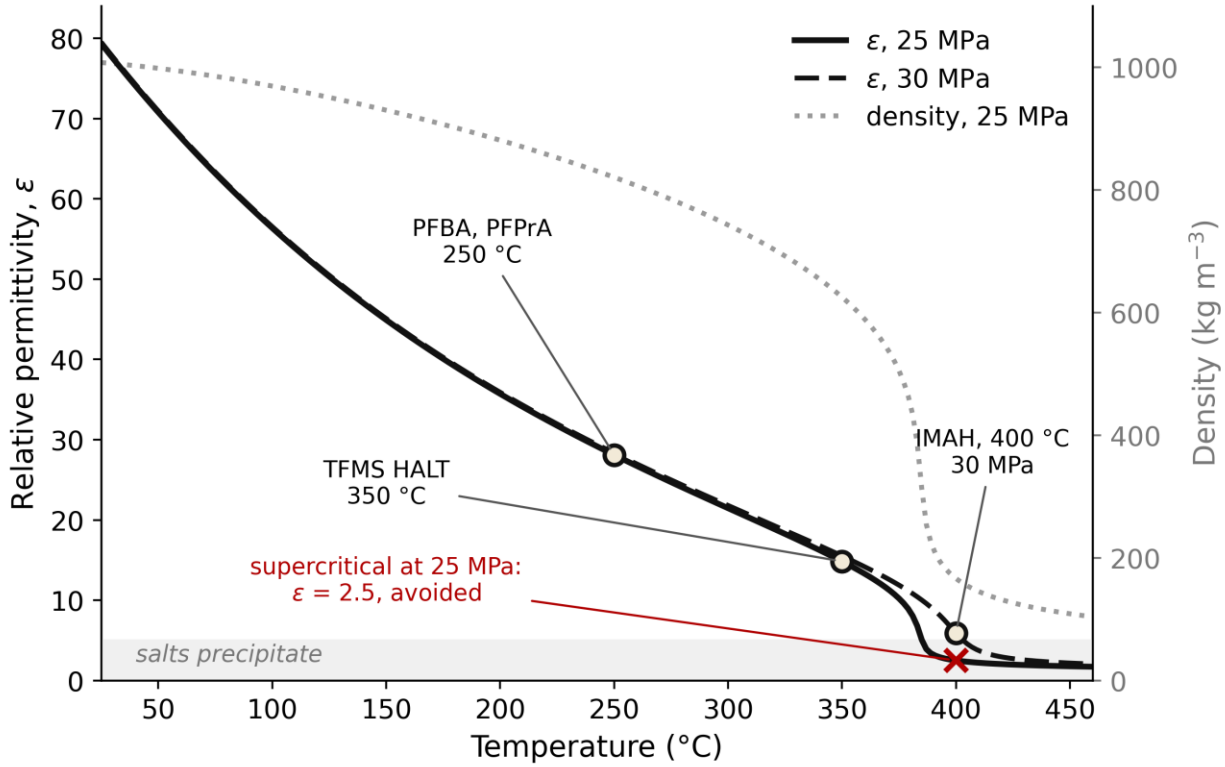

Figure 2.1: Relative permittivity and density of water as a function of temperature, computed from the IAPWS-95 formulation. Solid and dashed curves give the permittivity at 25 and 30 MPa; the dotted curve gives the density at 25 MPa. Markers indicate the conditions used in this work. At 400 °C the permittivity is 5.9 in the compressed liquid at 30 MPa but 2.5 in the supercritical fluid at 25 MPa. Shading marks the region in which sodium salts precipitate; the threshold is gradual rather than sharp. Values are for pure water.

The consequence for this work is most visible at 400 °C. In the compressed liquid at 30 MPa, the permittivity is 5.9, and the density is 357 kg/m³, whereas in the supercritical fluid at 25 MPa, the same temperature gives a permittivity of 2.5 and a density of 167 kg/m³. A pressure difference of 5 MPa therefore more than doubles both properties. The denser fluid retains the alkali in solution; the supercritical fluid does not. This is the physical basis of the ionically modulated regime developed in Chapter 4: raising the critical point with added electrolyte allows the temperature to be increased to 400 °C while the system stays in the compressed liquid, rather than crossing into a

fluid in which the alkali would precipitate. The values plotted are for pure water; the corresponding boundaries for the 3 wt% sodium chloride solution used in that work are given in Appendix C.

2.4.2 Phase Behavior of the Water-Sodium Chloride System

The location of the critical point in the presence of a dissolved electrolyte has been studied far less than that of pure water; it is particularly important here in determining the operating windows of both expanded regimes. Driesner and Heinrich developed comprehensive relationships for the phase transition of the water-sodium chloride system as functions of temperature, pressure, and composition, enabling calculation of the compressed-liquid, vapor, and halite phase boundaries and the critical curve across a wide range of conditions.[39, 40] Complementary equation-of-state and volumetric data for concentrated sodium chloride and sodium hydroxide solutions at hydrothermal conditions provide the density and vapor-pressure behavior needed to design and interpret experiments in this system.[72, 73, 74] These correlations show that adding sodium chloride raises the critical point of water; for a 3 wt% NaCl solution, the critical point rises to approximately 406.6 °C and 29.7 MPa, roughly 32 °C above that of DI water. [39, 75] The origin of this shift lies in the strongly asymmetric partitioning of the salt between the two phases. Sodium chloride is effectively non-volatile at these conditions: experimental vapor-liquid measurements place the NaCl content of the vapor at only 0.003 to 0.012 wt% near the critical temperature of pure water, so the salt is confined almost entirely to the compressed liquid.[75] A critical point is the state at which the coexisting liquid and vapor phases become indistinguishable, and that identity cannot be reached while one phase carries the electrolyte and the other cannot dissolve it. Solvating ions requires the close coordination by water molecules that only the dense liquid provides, so the difference in density and composition between the phases persists to higher temperature and pressure than in pure water, and the critical curve rises continuously from the critical point of water toward that of molten sodium chloride. [73, 75] The same non-volatility has a second consequence used directly in

this work. When the pressure is reduced at elevated temperature, water partitions preferentially into the low-density phase while the non-volatile solute remains behind and is concentrated in the residual liquid, forming concentrated brine solution. The critical point shift and in situ alkali concentration are therefore the consequences of a single property of the system rather than two independent effects.

Two consequences of the critical point shift are exploited in the TFMS work. First, elevating the critical point permits operation at higher temperature, i.e., ~400 °C, with water remaining in the subcritical single-phase liquid region, which accelerates hydrolysis without incurring supercritical salt precipitation. Second, at elevated temperature with the electrolyte present, reducing the system pressure drives the system into the two-phase vapor-liquid coexistence region, where water preferentially partitions into the low-density phase while the non-volatile ionic species, including hydroxide, concentrate in the residual liquid. [40, 72] The thermodynamic basis for these regions are captured entirely by the Driesner and Heinrich phase correlations, which are used in this dissertation to define the operating windows and to remain clear of the halite region where solid salt would precipitate. This phase framework is not used for the PFCAs destruction studies; these can be effectively treated under conventional single-phase conditions, but the subcritical-water properties reviewed here apply throughout.

2.5 Degradation Pathways and Mechanistic Probes

2.5.1 PFCA Pathways

The degradation chemistry of PFAS depends strongly on the head group and on chain length. For PFCAs, the established route begins with decarboxylation to release carbon dioxide and generate a reactive perfluoroalkyl intermediate, which then loses fluoride in a stepwise cascade. Trang et al. demonstrated that PFCAs can be mineralized under mild conditions through a sodium

hydroxide-mediated pathway in polar aprotic solvent, in which decarboxylation produces reactive perfluoroalkyl anions that degrade to fluoride, with fluoride yields of 78 to nearly 100%, and they showed by product analysis that the observed intermediates were inconsistent with the often-proposed one-carbon chain-shortening mechanism. [76] Instead, the carbanion undergoes fluoride elimination to a perfluoroalkene, followed by hydroxide addition and further defluorination, a mechanism supported computationally and by intermediate detection. This work established that PFCA defluorination can be tuned chemically rather than requiring thermal extremes, and it identified head-group activation as the mechanistic bottleneck. The same qualitative sequence has been observed under hydrothermal alkaline conditions, where added strong base catalyzes decarboxylation of both short- and long-chain carboxylic acids. [31]

The one-carbon case has been resolved experimentally in continuous flow AH systems at UW. Trifluoroacetate decarboxylates to the trifluoromethyl anion, which abstracts a proton from water to give fluoroform; fluoroform is volatile and leaves the solution at neutral or acidic pH, but at elevated pH it reacts with hydroxide instead, and neither fluoroform nor bicarbonate is observed in its place. The products are then fluoride, formate, and carbonate. The formate is formed by dehydration of an unstable geminal diol formed through repeated nucleophilic substitution.[37] The same work reports that carbon monoxide, proposed elsewhere as a product of this sequence, was not detected in the gas phase.

That result sets up the question addressed in Chapter 5. If the volatile 1H-perfluoroalkane is the common intermediate of the perfluorocarboxylate cascade, recovery of its carbon depends on hydroxide re-activating the fragment within the residence time. The elimination barrier changes along the series, so the outcome should shift with chain length.[37]

2.5.2 Chain-Length and Structure-Reactivity Relationships

Structure-reactivity studies of reductive defluorination provide the clearest available framework for predicting the extent of defluorination from molecular structure. The most systematic study examined 34 PFAS structures undergoing reductive defluorination by UV-generated hydrated electrons. It established that the head group, rather than chain length alone, is the primary determinant of reactivity. [53] PFCAs spanning two to ten perfluorinated carbons showed similar rates and extents of both parent decay and defluorination, whereas fluorotelomer carboxylates and PFSAs showed a pronounced dependence on the length of the fluoroalkyl chain.[53] These trends were connected to computed carbon-fluorine bond dissociation energies, relating the rate and extent of defluorination to the head group, the chain length, and the position and number of carbon-fluorine bonds with low dissociation energies.[53]

Two findings from the hydrated-electron studies apply directly to this dissertation. First, most structures defluorinated incompletely, and the incomplete defluorination of PFCAs was subsequently attributed to the accumulation of partially fluorinated products in which a fluorine has been replaced by hydrogen. [53] The general lesson is that a defluorination deficit need not indicate an incomplete reaction; it can equally indicate a stable partially fluorinated product that has left the reactive pool. Second, and counterintuitively, the shortest PFCA, trifluoroacetate, defluorinated essentially completely while most longer structures did not, a result the authors singled out as a distinctive behavior of the shortest chain. Short-chain PFSAs, by contrast, were sluggish toward hydrated electrons and recalcitrant to oxidation, and were flagged as a specific management concern for that reason.[53]

Chain-length behavior is not universal across destruction chemistries, and this is the point of departure for the present work. Under hydrated electrons, PFCAs of two to ten perfluorinated

carbons behave alike. [53, 76] Under base-mediated decarboxylation in polar aprotic solvent, PFCAs of various chain lengths are likewise mineralized efficiently, as described in Section 2.5.1.[76] At BDD anodes, the ordering inverts, and the shorter PFCAs are the harder ones to defluorinate (Section 2.2.1). Chain length therefore governs defluorination in some systems and not in others, indicating that the controlling step is not an intrinsic property of the carbon-fluorine bond and can be a property of reaction intermediates specific to a transformation route.

One structure-reactivity series is available under hydrothermal alkaline conditions. Defluorination of the C_4 to C_{12} PFCAs in aqueous NaOH at 280 °C is second-order and first-order in each of the acid and NaOH, with rates rising as the chain shortens, with PFBA the fastest. The second-order rate constants fall on a single line against saturation vapor pressure.[77] Endo and Funazukuri postulate partitioning of the parent acid between vapor and liquid, taking the reaction to occur in the liquid phase because NaOH partitioning, so that a shorter chain leaves less parent in the liquid and raises the NaOH-to-PFCA ratio. They state that partition ratios are needed to confirm this.[77] That series stops at four carbons, and it reports defluorination alone, without parent destruction, carbon balance, or gas-phase speciation, so partitioning of the parent is the only variable it can resolve. Extrapolated to three carbons, it predicts that PFPrA should defluorinate faster than PFBA. However, the data do not support this hypothesis, as described in Chapter 5, the opposite ordering and places the competition between reaction and release at the fragment that decarboxylation produces rather than at the parent.

2.5.3 PFSA Pathways and Computational Methods

For PFSAs, the analogous activation step is cleavage of the carbon-sulfur bond rather than decarboxylation. TFMS, with a single perfluorinated carbon bearing a sulfonic head group, is structurally homologous to the regulated PFSAs and represents an extreme case of their

recalcitrance, since it offers no carbon-carbon bonds to cleave. Short-chain PFSAs have been shown to be more recalcitrant than their longer-chain homologs under hydrothermal treatment, attributed to fewer carbon-carbon cleavage sites and reduced intermediate stability.[41] Density functional theory has become a standard tool for distinguishing competing degradation routes for these systems, for example, comparing hydroxide attack at sulfur against attack at carbon, and identifying which elimination or hydrolysis step controls the observed rate.[41, 53] The kinetics of formic acid decomposition in subcritical and supercritical water have been characterized by in situ Raman spectroscopy at 25 MPa and provide reference behavior for interpreting AH product distributions.[78]

The head-group cleavage step has been characterized directly. Under alkaline hydrothermal conditions, PFOS yields short-chain perfluorocarboxylic acids as transient intermediates at no more than 1.5% of the initial PFOS, which places hydroxide-mediated cleavage of the sulfonate head group first and sequential decarboxylation of the resulting carboxylate second.[31] TFMS, the shortest-chain PFSA and the compound studied in Chapter 4, has been examined under the same conditions in batch: 0.1 M TFMS at 350 °C in 1 M NaOH reached 65.7% mineralization after 180 min, with essentially all of the fluorine and sulfur in the degraded fraction recovered as fluoride and sulfate, and the degradation was attributed to concurrent nucleophilic substitution and base-promoted pathways.[41] That work establishes the product inventory against which the present continuous-flow results are compared.

2.5.4 Volatile Fragment Release

A theme recurring across these mechanistic studies, and central to this dissertation, is that carbon-containing intermediates can leave the reactor before they are fully defluorinated. Where a decarboxylation or elimination step generates a small, volatile fluorinated fragment, that fragment

can leave the reacting liquid before completing the defluorination cascade, removing both carbon and fluorine from the reacting pool and depressing the apparent defluorination without implying any failure of the underlying mechanism.

The clearest precedent is the hydrothermal transformation of trifluoroacetic acid, the simplest PFCA. In compressed liquid water at 150 to 250 °C, TFA decarboxylates to fluoroform and carbon dioxide, both of which aspirate naturally from solution. [37] Thermal decarboxylation of TFA to these same products had been reported earlier in high-pressure water above 180 °C and in ethylene glycol. [79, 80] The decisive observation concerns what alkali does to the fluorine balance. Without alkaline amendment, the carbon and fluorine liberated from TFA were not recovered in the liquid phase, and the fluorine balance could not be closed quantitatively, because the products left as gas. [37] With stoichiometric concentration of sodium hydroxide, fluoride formed stoichiometrically, and the fluorine balance closed to within experimental uncertainty, indicating that fluoroform reacts with hydroxide rapidly enough to prevent its accumulation and release. [37]

The competition is therefore between reaction and the residence time, and its outcome is set by how fast the fragment reacts relative to how fast it leaves the reactive environment (e.g., partitions to gas or its supercritical phase). Fluoroform serves as a good probe to test this hypothesis. It is thermally robust, surviving shock-tube conditions to roughly 900 °C and requiring catalytic hydrolysis near 600 °C in water vapor, yet in the presence of alkali it is mineralized at temperatures near 150 °C. [37] Hydroxide converts a fragment that thermal treatment struggles to destroy into one that is readily mineralized under mild hydrothermal conditions. Consistently, the kinetics of TFA disappearance showed little dependence on NaOH concentration, placing the rate-limiting step at thermal decarboxylation and locating the role of hydroxide entirely downstream, in the capture of the fragment. [37]

The same signature appears for a PFSA. Fluoroform was detected in the gas phase during hydrothermal treatment of TFMS at 400 °C in the absence of alkali, but at no temperature when hydroxide was present, which is what would be expected if OH^- reacts with the fragment before the fluoroform separates as an immiscible phase. Note that the supercritical transition for fluoroform occurs 25.7 °C (299.1 K) and a critical pressure of 4.82 MPa. These results are shown in Chapter 4.

In the existing literature, fragment partitioning has been treated largely as an analytical caveat, a reason that fluorine balances fail to close. Here it is proposed that hydrothermal treatment phase separation can be a chain-breaking step in the reaction mechanism. For the ultrashort- and short-chain PFCAs, the fragment remaining after decarboxylation must either eliminate fluoride and continue toward mineralization or be protonated to a hydrofluorocarbon reservoir that is inert on the process timescale and lost, and the barrier separating those two fates determines how far defluorination proceeds. [37, 76]

2.6 Knowledge Gaps and Research Questions

Three gaps emerge from the literature review. First, although the mechanistic literature establishes that head group and chain length govern defluorination, the destruction kinetics, product distributions, and defluorination behavior of many individual ultrashort- and short-chain fluorinated compounds under AH conditions remain incompletely characterized. The C_1 PFSA TFMS, as the recalcitrant limit of the PFSA class, and the ultrashort- and short-chain PFCAs (PFPrA and PFBA) are not characterized under AH conditions. Their kinetics and product distributions are required to quantify the destruction chemistry of the class. [5, 41]

Second, and most specifically, the difference between compounds that achieve comparable parent-compound destruction yet defluorination differing by a factor of two or more has not been

explained through a quantitative, closed mass-balance account combining pathway energetics with the fragment's reaction rate against the residence time. The one hydrothermal alkaline series available spans four to twelve carbons and assigns the chain-length ordering to partitioning of the parent acid,[77] which the destruction data reported here exclude for the compounds studied. The mechanistic origin of the defluorination difference between PFBA and PFPrA is the central question of this dissertation. [37, 76]

Third, although the phase behavior of the water-sodium chloride system is well characterized, it has not previously been used to define alkaline hydrolysis regimes that exploit critical-point shift or in-situ hydroxide enrichment, which is the subject of the TFMS destruction work. [39]

These gaps motivate the research questions of this dissertation. What are the destruction kinetics, product distributions, and defluorination behavior of TFMS, PFBA, and PFPrA under hydrothermal alkaline conditions? What determines the extent of defluorination for the ultrashort- and short-chain PFCAs, and can a closed carbon and fluorine mass balance explain the difference in defluorination between PFPrA and PFBA? A secondary question, arising within the TFMS study, is how the destruction and product data respond when the subcritical water medium is modified through the ionically modulated and distillation regimes.

Chapter 3: Materials and Methods

Where a method or reactor configuration is specific to one compound, that specificity is noted here and referenced again in the relevant chapter rather than repeated in full.

3.1 Materials and Reagents

The stoichiometric NaOH requirement is defined throughout on complete bond scission, as one hydroxide per carbon-fluorine, carbon-carbon, and carbon-hydrogen bond in the parent molecule. PFPrA carries five carbon-fluorine and two carbon-carbon bonds, giving seven. PFBA carries seven carbon-fluorine and three carbon-carbon bonds, giving ten. R-134a carries four carbon-fluorine, one carbon-carbon, and two carbon-hydrogen bonds, giving seven. Loadings are reported as the acid-to-NaOH molar ratio and, where useful, as a multiple of that requirement.

In the AH experiments, stock solutions were prepared using deionized water (18.2 MΩ·cm) from an ELGA PURELAB Option-Q system (Woodridge, IL, USA). Sodium hydroxide (10 M, MilliporeSigma, Burlington, MA, USA) was diluted to prepare NaOH solutions in the 0 to 2 M range, and sodium chloride (Fisher Scientific, Hampton, NH, USA) was added at 3 wt% to reagent solutions for the ionically modulated and distillation regimes. The three model compounds, their feed concentrations, and the reactor used for each are summarized in Table 3.1. For LC-MS/MS calibration of TFMS an unlabeled TFMS sodium salt standard (Cambridge Isotope, Tewksbury, MA, USA) was used over the 0.05 to 50 µg/L range. Total ionic strength adjustment buffer 2 (TISAB 2) was used at 50% by volume for fluoride ion-selective electrode sample preparation, certified anion standards were used for ion chromatography calibration in the 0.1 to 20 mg/L range, and LC/MS-grade methanol was used for sample dilution before LC-MS/MS analysis.

Table 3.1: Model compounds, feed concentrations, and reactor configurations.

Compound	Formula	MW (g/mol)	Feed conc.	Reactor	Supplier
TFMS	CF_3SO_3H	150.08	0.025 M	4.2 mL	MilliporeSigma / Cambridge Isotope (std)
PFPrA	C_2F_5COOH	164.04	0.05 M	3.2 mL	Sigma-Aldrich
PFBA	C_3F_7COOH	214.04	0.05 M	3.2 mL	Sigma-Aldrich

3.2 Reactor System and Operating Regimes

The experiments used continuous-flow hydrothermal reactors of the type described previously.[35, 37] Two reactor sizes were employed depending on the compound and on whether high gas throughput was required. The larger reactor was used for TFMS, and a smaller reactor was used for PFPrA and PFBA. The two expanded operating regimes described in Sections 3.2.2 and 3.2.3, SIM-AH and DAH, were applied to TFMS, where the alkaline demand is highest. The ultrashort- and short-chain PFCAs, PFBA and PFPrA, were processed under conventional single-phase alkaline hydrolysis at elevated pressure.

3.2.1 Continuous-Flow Reactors

The layout of the continuous-flow system is shown in Figure 3.1.

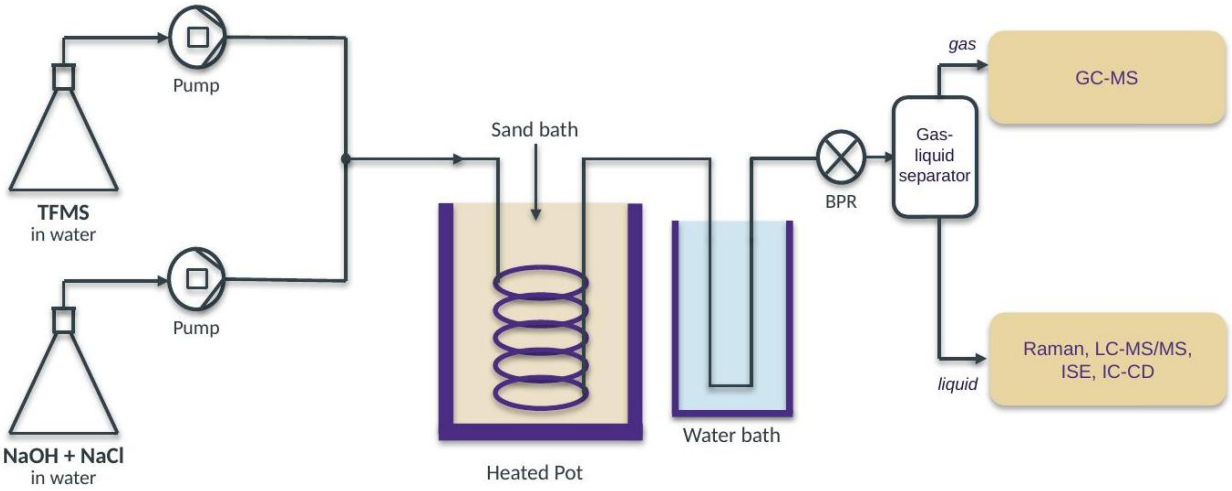

Figure 3.1: Schematic of the continuous-flow hydrothermal reactor. Separate pumps deliver the substrate stream and the alkaline stream, which combine before entering the coiled reactor held in a heated sand bath. The effluent is quenched in a water bath, depressurized across a back-pressure regulator, and separated into gas and liquid streams for analysis. Gas-phase products are analyzed by GC-MS; liquid-phase products by Raman spectroscopy, LC-MS/MS, fluoride ISE, and IC-CD. The schematic depicts the two-stream configuration used for TFMS (4.2 mL Inconel 600 coil); the PFBA and PFPrA experiments used a single premixed compound-and-NaOH feed through a 3.2 mL Hastelloy C276 coil, with the remainder of the flow path unchanged.

The small-scale lab-scale reactor consists of a 3.175 mm outer-diameter, 10 m long, Inconel 600 coiled tube with an internal volume of 4.2 mL and a surface-to-volume ratio of approximately 26.3 cm^{-1}.[37] The coiled reactor section is submerged in a sand bath held at the operating temperature by proportional-integral-derivative controllers, and K-type thermocouples measure the sand temperature and the reactor wall temperature at the inlet and outlet. In all experiments, the temperature difference between the coil inlet and outlet was less than 4 °C, providing near-isothermal reacting conditions. The feed streams are introduced by positive-displacement pumps: a Waters 515 HPLC pump for the compound solution and a Teledyne LS-class pump for the NaCl-NaOH reagent solution, with the two streams mixed upstream of the heated section. System pressure was maintained between 13.8 and 30.0 MPa by a back-pressure regulator downstream of a cooling section. The effluent was rapidly cooled, liquid samples were collected in 20 mL scintillation vials, and gas samples were collected in 600 mL Tedlar bags.[37]

Residence time in the hot zone was targeted at approximately 10 minutes. The pump flow rate was set by mass conservation, as given in Equation 3.6. The NaCl-water mixture was used as the density basis because density data for the H_2O-NaOH system are unavailable under these hydrothermal conditions; at 2 M the sodium hydroxide mass fraction (approximately 8 wt%) exceeds that of the added NaCl (3 wt%) and would contribute comparably to the mixture density, so neglecting it introduces an acknowledged uncertainty in the residence-time estimate. [74]

3.2.2 Superheated Ionically Modulated Alkaline Hydrolysis (SIM-AH)

The critical point of pure water is 374 °C and 22.1 MPa. Above it, water enters the supercritical phase.[39, 40] Adding a non-volatile electrolyte shifts this point, for the reason developed in Section 2.4.2: the salt partitions almost entirely into the dense liquid, so the two phases cannot become identical until higher temperature and pressure are reached.[75] The addition of 3 wt% NaCl shifts the critical point from 374 °C to 406.6 °C and raises the corresponding critical pressure to 29.7 MPa, extending the operational temperature range of alkaline hydrolysis while remaining subcritical.[39, 75] In a typical SIM-AH experiment, once the reactor reached target temperature under deionized-water flow, a background sample was collected, then the compound solution and the NaOH solution (0.1 to 2.0 M, with 3 wt% NaCl) were introduced at 50:50 volumetric flow rates with pressure held at 30.0 MPa to ensure compressed-liquid conditions. Temperatures of 350, 380, and 400 °C were tested, all subcritical for 3 wt% NaCl, and sample collection began after at least five reactor volumes had passed (approximately 60-80 minutes) to ensure steady state.

3.2.3 Distillation Alkaline Hydrolysis (DAH)

The distillation regime exploits the vapor-liquid equilibrium of the electrolyte-water system. At elevated temperature, reducing the pressure moves the system from single-phase compressed liquid into the two-phase region: near 24.8 MPa the system enters a supercritical-plus-liquid region, and at 20.0 MPa a vapor-plus-liquid region. [39, 72] Because NaOH and NaCl have negligible

vapor pressure relative to water, water preferentially partitions into the low-density phase while the non-volatile ionic species, including hydroxide, concentrate in the residual liquid. Using the phase-equilibrium correlations for the water-NaCl system, reducing the pressure from 24.8 to 13.8 MPa at 350 °C is estimated to convert roughly 90% of the water to the vapor phase, increasing the hydroxide concentration in the residual liquid by approximately ten-fold, with the dissolved compound assumed to remain in the aqueous phase. [39, 40] The density of the mixed phase was used to calculate residence times in the two-phase experiments.

3.3 Analytical Methods

Parent-compound destruction, defluorination, and the distribution of carbon- and sulfur-containing products were quantified by complementary techniques. Because no single technique captures the full product slate, the methods were cross-validated and the limitations of each are stated.

Raman spectroscopy (MarqMetrix Inc., Seattle, WA) was used for direct, dilution-free quantification of parent compound and of Raman-active products, with a 10 second integration time over a 200 to 3100 cm^{-1} range at 8 cm^{-1} resolution and peak identification by an in-house algorithm following baseline subtraction. [78] Raman is insensitive to oxalate even at high concentration; this is a cross-section limitation of the technique, not a sample problem, so those species are identified by carbon-13 NMR instead and do not enter the carbon balance.

Destruction above 99.99% leaves the residual parent compound near the detection limit. Parent compound was quantified by LC-MS/MS at a detection limit of 0.1 µg/L. Analysis used a tandem quadrupole instrument coupled to a Waters 2795 Alliance HT LC system (Waters, Milford, MA), with a Zorbax Eclipse XDB-C18 column and an ammonium acetate mobile phase. Ion chromatography with conductivity detection (IC-CD; Dionex ICS-1000 with AERS 500 suppressor and an IonPac AS9-HC column, 9 mM Na_2CO_3 mobile phase) was used for fluoride

and sulfate, and is the defluorination method of record. Fluoride was also measured by ion-selective electrode (F-ISE; Orion 9609BNWP, Thermo Scientific) buffered in TISAB 2, but the ISE deviates from IC-CD at high NaOH and NaCl because of matrix effects on the electrode response, occasionally reporting apparent defluorination above 100%, so IC-CD is preferred wherever the two disagree.

Carbon-13 and fluorine-19 NMR spectra were recorded on a Bruker 500 MHz spectrometer (470 MHz for fluorine-19 and 126 MHz for carbon-13), with samples prepared in deuterium oxide for the field lock and processed in TopSpin. NMR was used qualitatively for structural confirmation of intermediates. Total organic carbon analysis was used to close the total carbon pool where the speciated methods were insufficient.

Gas-phase products were analyzed by GC-MS (Agilent 5973) with a Rt-Q-BOND fused-silica capillary column. Products were identified by retention time and mass spectrum. Gas-phase species were not quantified. The signals shown in the gas-phase figures are not internal-standard corrected and are therefore semi-quantitative, comparable across a series only to the extent that the injection volume was reproducible. Spectra acquired in selected ion monitoring mode are not comparable in absolute intensity with full-scan spectra, so the two acquisition modes are compared only within themselves. Full scan was used for discovery and selected ion monitoring for targeted confirmation.

3.4 Data Analysis and Kinetics

Destruction and removal efficiency (DRE) was calculated from the initial and effluent parent-compound concentrations, Equation 3.1, with the parent concentration determined by Raman spectroscopy at intermediate conversions and by LC-MS/MS at high conversions.

$$DRE\ (\%) = \frac{(C_o - C_e)}{C_o} \times 100, \quad (3.1)$$

Where C_o and C_e are the feed and outlet parent-compound concentrations. Defluorination efficiency was calculated from measured fluoride relative to the fluorine content of the feed, Equation 3.2, with fluoride measured by IC-CD and, with the caveats above, by ISE.

$$DeF\ (\%) = \frac{Fluoride\ Conc.\ \text{in}\ Effluent}{Initial\ Fluorine\ Conc.\ \text{in}\ Feed} \times 100, \quad (3.2)$$

Elemental mass balances for fluorine, sulfur, and carbon were determined by comparing the sum of the element across all measured effluent species to the element delivered in the feed, applying a single consistent closure form to all three elements, Equation 3.3. [37] The specific effluent species summed in the numerator depend on the compound and are given in the corresponding chapters; for TFMS, for example, the sulfur balance sums residual TFMS and sulfate while the carbon balance sums residual TFMS, formate, and carbonate.

$$Element\ recovery\ (\%) = \frac{(sum\ of\ element\ in\ effluent\ products)}{(element\ in\ feed)} \times 100 \quad (3.3)$$

The apparent activation energy of global destruction was determined from an Arrhenius analysis of the observed rate constant across the temperature range studied, Equation 3.4, where the observed rate constant, pre-exponential factor, and global activation energy are obtained from the slope and intercept of the linear fit and R is the universal gas constant.

$$ln(k_{obs}) = ln(A) - \frac{E_{aG}}{RT}, \quad (3.4)$$

The dependence of the rate on hydroxide was represented by a power law in NaOH concentration, Equation 3.5, where the exponent is the reaction order with respect to hydroxide. Because density data for concentrated NaOH at these hydrothermal conditions are unavailable, the in-situ hydroxide molarity in the two-phase regime cannot be determined precisely, and reaction orders that depend on that molarity are reported with that limitation stated.

$k_{obs}=k[NaOH]^n$, (3.5)

The pump flow rate was set by mass conservation, Equation 3.6, from the reactor volume, the fluid densities at the hot reacting and cold feed conditions, and the target residence time.[74]

$$Q_{pump} = \frac{V_{reactor} \times \rho_{hot}}{\tau_{res} \times \rho_{cold}} \quad (3.6)$$

3.5 Computational Methods

Two separate sets of density functional theory calculations were performed, differing in software, level of theory, and provenance. The calculations supporting the TFMS thermal-degradation pathway were performed by a collaborator using the Gaussian16 software suite, with geometries and thermochemistry computed at the M06-2X/6-311+G(d,p) level of theory, selected for its accuracy for the thermal properties of main-group elements. Temperature and pressure corrections were applied to match experimental conditions, an implicit polarizable continuum model with a static dielectric constant of 4.2 was used, and transition-state structures were verified by a single imaginary vibrational frequency. These calculations were performed in collaboration with the Vyas Research Group at the Colorado School of Mines.

The calculations supporting the PFPrA and PFBA elimination pathways were performed by the author using ORCA 6.1.1 on a Windows workstation with MS-MPI for parallel execution. Geometries were optimized with the range-separated hybrid functional ωB97X-D3, which combines a long-range-corrected exchange treatment with Grimme's D3 dispersion correction using zero damping. The range separation improves the description of long-range exchange, which is important for the charged and polar species considered here, and the dispersion correction accounts for weak interactions the underlying functional does not capture. This functional is a well-established choice for main-group reaction thermochemistry and barrier heights. [81]

The ma-def2-TZVP basis set was used for all atoms. This triple-zeta valence basis with minimal augmentation provides the diffuse functions needed to describe the anionic species accurately, whose electron density is more diffuse than that of neutral molecules. The resolution-of-identity approximation was applied with the def2/J auxiliary basis, and the chain-of-spheres approximation to the exchange (RIJCOSX) was used to reduce cost without meaningful loss of accuracy. Aqueous solvation was described with the SMD implicit solvent model using water as the solvent, representing the condensed-phase environment through a continuum without explicit water molecules. [82, 83]

Two reaction models were considered for each fragment. In the first, base-assisted elimination was modeled from the neutral 1H-perfluoroalkane with an explicit hydroxide ion serving as the base, giving a total system charge of negative one; this model represents the concerted route in which proton abstraction and fluoride departure occur together. In the second, elimination was modeled directly from the perfluoroalkyl carbanion, again with a total charge of negative one; this model represents the stepwise route in which the carbanion, formed by prior deprotonation, expels a fluoride without further assistance from the base. The two models correspond to alternative mechanistic pathways to the same alkene product rather than to sequential steps of a single pathway.

Transition states were located by first performing relaxed surface scans along the breaking carbon-fluorine coordinate, then optimizing the energy maximum of each scan to a first-order saddle point. Each transition state was confirmed by a single imaginary vibrational frequency corresponding to the reaction coordinate, that is, to carbon-fluorine bond cleavage and, in the base-assisted model, the associated proton transfer. Three structures carry an additional small imaginary mode below 51 cm^{-1} that does not correspond to the reaction coordinate and contributes negligibly to the Gibbs

free energy; these are identified in Appendix A.3. Each reactant was confirmed as a minimum by the absence of significant imaginary frequencies. Gibbs free energies were obtained from analytical frequency calculations at 298.15 K, and activation free energies are reported as the difference in Gibbs free energy between the transition state and the corresponding reactant. Cartesian coordinates and absolute energies in hartrees for all stationary points are provided in Appendix A.

Chapter 4: Destruction of Trifluoromethanesulfonic Acid (TFMS)

4.1 Introduction

TFMS (CF_3SO_3H) is the C_1 PFSA and the most structurally reduced member of the PFSA class. It serves in this dissertation as both a mechanistic probe for the regulated PFSAs, which share the sulfonic head group attached to a fluorinated carbon chain, and as an extreme test case for the expanded alkaline hydrolysis regimes, because with a single perfluorinated carbon it offers no sites for carbon-carbon bond cleavage and therefore represents the recalcitrant limit of the class.[41]

TFMS is a persistent environmental contaminant; it has been detected in aqueous film-forming foams and in AFFF-impacted groundwater at military bases,[42] in the large majority of German drinking-water sources,[84] and in surface waters in China and Sweden.[14, 85] TFMS presence in human umbilical cord blood, and hazard assessments based on persistence, mobility, bioaccumulation, and toxicity have ranked it above PFOS despite its lower bioaccumulation potential. [14, 42, 84-86] Preliminary experiments under conventional AH conditions confirmed its recalcitrance. Across 1 to 5 M NaOH at 350 °C and 25 MPa, with a residence time of roughly 8 minutes, TFMS conversion rose with alkalinity but never went to completion: even at 5 M NaOH approximately 13% of the TFMS remained, and the carbon released was distributed between formate and carbonate rather than fully mineralized (Figure 4.1). This is consistent with the high alkaline demand reported for other PFSAs and defines the limitation the expanded regimes were developed to address.[35]

4.2 Experimental Approach

Preliminary experiments were performed under conventional alkaline hydrolysis to establish a baseline against which the expanded regimes could be compared. These runs were performed at 350 °C and 25.0 MPa with a residence time of approximately 8 minutes, with NaOH varied from

1.0 to 5.0 M and no sodium chloride added to the reagent stream (Figure 4.1). TFMS was processed in the 4.2 mL continuous-flow Inconel 600 reactor described in Chapter 3 at a feed concentration of 0.025 M, with NaOH varied from 0 to 2.0 M and 3 wt% NaCl present in the reagent stream. The SIM-AH experiments were run at 30.0 MPa and 350, 380, and 400 °C, all subcritical for the 3 wt% NaCl solution, giving NaOH-to-TFMS molar ratios from 0:1 to 80:1. The DAH experiments were run at 400 °C and 0.5 M NaOH with pressure reduced from 30.0 MPa into the two-phase region at 24.8 and 20.0 MPa, and a further set at 350 °C near 13.8 to 14.5 MPa. Destruction was quantified by Raman spectroscopy and, at high conversion, by LC-MS/MS with external calibration against a native TFMS standard from Wellington Laboratories; defluorination by IC-CD and F-ISE; and sulfur and carbon products by Raman and IC-CD, with the method caveats of Chapter 3 applied throughout.

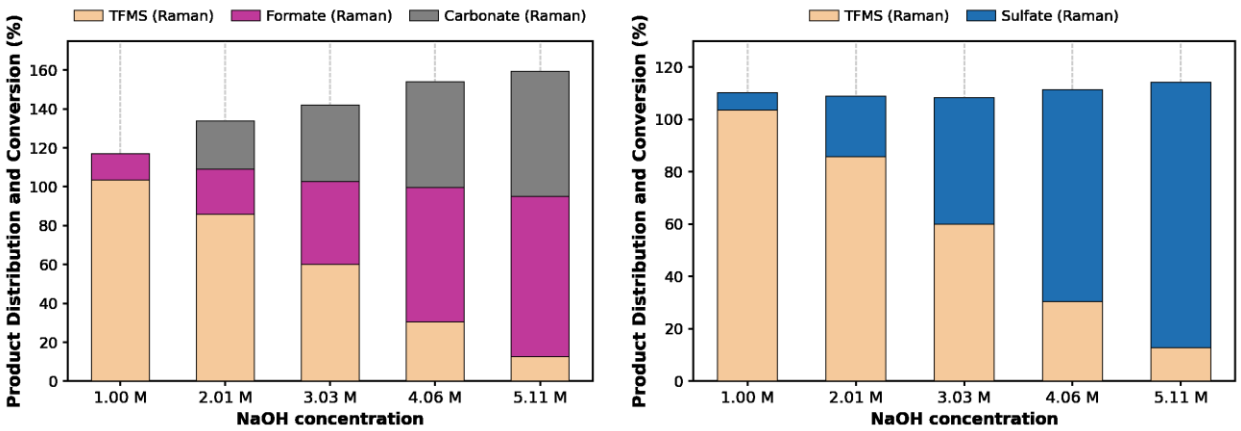

Figure 4.1: Product distribution and conversion for TFMS under conventional alkaline hydrolysis at 350 °C and 25 MPa with a residence time of approximately 8 minutes, as a function of NaOH concentration from 1 to 5 M. Left: carbon balance showing residual TFMS, formate, and carbonate. Right: sulfur balance showing residual TFMS and sulfate. All species quantified by Raman spectroscopy. Approximately 13% of the TFMS remains at 5 M NaOH.

4.3 Results

4.3.1 Phase Behavior and Definition of the Operating Regimes

Both expanded regimes derive from the phase behavior of the H_2O-NaCl system. Pure water reaches its critical point at 374 °C and 22.1 MPa, above which it enters the supercritical state and

can no longer sustain the high density and ionic solvation that alkaline hydrolysis requires. Adding a non-volatile electrolyte raises this boundary. Figure 4.2 shows the critical curve of the H_2O-NaCl system computed from the Driesner and Heinrich correlation as a function of NaCl content.

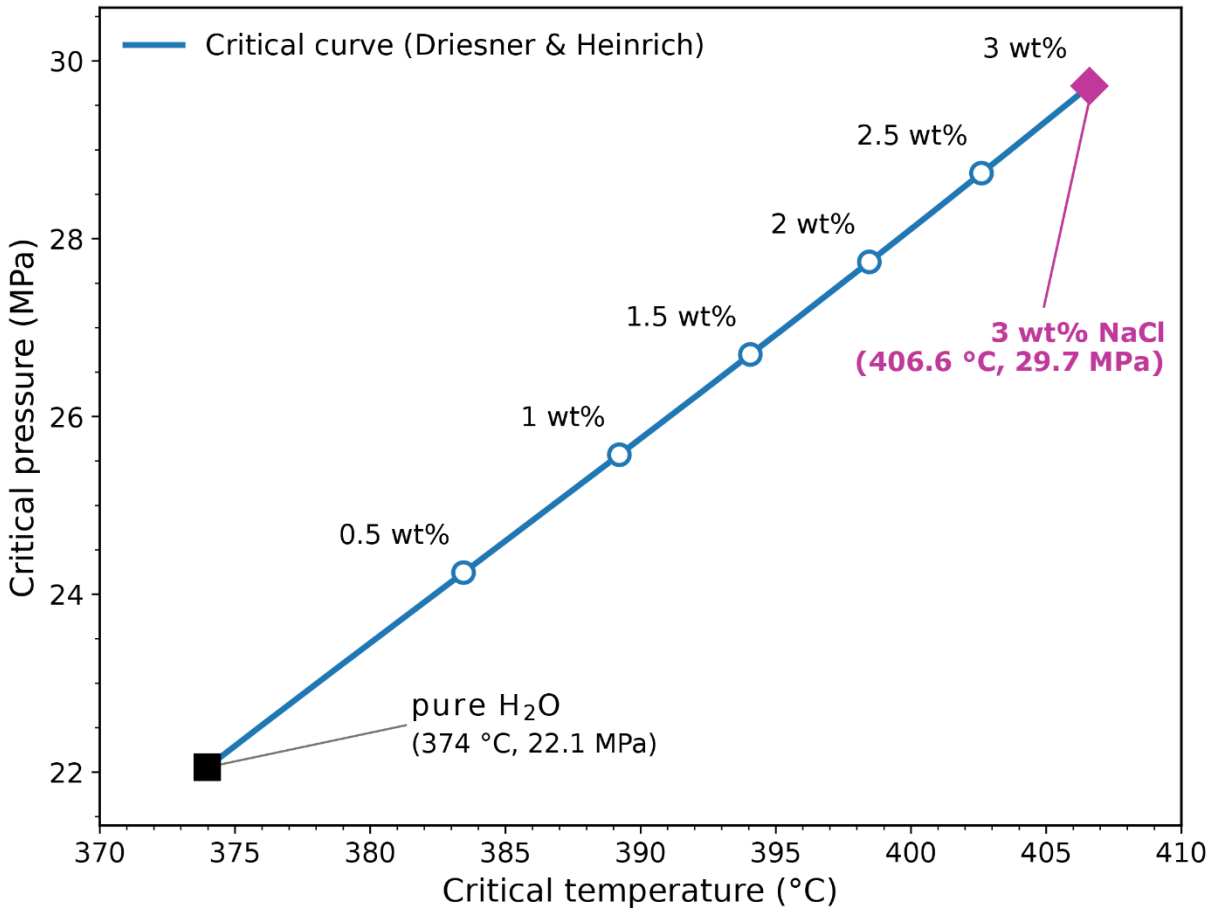

Figure 4.2: Critical curve of the H_2O-NaCl system computed from the Driesner and Heinrich correlation, showing the shift in the critical point with NaCl wt%. At 3 wt% NaCl, the critical point shifts from that of pure water (374 °C, 22.1 MPa) to 406.6 °C and 29.7 MPa. This shift is the thermodynamic basis for operating alkaline hydrolysis at elevated temperature while remaining subcritical.

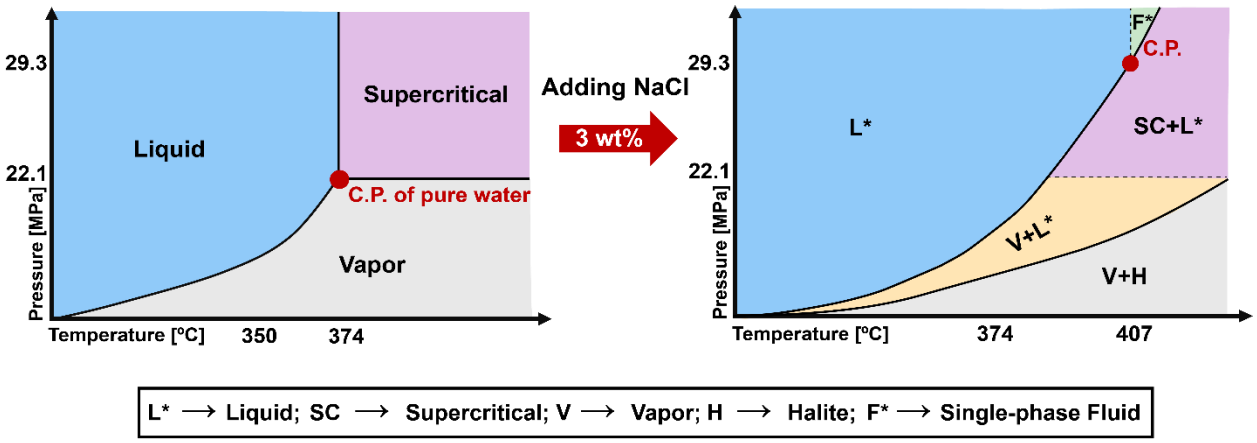

Figure 4.3: Water phase diagram with electrolyte addition. Left: pure water, with the red circle marking the critical point of pure water (374 °C, 22.1 MPa), with conventional AH operating at 350 °C in the compressed-liquid (L) region. Right: the H_2O-NaCl (3 wt%) phase diagram, for which the critical point shifts to 406.6 °C and 29.7 MPa, enabling subcritical operation at elevated temperature (L*) and access to a two-phase vapor-liquid (V+L*) or supercritical-liquid (SC+L*) region where partial water evaporation concentrates alkali in the liquid phase. L*: liquid; SC: supercritical; V: vapor; H: halite; F*: single-phase fluid; C.P.: critical point.

4.3.2 Destruction and Defluorination under SIM-AH

Figure 4.4 presents TFMS destruction and defluorination at 350, 380, and 400 °C across NaOH concentrations from 0 to 2 M.

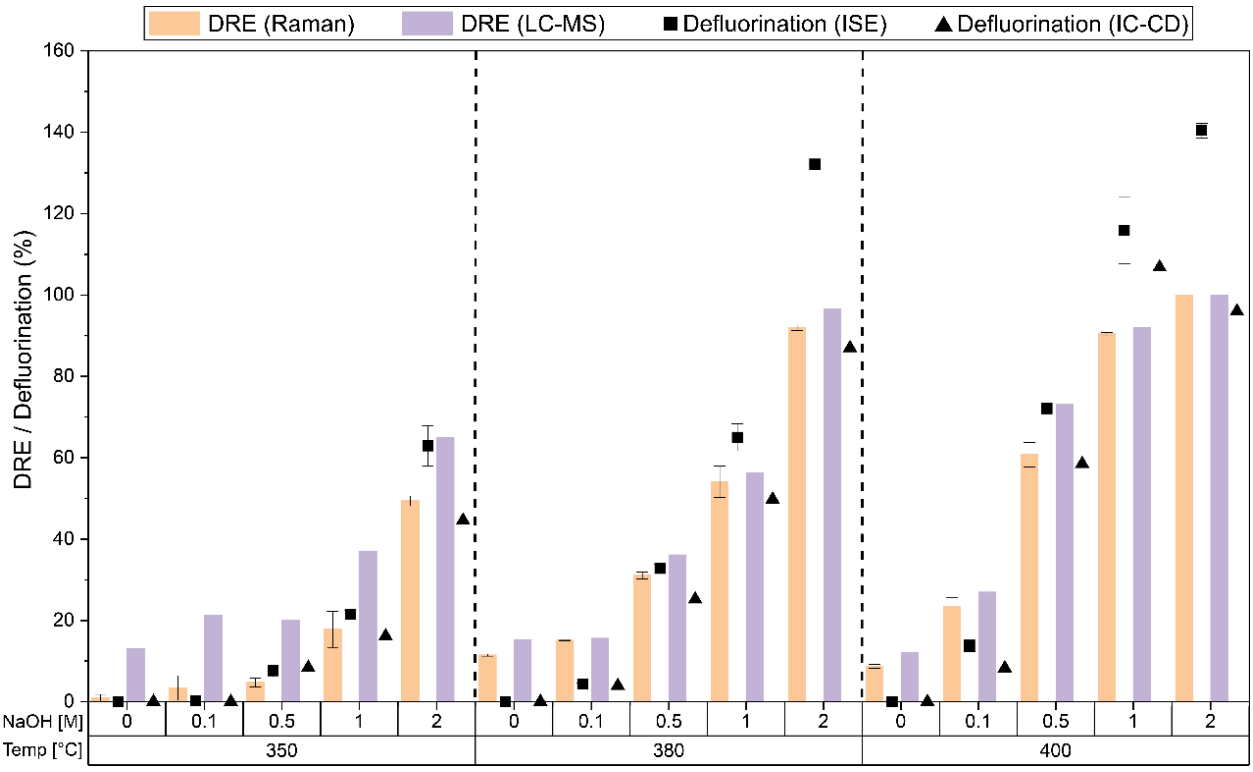

Figure 4.4: TFMS DRE and defluorination during SIM-AH at 350, 380, and 400 °C with varying amendment concentration (0, 0.1, 0.5, 1, and 2 M NaOH), residence time approximately 10 minutes. TFMS destruction was determined by both Raman and LC-MS/MS analysis. Defluorination efficiency was quantified by F-ISE and IC-CD. Error bars represent the spread between duplicate measurements.

Both DRE and defluorination increase with temperature and with NaOH concentration. At 380 °C and 2 M NaOH, DRE and defluorination reach 92 and 86% respectively (by IC-CD), and the methods converge further at 400 °C and 2 M NaOH. Two features are important for the mechanism developed later. First, a small amount of DRE, 6 to 11%, occurs at 380 and 400 °C even with no NaOH present, which indicates a thermal degradation pathway independent of hydroxide-driven nucleophilic substitution. Second, defluorination consistently lags destruction at low NaOH, then closes the gap as NaOH rises, which indicates that fluorinated organic intermediates form first and require sufficient alkali to be converted to fluoride. The fluoride measured by F-ISE runs higher than by IC-CD and occasionally exceeds 100% at the highest temperature and alkalinity, an artifact of matrix effects on the electrode at high ionic strength, so IC-CD is treated as the defluorination method of record throughout.

4.3.3 Product Distribution: Sulfur and Carbon Balances

Figure 4.5 resolves the sulfur inventory as a stacked balance of residual TFMS and sulfate across the same conditions.

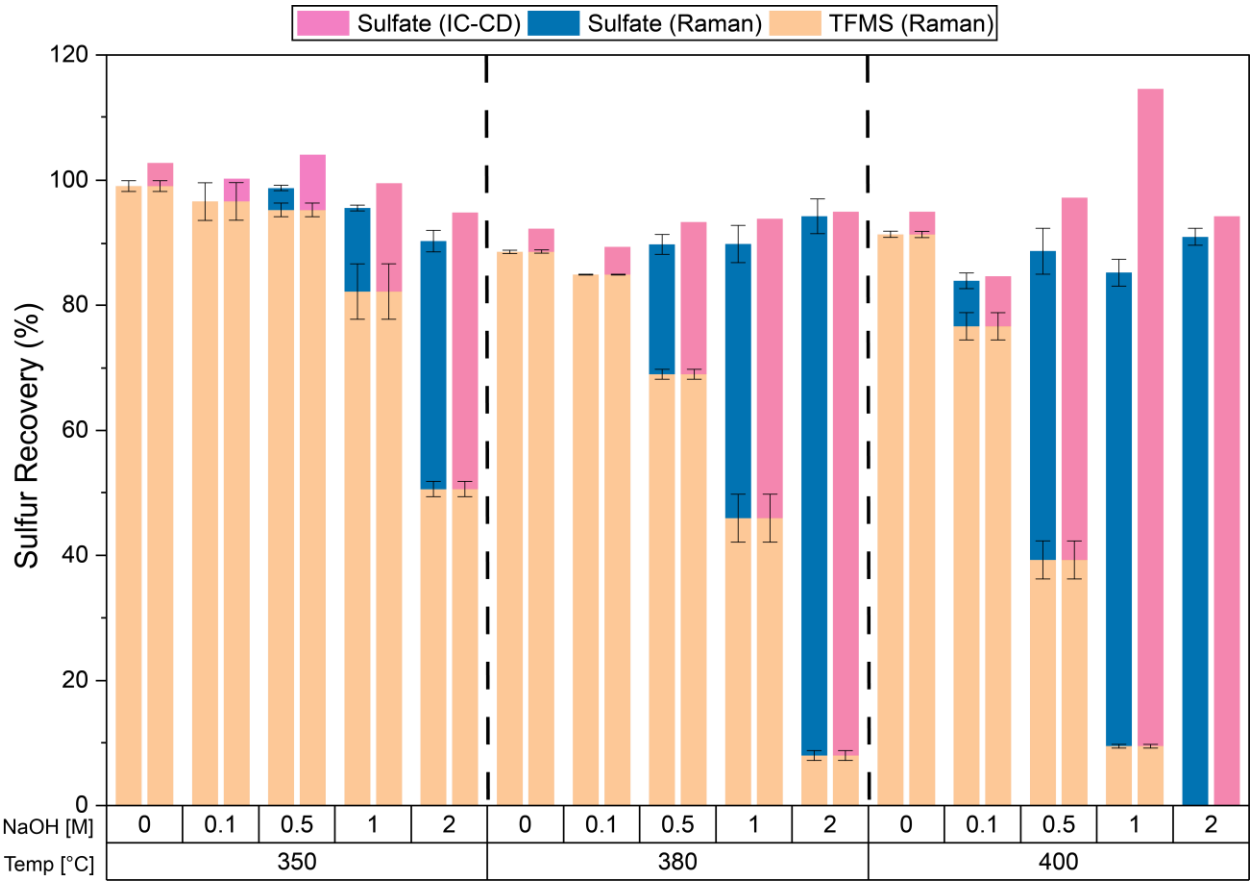

Figure 4.5: Sulfur balance during TFMS degradation under SIM-AH at 350, 380, and 400 °C with varying NaOH levels (0, 0.1, 0.5, 1, and 2 M), residence time approximately 10 minutes. Stacked bars represent sulfur-containing products: sulfate measured by Raman (blue) and IC-CD (pink), with residual TFMS measured by Raman. Error bars represent the difference between duplicate measurements.

The sulfonic head group is converted primarily to sulfate. At 350 °C and 2 M NaOH, 37.9% of sulfur is recovered as sulfate with 49.4% remaining as unreacted TFMS, and sulfate formation rises with temperature to roughly 89% at 380 °C and 90% at 400 °C at 2 M NaOH. Sulfate quantified by Raman agrees with IC-CD to within 7% across all conditions, and total sulfur recovery ranges from 85 to 95%, confirming that sulfate is the terminal sulfur product. Figure 4.6 shows the carbon balance as residual TFMS, formate, and carbonate.

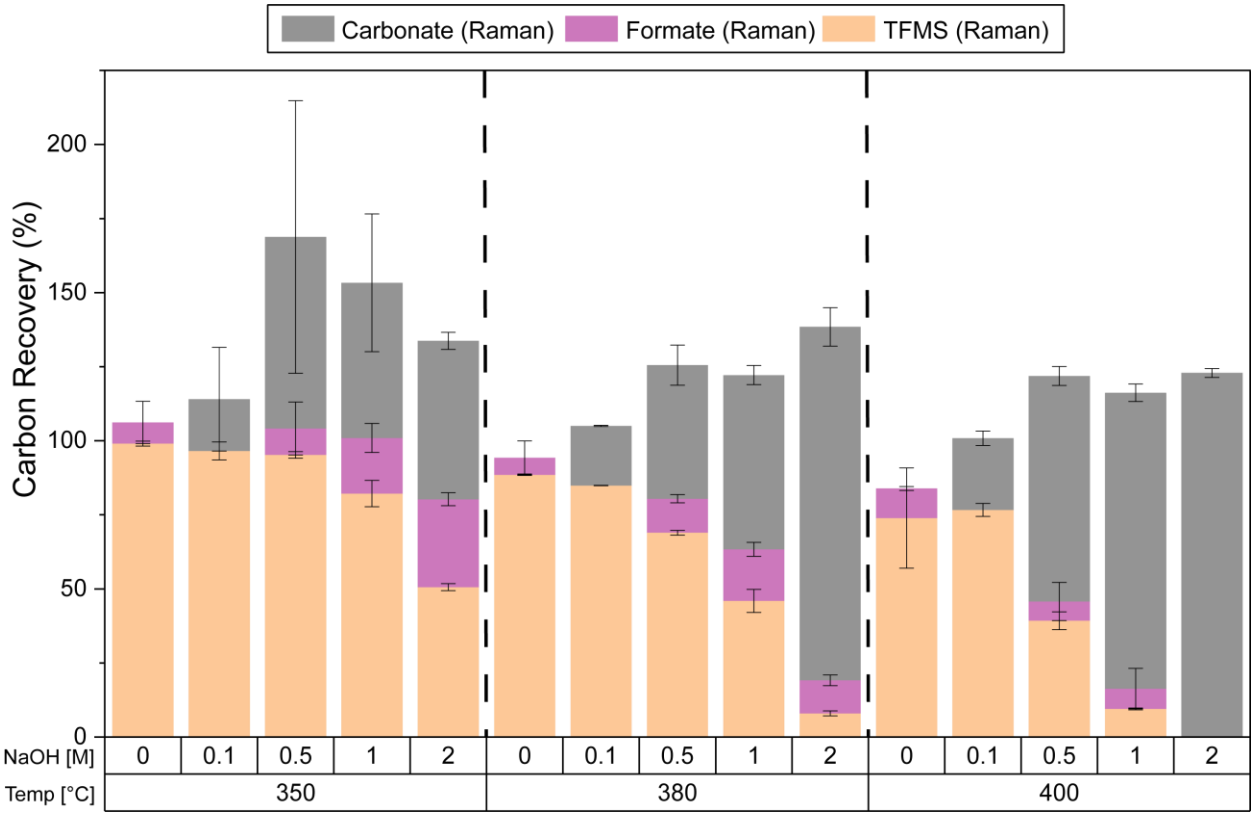

Figure 4.6: Carbon balance during TFMS degradation under SIM-AH at 350, 380, and 400 °C with varying alkalinity (0, 0.1, 0.5, 1, and 2 M NaOH), residence time approximately 10 minutes. Stacked bars represent carbon-containing products: residual TFMS (orange), formate (purple), and carbonate (gray), all measured by Raman. Error bars represent the average difference between duplicate measurements.

At 350 °C and 2 M NaOH, residual TFMS accounts for 11.8% of carbon while formate and carbonate make up 31.8 and 56.4%. As temperature rises, carbonate becomes dominant and formate declines, and at 400 °C formate is essentially absent across all NaOH concentrations. This progression identifies formate as an intermediate that mineralizes to carbonate at elevated temperature, consistent with formic acid decomposition kinetics reported for hydrothermal systems. Carbon recovery exceeds 100% at the highest NaOH concentrations. This is attributable to carbonate carried into the reactor by the alkaline stock, which takes up atmospheric carbon dioxide during handling, rather than to a true over-recovery. The offset scales with the NaOH loading, which is why it becomes apparent only at the highest concentrations.

4.3.4 Evidence for a Thermal Pathway

The small hydroxide-independent destruction noted in Figure 4.4 points to a second, thermally driven route that operates when alkali is limited. Gas-phase analysis of the no-NaOH experiments identifies its product directly. Figure 4.7 shows the GC-MS detection of fluoroform (CHF_3) from TFMS processed at 400 °C in the absence of NaOH amendment.

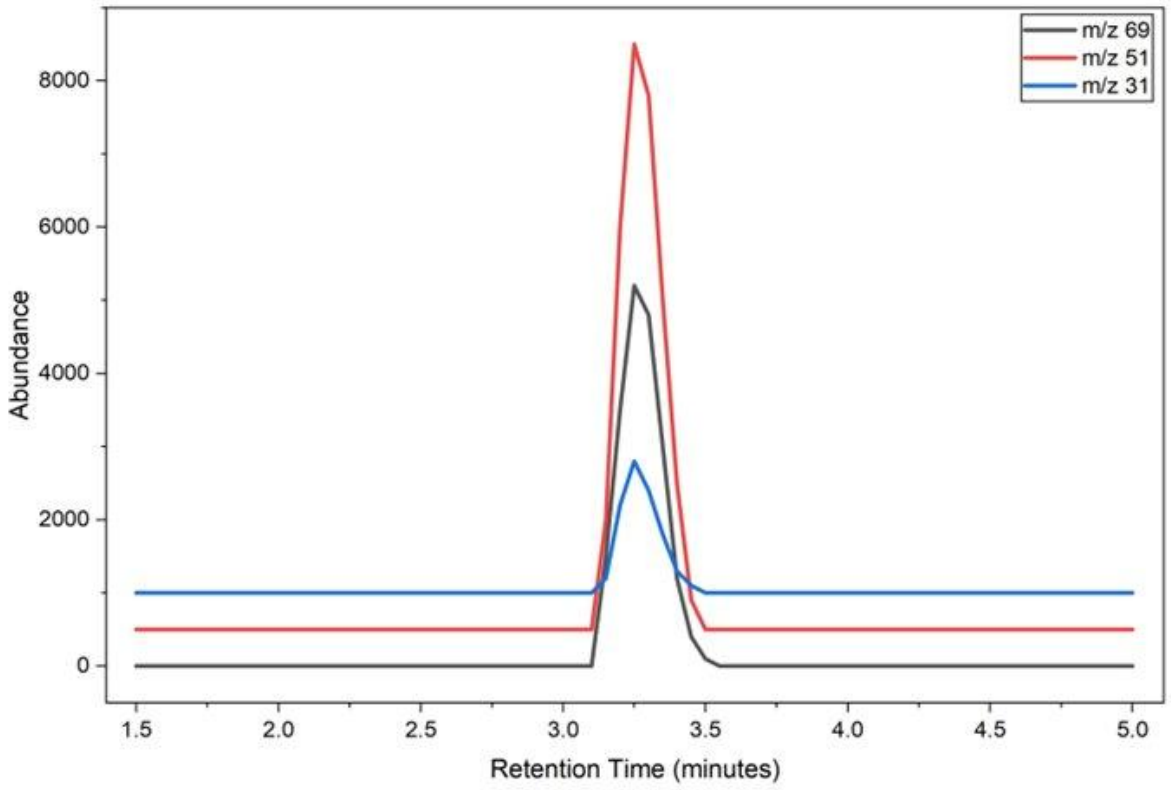

Figure 4.7: GC-MS detection of fluoroform (CHF_3) from TFMS degradation at 400 °C under non-alkaline conditions (0 M NaOH, 0.025 M TFMS, 30.0 MPa, residence time approximately 10 min). Characteristic fragments appear at m/z 69 (CF_3^+), 51 (CHF_2^+), and 31 (CF^+) at a common retention time of approximately 3.2 min. Fluoroform was not detected at 350 or 380 °C, nor at any temperature in the presence of NaOH, indicating a thermally driven pathway that operates only when hydroxide is limited.

The characteristic fragments at m/z 69, 51, and 31 confirm fluoroform, and its absence at 350 and 380 °C and in every NaOH-containing experiment shows that this thermal route becomes competitive only at the highest temperature when hydroxide is unavailable to react with the reactive intermediate. Because only about 11% of the TFMS is destroyed at 400 °C without NaOH,

fluoroform is a minor product. The mechanistic origin of fluoroform is examined in the Discussion using density functional theory.

4.3.5 Distillation Alkaline Hydrolysis

The SIM-AH results were obtained in the single-phase liquid region. Lowering the pressure at fixed temperature moves the system into the two-phase region defined in Figure 4.8, where the distillation regime operates.

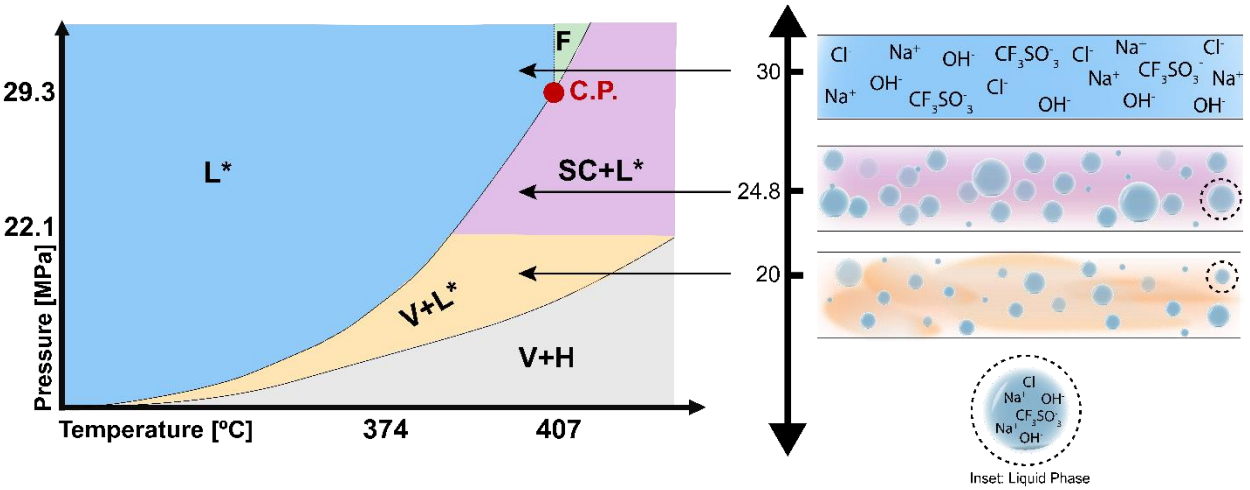

Figure 4.8: H_2O-NaCl phase diagram for the distillation regime. At 400 °C and 30.0 MPa the system operates in the single-phase liquid (L*) region. Reducing the pressure to 24.8 MPa enters the supercritical-liquid (SC+L*) region and to 20.0 MPa the vapor-liquid (V+L*) region, where water partitions into the low-density phase and alkali concentrates in the residual liquid. The inset depicts the enriched liquid phase.

Holding temperature and initial NaOH fixed and reducing only the pressure isolates the effect of phase separation. Figure 4.9 compares the product distribution at 400 °C and 0.5 M NaOH across single-phase SIM-AH at 30.0 MPa and two-phase DAH at 24.8 and 20.0 MPa.

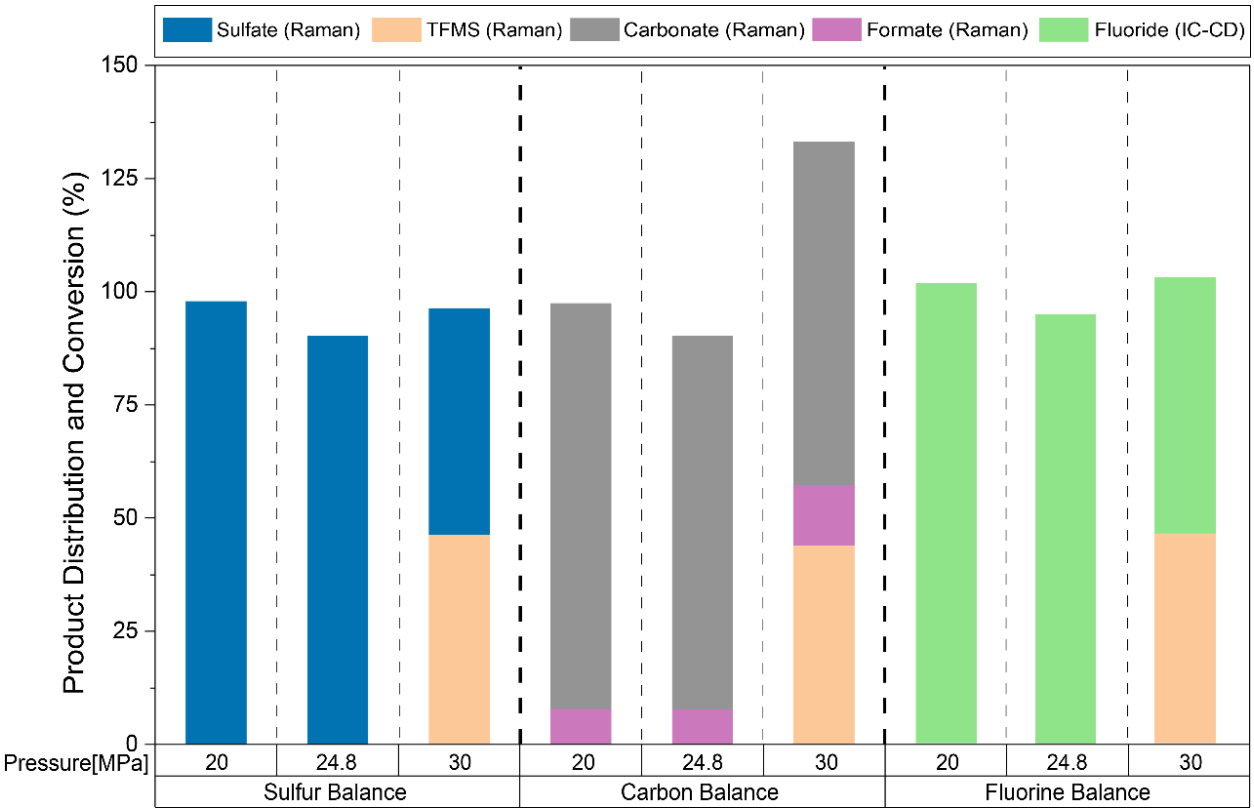

Figure 4.9: Product distribution and TFMS degradation at 400 °C comparing two-phase SC+L* and V+L* DAH (0.5 M NaOH, 20.0 and 24.8 MPa) with single-phase SIM-AH (0.5 M NaOH, 30.0 MPa). Sulfur, carbon, and fluorine balances are shown at constant pump flow rate with varying system pressure. Stacked bars show the product distribution measured by Raman spectroscopy; fluoride was measured by IC-CD (green bars).

At 30.0 MPa and 0.5 M NaOH the single-phase system destroys approximately 57% of the TFMS, with 44% of carbon remaining as unreacted TFMS. Reducing the pressure to 24.8 and 20.0 MPa raises the DRE to 99.98%, and TFMS is not detected in the effluent at either two-phase pressure. Carbonate becomes the dominant carbon product at 83 to 90% with formate below 10% and no residual TFMS. Because the only variable changed is pressure, the sharp increase in destruction is a direct consequence of the in situ NaOH enrichment that accompanies phase separation. Both two-phase pressures reached complete destruction, but they differ in operating margin. At 400 °C with 3 wt% NaCl the vapor-halite boundary lies near 17.7 MPa, so operation at 20.0 MPa remains in the V+L* region with margin above halite precipitation, whereas 24.8 MPa enters the SC+L* region where the supercritical phase carries the corrosion behavior that subcritical operation was

chosen to avoid. The V+L* condition at 20.0 MPa is therefore the more favorable window for reactor integrity. A second comparison, in Figure 4.10, tests this at 350 °C against conventional aqueous AH.

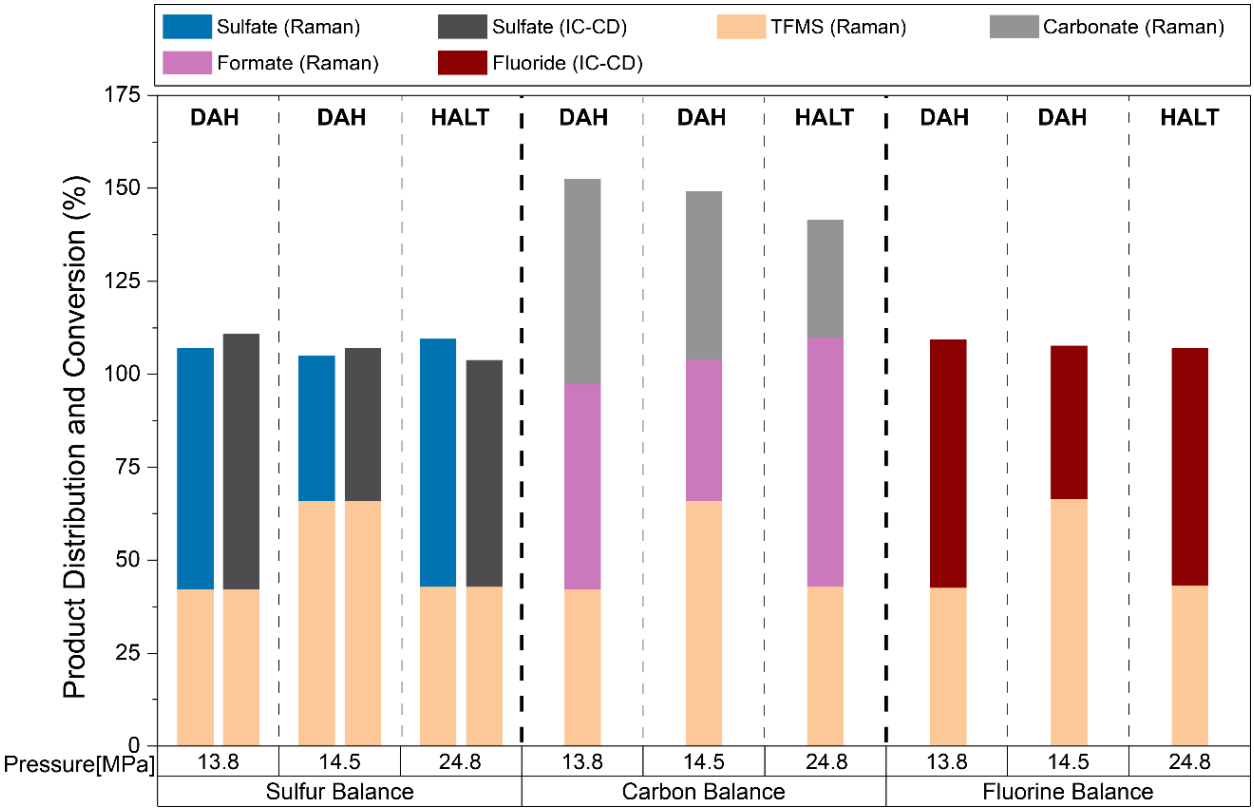

Figure 4.10: Product distribution and TFMS degradation in DAH (V+L*) versus conventional AH. Operating conditions are 350 °C, residence time approximately 3 minutes; DAH at 0.5 M NaOH and 13.8 to 14.5 MPa, and aqueous AH at 5 M NaOH and 24.8 MPa. Sulfur, carbon, and fluorine balances are shown with stacked bars from Raman spectroscopy and IC-CD; fluoride was measured by IC-CD (dark red bars). The DAH conditions correspond to the two-phase region where in situ alkali enrichment occurs, while AH operates in compressed-liquid conditions.

Here the two-phase DAH case at 0.5 M NaOH and the single-phase AH case at 5 M NaOH reach similar DRE, approximately 30 to 50%, with sulfur mass balances closing within uncertainty in both, despite the DAH initial NaOH loading being ten-fold lower. Figures 4.9 and 4.10 show that reducing pressure to induce phase separation concentrates hydroxide enough to match, at one-tenth the initial alkali, the destruction otherwise requiring a fully aqueous high-NaOH throughput.

4.4 Discussion

4.4.1 Degradation Mechanism and the Role of Hydroxide

The product distributions point to two competing routes, one dominant under alkaline conditions and one thermal route that appears only when hydroxide is limited. The detection of fluoroform in Figure 4.7 raises the specific question of whether the thermal route proceeds through a radical (homolytic) or an anionic (heterolytic) pathway. Figure 4.11 compares the two using density functional theory energy profiles.

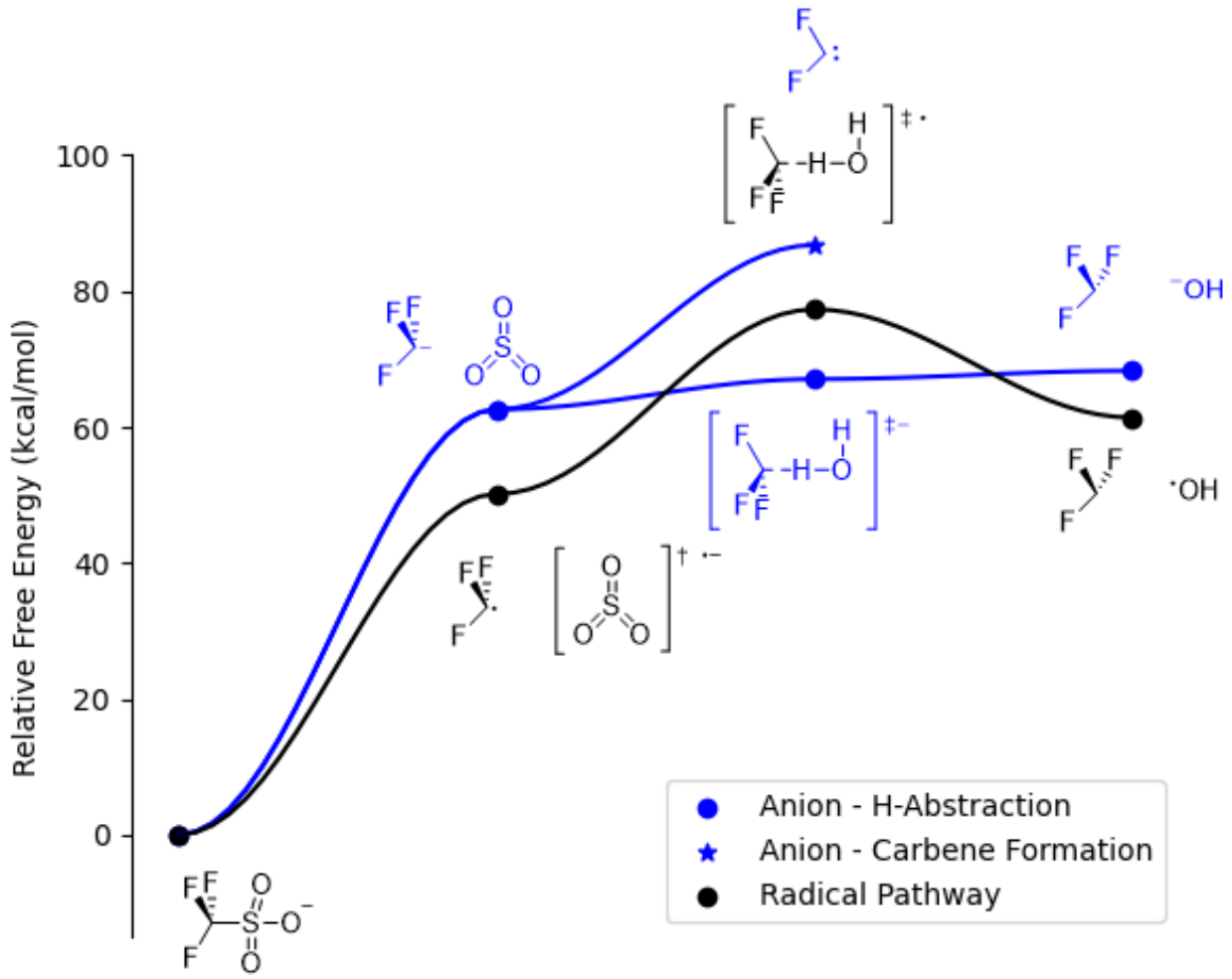

Figure 4.11: DFT energy profiles for TFMS thermal degradation pathways in the absence of hydroxide. Comparison of the anionic pathway (blue) via the trifluoromethyl anion with proton abstraction and carbene formation, versus the radical pathway (black) via the trifluoromethyl radical. Relative energies (kcal/mol) are plotted along the reaction coordinate with key intermediates and transition states shown. The anionic mechanism presents the lower barrier.

The calculations identify heterolytic cleavage of the C-S bond as the rate-determining step of the thermal route, with a barrier of 62.58 kcal/mol, producing the trifluoromethyl anion and a sulfur-oxide leaving group. From the trifluoromethyl anion, proton abstraction from water leads to fluoroform through a pathway that reaches 67.04 and 68.25 kcal/mol, whereas the competing direct carbene formation reaches 86.77 kcal/mol and the homolytic radical pathway peaks at 77.29 kcal/mol. Because the proton-abstraction route lies well below both alternatives, fluoroform forms as the terminal product of thermal degradation when hydroxide is limited, which explains its detection only at 400 °C with no NaOH.

Under alkaline conditions a base-catalyzed pathway accounts for the observed mineralization, and it agrees with the mechanism reported independently by Hao et al. for TFMS under different hydrothermal conditions. Figure 4.12 summarizes both routes.

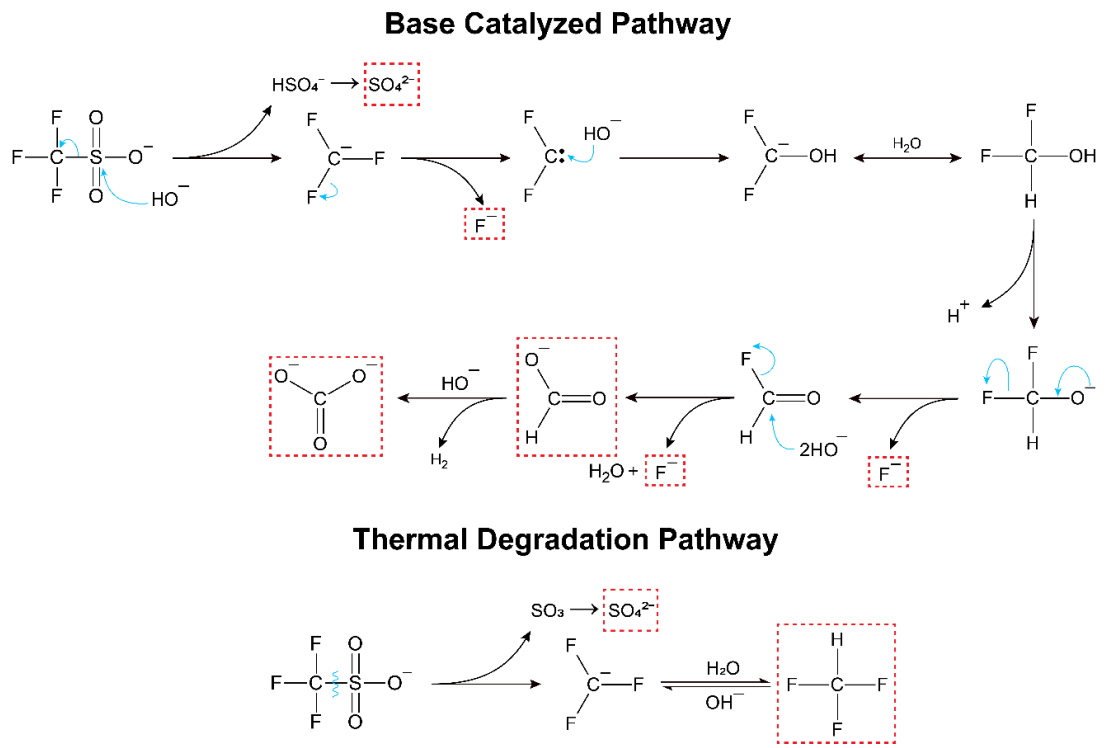

Figure 4.12: Combined degradation mechanism for TFMS. (a) Base-catalyzed pathway: hydroxide-mediated C-S bond cleavage, sequential defluorination through a formate intermediate, and complete mineralization to fluoride, carbonate, and sulfate. (b) Thermal pathway at 400 °C without NaOH: heterolytic C-S cleavage followed by proton abstraction from water to form fluoroform as the terminal product.

In the base-catalyzed route, hydroxide attacks the C-S bond and cleaves it to release sulfate and the trifluoromethyl anion; the anion defluorinates stepwise through a difluorocarbene intermediate, which reacts with hydroxide and water through sequential HF elimination and hydroxide attack to yield formate, which is then converted to carbonate, releasing hydrogen. This stepwise cascade explains the lag of defluorination behind DRE seen in Figure 4.4, because each C-F bond must be broken in turn, and it explains why higher hydroxide narrows that gap. The sulfate, carbonate, and fluoride identified in the balances are the terminal products of this route, while the thermal route in panel (b) diverts carbon to fluoroform when hydroxide is unavailable.

4.4.2 Kinetic Analysis

The temperature and hydroxide dependence of DRE can be quantified from the same data set. Figure 4.13 presents the Arrhenius analysis and the hydroxide-order analysis.

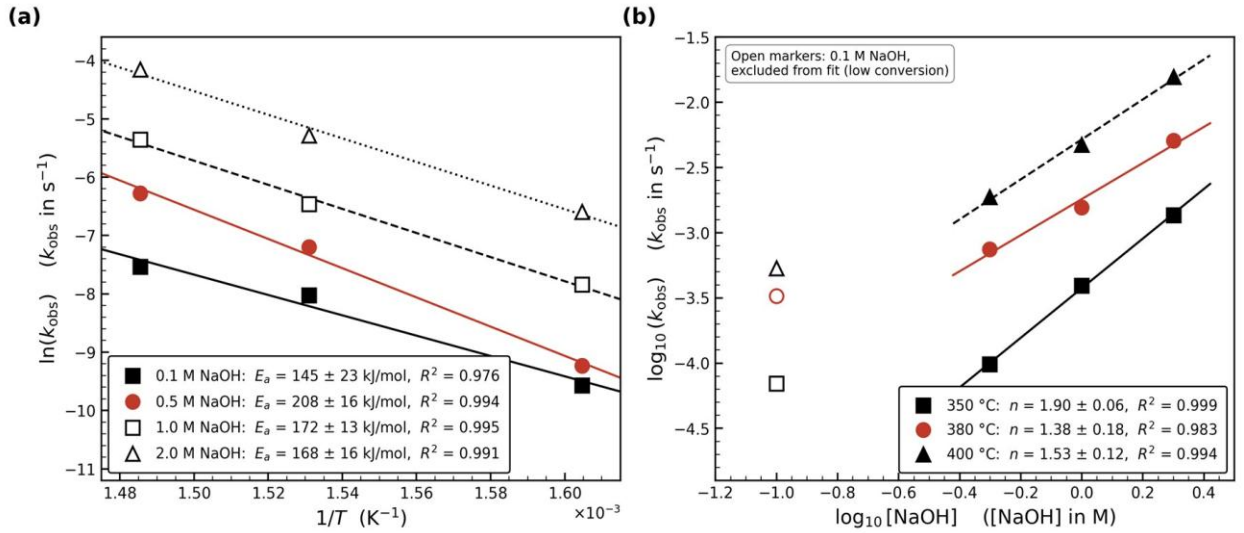

Figure 4.13: Kinetic analysis of TFMS degradation under SIM-AH conditions. Left: Arrhenius analysis of ln(k) versus 1/T at 0.1 M (filled black squares), 0.5 M (filled red circles), 1.0 M (open black squares), and 2.0 M (open triangles) NaOH. Right: hydroxide dependence of log10(k) versus log10[NaOH] at 350 °C (filled black squares), 380 °C (filled red circles), and 400 °C (filled black triangles); open markers denote the 0.1 M NaOH points, excluded from the fit due to low conversion.

The Arrhenius fits give apparent activation energies of 145 ± 23 kJ/mol at 0.1 M, 208 ± 16 kJ/mol at 0.5 M, 172 ± 13 kJ/mol at 1.0 M, and 168 ± 16 kJ/mol at 2.0 M NaOH, an overall range of 145

to 208 kJ/mol with uncertainties reflecting the standard error of the fits. These values are placed alongside those for the PFCAs and the literature in Section 6.1. A substantially lower value of 55 kJ/mol has been reported for PFOS degradation with $NaHCO_3$,[87] although that system used a different alkaline source and reaction medium. The hydroxide-order analysis gives apparent reaction orders of 1.38 to 1.90 across the temperature range; because density data for concentrated NaOH at these conditions are unavailable, the in-situ hydroxide molarity cannot be determined precisely, so the order is reported as lying between first and second order rather than assigned a single integer value. Including the 0.1 M point shifts the apparent order closer to unity. At low NaOH in a continuous-flow reactor at short residence time, diffusion of reagents and products may limit NaOH availability, so the low-concentration points are the least reliable. This behavior is consistent with hydroxide acting both as the nucleophile in C-S cleavage and as a base catalyst in the subsequent defluorination steps.

The two regimes reduce the alkaline demand by different routes. SIM-AH raises temperature by shifting the critical point, accelerating destruction at fixed alkali, while DAH concentrates hydroxide in situ by phase separation, reaching comparable destruction at an order-of-magnitude lower initial alkali loading, as Figures 4.9 and 4.10 show. These are reported here as characterized outcomes of the phase behavior of the electrolyte-water system rather than as an engineering objective; their practical implication is that the reagent and neutralization burden of destroying a highly recalcitrant PFSA can be reduced 2.5- to 10-fold, and the reduction in total NaOH proportionally lowers the associated chlor-alkali greenhouse-gas footprint, while the elevated total dissolved solids of the effluent remains a consideration common to all high-salt hydrothermal approaches.

4.5 TFMS Transformation Summary

TFMS, the recalcitrant limit of the PFSA class, was mineralized in both expanded regimes at 2.5- and 10-fold lower alkali demand. SIM-AH achieved DRE above 99.9% with 2 M NaOH at approximately 10 min residence time, a 2.5-fold reduction in alkali demand relative to conventional operation at 5 M, and DAH achieved DRE above 99.99% with 0.5 M NaOH at 400 °C, a 10-fold reduction. Product analysis identified sulfate, carbonate, and fluoride as terminal products, with formate as a temperature-sensitive intermediate. The detection of fluoroform under low alkalinity revealed a competing thermal pathway, and density functional theory established heterolytic C-S bond cleavage as the rate-determining step, with nucleophilic substitution by hydroxide controlling degradation under alkaline conditions and thermal heterolysis becoming competitive only when hydroxide is limited.

Chapter 5: Destruction of Ultrashort- and Short-Chain PFCAs (PFPrA and PFBA)

5.1 Introduction

Perfluorobutanoic acid (PFBA, C_3F_7COOH) and perfluoropropanoic acid (PFPrA, C_2F_5COOH) are four- and three-carbon perfluorocarboxylic acids. Both were adopted as replacements during the phase-out of PFOA and PFOS. Both are highly water-soluble, poorly captured by the granular activated carbon and ion-exchange media used in conventional treatment. These PFCA have been increasingly detected in industrial wastewater and at environmental remediation sites as terminal transformation products of larger precursors. [5, 6, 8]

These two acids are studied together because they form a matched pair that isolates the effect of a single carbon PFCA (TFA). Under conventional single-phase alkaline hydrolysis, both are destroyed to comparable extents, yet PFBA experiments yield near-complete defluorination by 225 to 250 °C while PFPrA reaches only 41% at 250 °C and at matched NaOH loading; PFBA requires 275 to 300 °C to reach comparable defluorination rates. Because the two differ only in chain length, the study isolates a chemical pathway that emerges after the parent acid is destroyed.[76]

5.2 Experimental Approach

Both acids were processed under conventional single-phase alkaline hydrolysis, without the electrolyte modulation or phase separation used for TFMS, in a continuous-flow reactor that followed the same flow path as in Chapter 3 but used a Hastelloy C276 coil of approximately 3.2 mL internal volume, with the premixed compound and NaOH delivered by a single pump rather than as two separate streams. This allowed the two compounds to be compared side by side, with feed concentration and temperature range adjusted to each acid. PFBA was run at a feed concentration of 0.05 M across 150 to 250 °C at 0, 0.5, and 1 M NaOH, with the 1 M series

extended to 275 °C; PFPrA was run at a feed concentration of 0.05 M at 0, 0.35, and 0.7 M NaOH, corresponding to acid-to-NaOH ratios of 1:7 and 1:14, across 150 to 250 °C, with the 0.7 M series extended to 300 °C. A separate dilute series at 0.01 M PFPrA in 0.7 M NaOH, a 1:70 acid-to-NaOH ratio, was also run.

The system was held at 25 MPa, with a hot-zone residence time of approximately 10 minutes to match the TFMS runs and the pump flow rate set by mass conservation. At each condition the reactor was flushed with at least five hot-zone volumes before sampling, to reach steady state. To probe the degradation intermediates, both acids were also run at 0.05 M in 0.1 M NaOH at 250 °C. This sub-stoichiometric NaOH loading stalls the cascade so that intermediates accumulate rather than being driven to completion. The gas-phase products of this condition are reported in Appendix E.

Parent-compound destruction was quantified by LC-MS/MS. Native PFBA was quantified by isotope dilution against $^{13}C_4$-PFBA (from the MPFAC-MXA mixture, Wellington Laboratories). PFPrA, for which no mass-labeled analog was available in that mixture, was quantified against $^{13}C_4$-PFBA as a surrogate internal standard. External calibration used native standards from Wellington Laboratories, the PFAC-30PAR acid mixture for PFBA and a separate native PFPrA standard for PFPrA. Defluorination was quantified by ion chromatography with conductivity detection (IC-CD), the defluorination method of record, and the fluoride ion-selective electrode was not relied upon at elevated ionic strength because of the matrix limitations described in Chapter 3. IC-CD was used for fluoride only. Carbon balances were constructed by Raman deconvolution, which quantified residual parent, carbonate, tartronate, glycolate, bicarbonate, and formate against the calibrations of Appendix B, with carbon-13 NMR used for structural confirmation of the major intermediates. Apparent activation energies were determined from

Arrhenius fits with the lowest-temperature point excluded for consistency, uncertainties reported as the standard error of the fit. Density functional theory calculations, performed by the author with the protocol in Section 3.5, were used to quantify the elimination barriers of the fragments formed after decarboxylation.

5.3 PFBA Results

5.3.1 Destruction and Defluorination

Across the conditions studied, PFBA destruction increases with temperature and is independent of NaOH concentration. The carbon balance in Figure 5.7 and the kinetics in Figure 5.9 together show that parent PFBA is consumed and converted to oxygenated products, and the near-complete conversion of parent carbon at the higher temperatures under 1 M NaOH distinguishes PFBA from the shorter PFPrA examined in Section 5.4.

Destruction and defluorination were measured independently. Figure 5.1 presents parent loss by LC-MS/MS alongside fluoride release by ion chromatography at 0, 0.5, and 1 M NaOH, both referenced to the prepared feed concentration. DRE > 99.9% for T>225 °C at every hydroxide concentration was observed, including the alkali-free case, establishing that thermal scission proceeds without added base. Defluorination remains at background without hydroxide and rises steeply with alkali addition, reaching ~ 97- 98% at T ~ 225 - 250 °C.

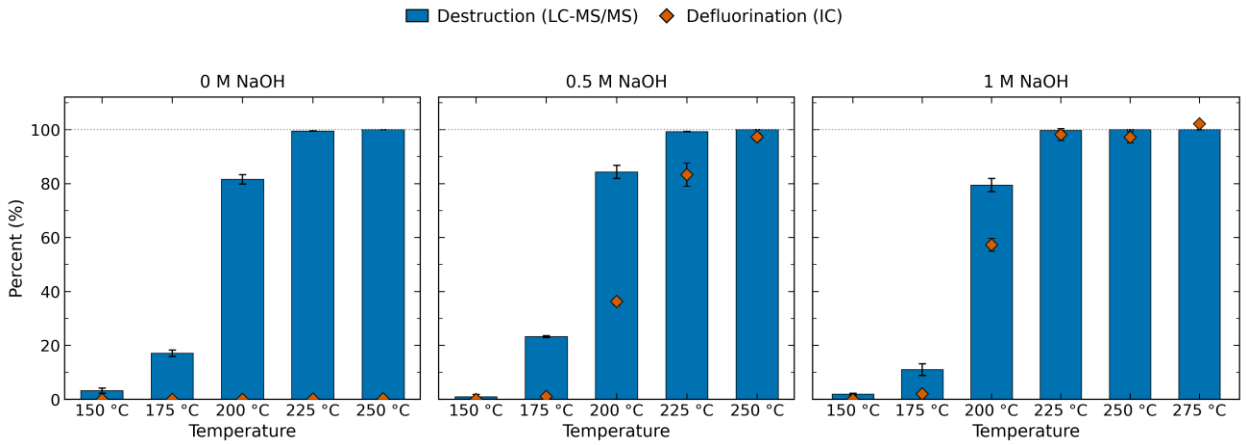

Figure 5.1: PFBA destruction (bars, LC-MS/MS) and defluorination (markers, ion chromatography) at 0, 0.5, and 1 M NaOH, T~150 - 275 °C, referenced to a prepared feed concentration of 0.05 M. Defluorination error bars are the half-range of two independent IC batches. Destruction exceeds 99.9% at every hydroxide concentration including 0 M, whereas defluorination remains at background without base.

The fate of the fluorine in the absence of base is resolved by fluorine-19 NMR. Figure 5.2 compares the feedstock with effluent treated at 200 and 250 °C, 0 M NaOH on a common gain-corrected intensity scale: the parent resonances collapse with temperature, no fluoride resonance appears at any condition, and the 250 °C spectrum shows no fluorinated species between 0 and -200 ppm. Neither fluoride nor any dissolved organofluorine species were found in the liquid within the observed window, so essentially none of the fluorine delivered in the feed is retained there in any form. Since the parent compound is fully destroyed under these conditions, the whole fluorine inventory leaves as volatile organofluorine, consistent with the fragment detected by GC-MS (Figure 5.3).

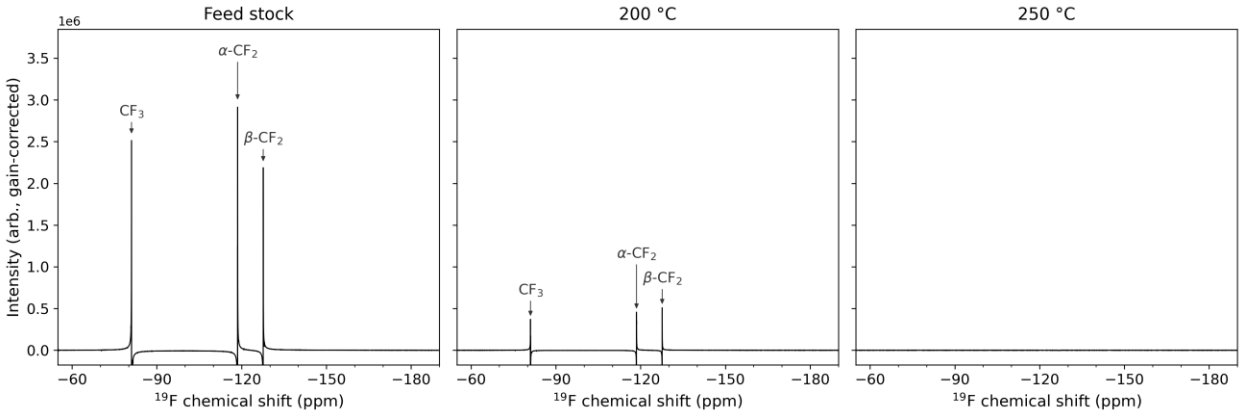

Figure 5.2: Fluorine-19 NMR spectra of PFBA feed stock and effluent treated at 200 and 250 °C at 0 M NaOH. Panels share a common gain-corrected intensity scale. Parent resonances are labeled CF_3 (-81.0 ppm), α-CF_2 (-118.6 ppm), and β-CF_2 (-127.6 ppm). No fluoride resonance appears at any condition, and no fluorinated species are detected between 0 and -200 ppm at 250 °C.

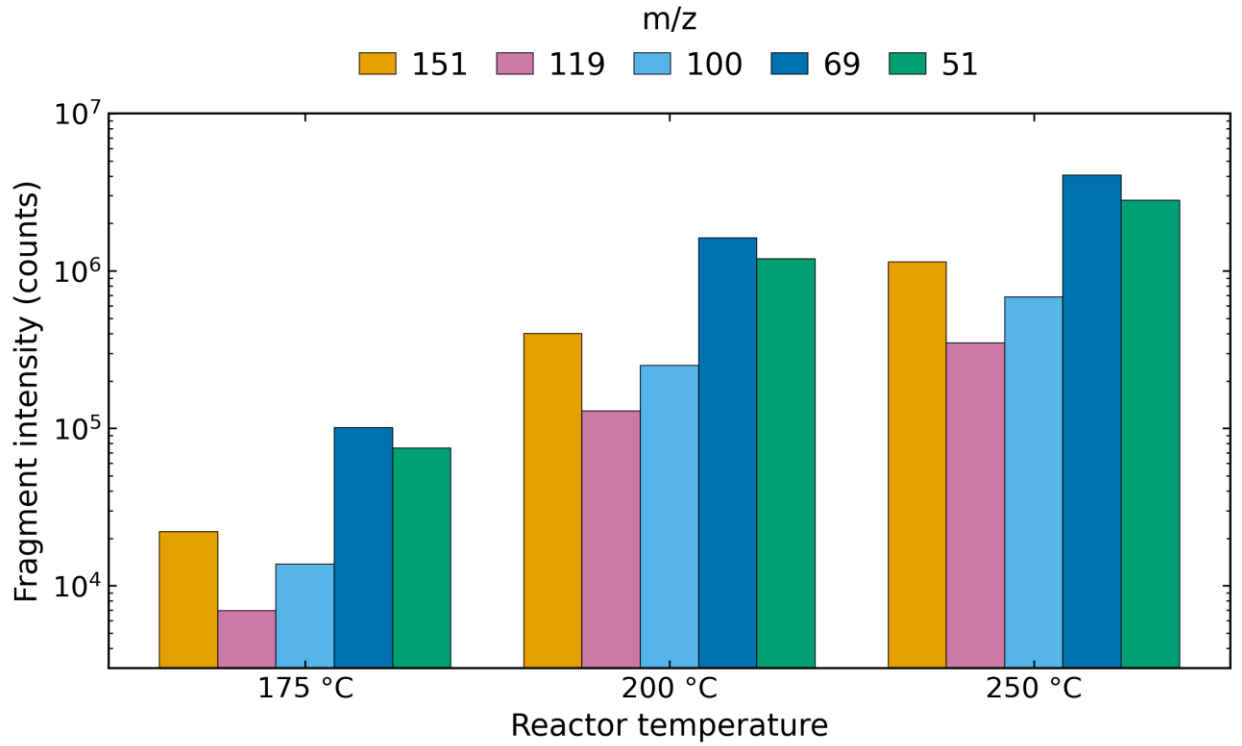

Figure 5.3: Gas-phase GC-MS of the alkali-free PFBA series (0.05 M PFBA, 0 M NaOH), showing the five fragment ions of the three-carbon hydrofluorocarbon C_3F_7H as a function of reactor temperature on a logarithmic scale. The ion at m/z 151 corresponds to loss of fluorine from the molecular ion, m/z 119 to the pentafluoroethyl cation, and m/z 69 and 51 to the trifluoromethyl and difluoromethyl cations. Relative intensities are constant across the series, confirming the presence of a single compound. No signal was detected at 150 °C. The 225 °C sample is excluded because the gas sample was lost.

Fluorine-19 NMR provides direct qualitative confirmation of this progression. Figure 5.4 shows the fluorine-19 spectra at 0.5 and 1 M NaOH across 200 to 250 °C. At the lowest temperature the

three fluorine environments of the parent acid are present, the trifluoromethyl resonance near -81 ppm and the two difluoromethylene resonances near -118 and -128 ppm, together with a small fluoride resonance near -120 ppm. As temperature increases the parent resonances disappear and the fluoride resonance dominates the spectrum, and by 225 °C no parent signal remains at either hydroxide concentration. The two NaOH concentrations behave alike, consistent with the absence of a clear hydroxide dependence in the kinetics reported in Section 5.3.3.

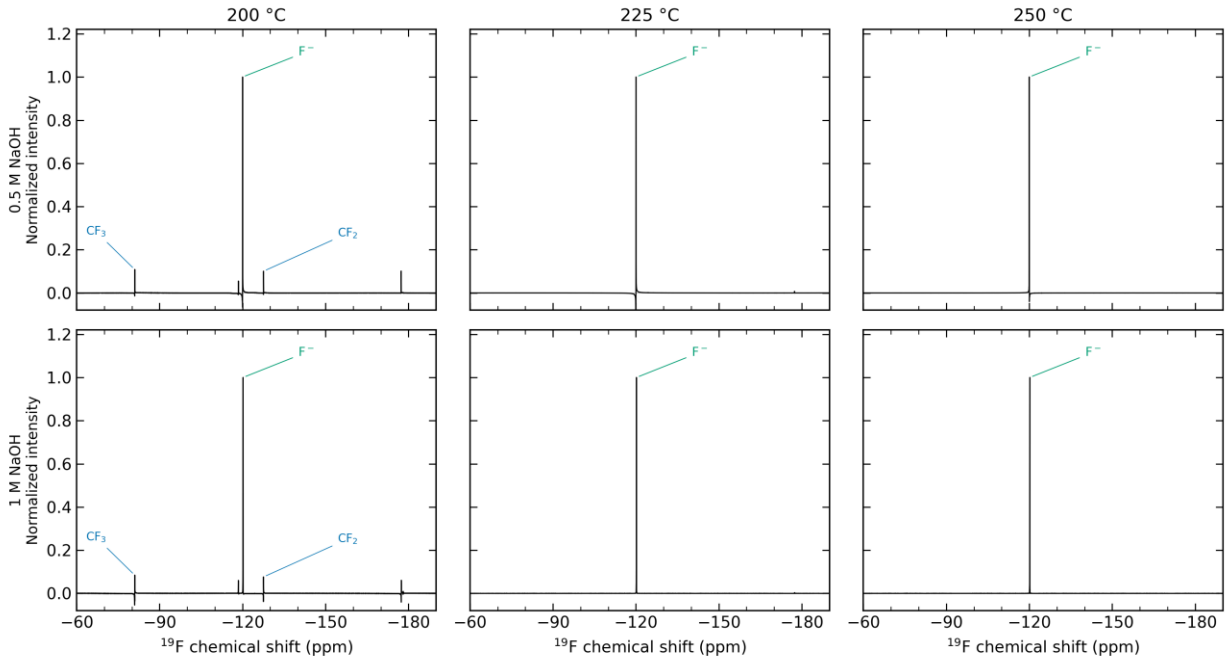

Figure 5.4: Fluorine-19 NMR spectra of PFBA effluent at 0.5 M NaOH (top row) and 1 M NaOH (bottom row) at 200, 225, and 250 °C. Each panel is normalized to its own maximum. Parent resonances are labeled CF_3 and CF_2; the fluoride resonance is labeled F-. Spectra are phase- and baseline-corrected.

Defluorination approaches completion at the higher temperatures. The narrowing of the gap between destruction and defluorination as conditions intensify indicates that the fluorinated intermediates formed after decarboxylation are efficiently converted to fluoride rather than leaving the reactor unreacted.

5.3.2 Product Identification and Carbon Balance

Carbon-13 NMR identifies the organic products directly and resolves the tartronate backbone: the carboxylate resonance at 177 ppm and the methine resonance at 75 ppm establish that the three-carbon skeleton survives intact, with carbonate at 168 ppm. A weak feature near 180 ppm is present but could not be assigned. Glycolate was resolved by Raman at 0.5 M NaOH and 250 °C, the only condition at which it was observed, and enters the product slate on that basis.

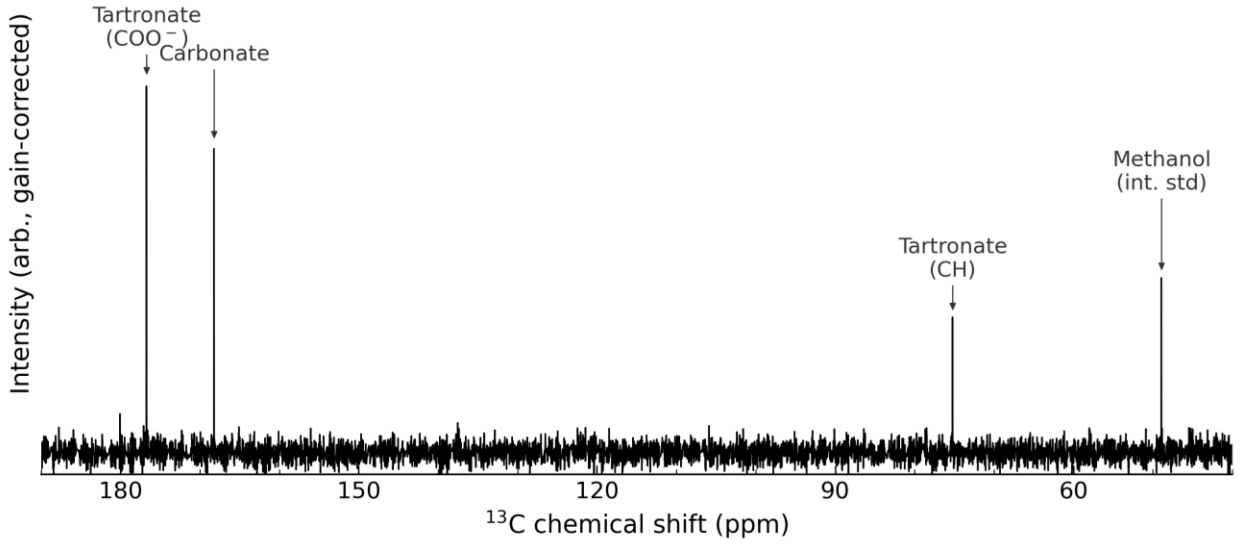

Figure 5.5: Carbon-13 NMR of PFBA treated at 275 °C in 1 M NaOH, receiver-gain corrected and wavelet denoised. Tartronate is identified by resonances at 177 ppm (carboxylate) and 75 ppm (methine), carbonate at 168 ppm, and methanol at 49 ppm as the internal standard.

The RAMAN analysis can be used to provide insight into the parent species transformation.[78, 88-90] Figure 5.6 shows that the PFBS band at 1404 cm^{-1} decreases with temperature. Tartronate is identified by its bands at 940 and 1437 cm^{-1}, and carbonate at 1066 cm^{-1}. Concentration of both products increase with temperature. The 1354 cm^{-1} feature overlaps a parent contribution and is labeled as such.

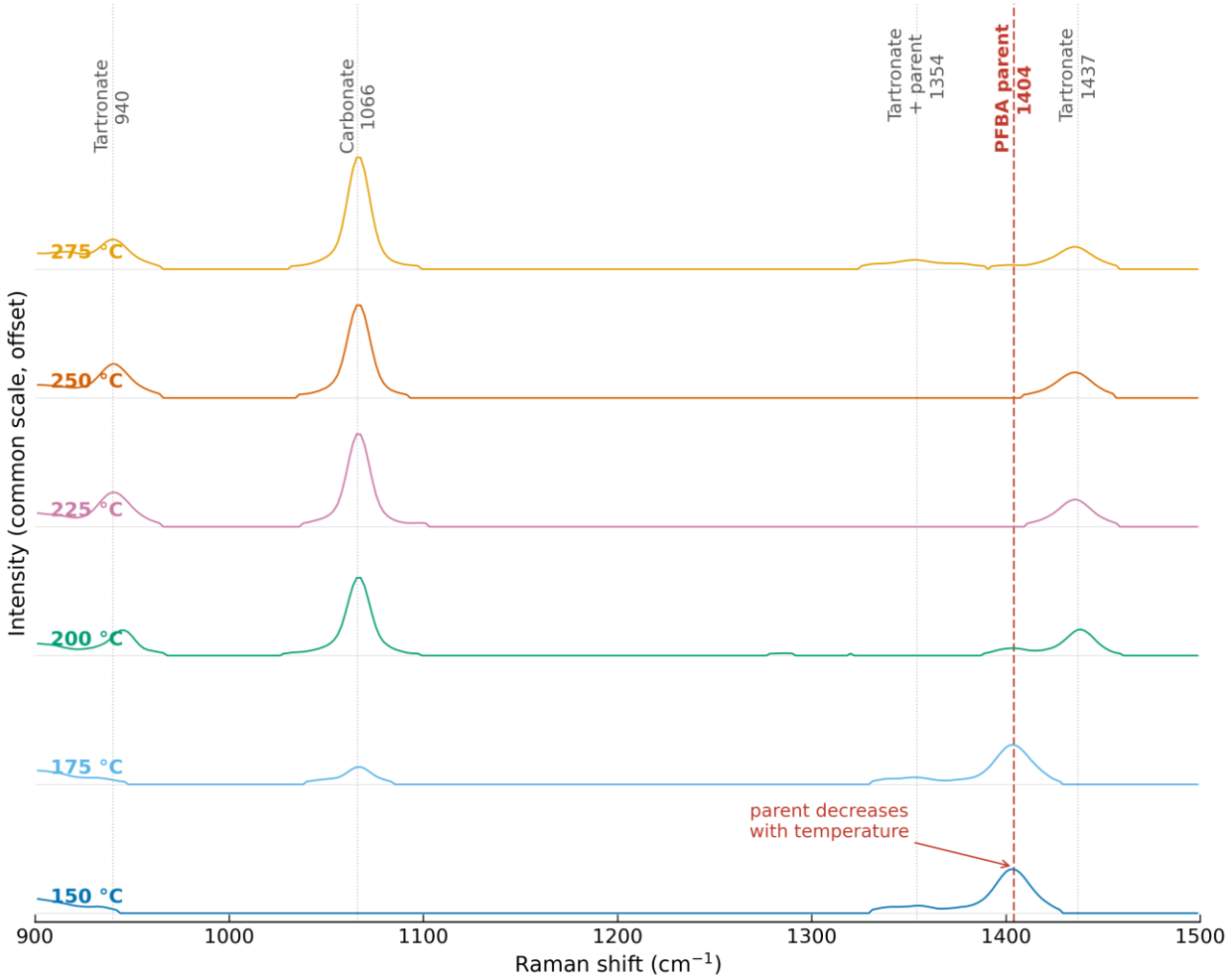

Figure 5.6: Raman spectra of PFBA products by temperature (0.05 M PFBA in 1 M NaOH). The parent band at 1404 cm^{-1} decreases while tartronate (940 and 1437 cm^{-1}) and carbonate (1066 cm^{-1}) grow in. The 1354 cm^{-1} feature overlaps a parent contribution and is labeled as such.

The carbon-containing products of PFBA degradation were identified and quantified as a function of temperature and hydroxide concentration. Figure 5.7 presents the carbon balance at 0.5 and 1 M NaOH, for T~150 - 275 °C range.

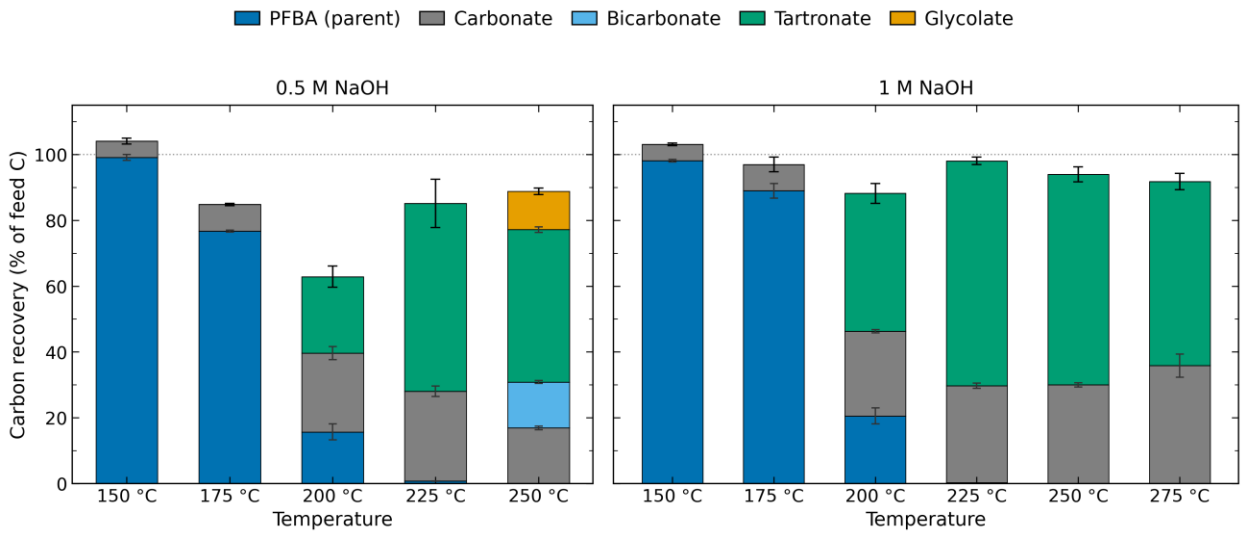

Figure 5.7: Carbon balance for PFBA degradation at 0.5 and 1 M NaOH across 150 to 275 °C, with the 1 M series extended to 275 °C, expressed as % of feed carbon. Parent is from LC-MS/MS; carbonate, bicarbonate, glycolate, and tartronate are from Raman deconvolution against the calibrations of Appendix B. Error bars are the half-range of duplicate spectra where available. The gap below 100% at high temperature includes the volatile fragment C_3F_7H detected in the gas phase but not quantified.

At low temperature, the carbon persists predominantly as parent PFBA, and as temperature rises, the parent is converted to carbonate, to bicarbonate at the lower NaOH loading, and to the two- and three-carbon hydroxy-acids glycolate and tartronate, with tartronate becoming the dominant product above 200 °C. Carbon recovery slightly exceeds 100% at 150 °C in both series, where the PFBA is essentially unconverted. This reflects carbonate carried into the reactor by the alkaline stock, which takes up atmospheric carbon dioxide during handling, and appears as a fixed positive offset at a given NaOH loading. Bicarbonate appears only at 250 °C in the 0.5 M series, where NaOH has been consumed, and the carbonate-bicarbonate equilibrium shifts before conversion to carbonate is complete. At higher temperature, recovery falls below 100%, reaching 89% at 250 °C in the 0.5 M series and 92% at 275 °C in the 1 M series, consistent with the volatile fragment leaving the effluent levels unquantified. Glycolate is resolved only at 250 °C in the 0.5 M series and is present as a minor intermediate rather than a general product. The detection of the volatile three-carbon fragment C_3F_7H in the gas phase confirms that a fraction of the decarboxylated

fragment leaves unreacted before it is defluorinated, though for PFBA this loss is minor relative to the carbon retained and defluorinated. The identity of the hydroxy-acid intermediates was confirmed by carbon-13 NMR, shown in Figure 5.5. Tartronate was identified by resonances at 177 ppm (carboxylate) and 75 ppm (methine), and carbonate at 168 ppm.

The gas phase provides independent evidence for the PFBA thermal degradation. Figure 5.3 shows the diagnostic fragment ions of the released species for the alkali-free PFBA series across temperature. The peak eluting near 13 to 14 minutes is assigned to C_3F_7H from its electron-ionization fragmentation, which shows m/z 151 corresponding to loss of fluorine from the molecular ion, m/z 119 for the pentafluoroethyl cation, m/z 69 for the trifluoromethyl cation, and m/z 51 for the difluoromethyl cation. All five diagnostic ions appear together and grow with reactor temperature, with no signal at 150 °C. Because decarboxylation generates the perfluoropropyl fragment and protonation of that fragment yields C_3F_7H, the growth of this signal with temperature tracks the increasing decarboxylation and confirms that the hydrofluorocarbon branch operates in this system.

The experiment under alkaline conditions isolates the role of hydroxide. Figure 5.8 compares the C_3F_7H fragment ions at 0 and 1 M NaOH at two temperatures. At 200 °C, the two alkali amendment levels are indistinguishable. At 250 °C, all five ions in GC/MS are suppressed by more than two orders of magnitude. The fragment remains detectable under alkali at these suppressed levels, so a minor fraction is still released. NaOH suppresses release of the three-carbon fragment only where the elimination is fast relative to the residence time. This is the behavior expected for a base-assisted activation barrier of 22.4 kcal/mol.

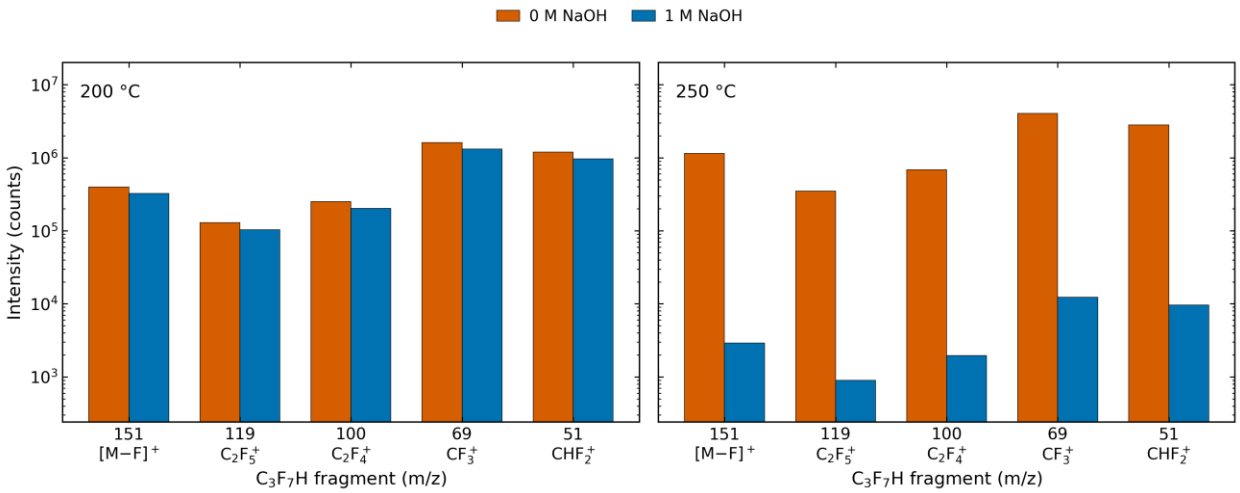

Figure 5.8: Gas-phase GC-MS of PFBA at 0 M and 1 M NaOH, comparing the five C_3F_7H fragment ions at 200 °C and 250 °C on a shared logarithmic scale. All five ions are suppressed by more than two orders of magnitude at 250 °C in the presence of hydroxide, while at 200 °C the two hydroxide levels are indistinguishable. The two datasets were acquired two weeks apart.

5.3.3 PFBA Destruction Kinetics

.The apparent activation energies are 102 ± 20 kJ/mol at 0 M, 97 ± 13 kJ/mol at 0.5 M, and 122 ± 24 kJ/mol at 1 M NaOH, a narrow range of roughly 97 to 122 kJ/mol with no clear dependence on hydroxide concentration. The absence of a strong hydroxide dependence in the destruction rate indicates that the rate-limiting step of parent-compound destruction is the decarboxylation of PFBA rather than a hydroxide-mediated step, consistent with the thermal decarboxylation behavior established for PFCAs.

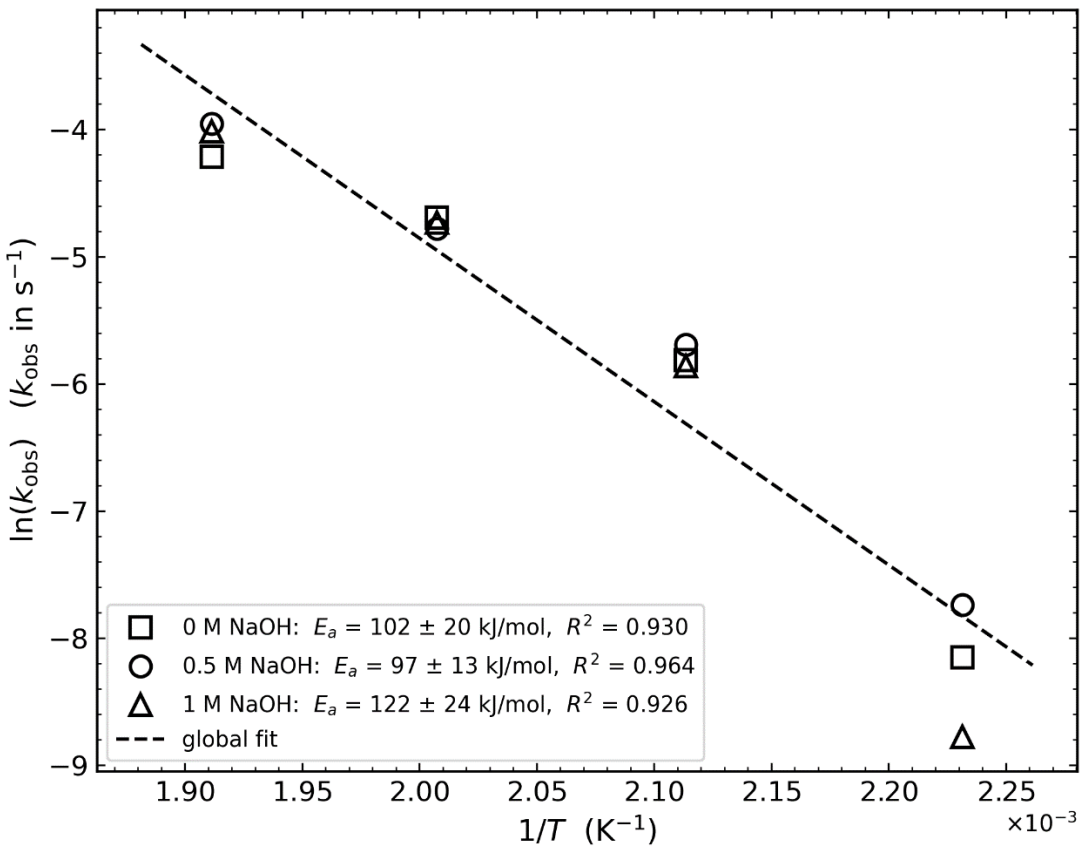

Figure 5.9: Arrhenius analysis of PFBA destruction at 0 M (squares), 0.5 M (circles), and 1 M NaOH (triangles). Apparent activation energies are 102 ± 20, 97 ± 13, and 122 ± 24 kJ/mol, respectively. The dashed line represents the global fit.

5.4 PFPrA Results

5.4.1 Destruction and Defluorination

Destruction and defluorination were measured independently. Figure 5.10 compares parent compound loss by LC-MS/MS and fluoride release by IC in the 0 - 0.7 M NaOH range. Destruction approaches completion at T~ 225 - 250 °C for every concentration, including the alkali-free case, which establishes that scission of the parent proceeds thermally and does not require added base. Defluorination remains near zero at 0 M NaOH for all temperatures, and rises with hydroxide concentration, reaching approximately 17% at 0.35 M and 41% at 0.7 M at 250 °C. The separation between the destruction bars and the defluorination markers in the alkali-free panel

shows the two-step behavior: (i) the carbon skeleton is broken thermally; (ii) fluoride is released by hydroxide attacking the intermediate organic fluorine compound from PFPrA degradation.

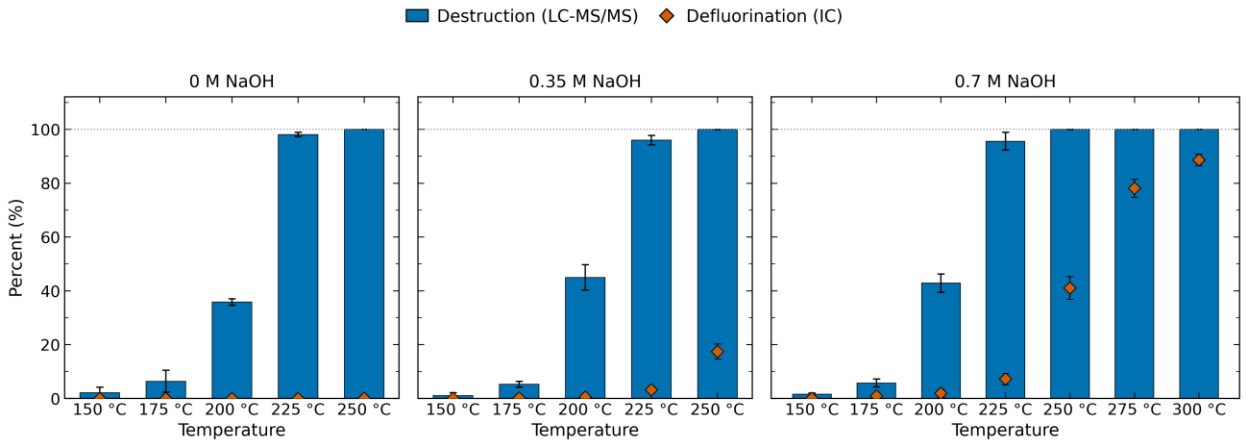

Figure 5.10: PFPrA destruction (bars, LC-MS/MS) and defluorination (markers, ion chromatography) at 0, 0.35, and 0.7 M NaOH across 150 to 300 °C at a feed concentration of 0.05 M. Destruction error bars are from duplicate LC-MS/MS measurements. Destruction reaches near-completion at every hydroxide concentration including 0 M, whereas defluorination remains near zero without base.

PFPrA was run in the same reactor and under the same single-phase alkaline conditions used for PFBA, so that the two acids could be compared on the same basis. The parent compound behaves much as PFBA: destruction increases with temperature and approaches completion at the upper end of the range. Defluorination is significantly different. At 250 °C, where PFBA was fully converted to fluoride, PFPrA reaches only 41% defluorination. The carbon balance shows carbonate rising toward a ceiling near one-third of the feed carbon rather than closing. The difference in defluorination therefore does not lie in the rate of destroying the parent PFAS, but rather in the fate of the product of incomplete destruction (PID) from decarboxylation. The two-carbon fragment (C_2F_5H) was detected in the gas phase under every condition tested, and unlike the three-carbon fragment released in PFBA decomposition, it was not mineralized rapidly. In the PFPrA case, defluorination occurred at T > 225 °C, reaching 41% at 250 °C, 78% at 275 °C, and 89% at 300 °C at the same NaOH loading. The difference from PFBA is therefore an onset temperature > 50 °C rather than an absolute limit on defluorination. This delay in defluorination

rate is an important experimental observation; the mechanistic analysis is presented in Section 5.5. To elucidate this behavior, the elimination barriers were computed by density functional theory.

Fluorine-19 NMR of the 0 M series shows the fate of fluorine in effluent. Figure 5.11 compares the PFPrA feedstock with effluent treated at 200 and 250 °C and 0 M NaOH: the parent resonance peaks disappear, while no fluoride resonances are present, and the 250 °C spectrum shows no fluorinated species between 0 and -200 ppm. As with PFBA, the organofluoride does not mineralize; it is not released as fluoride nor as a dissolved fluorinated intermediate. Under these conditions, the entire fluorine inventory must leave as VOF.

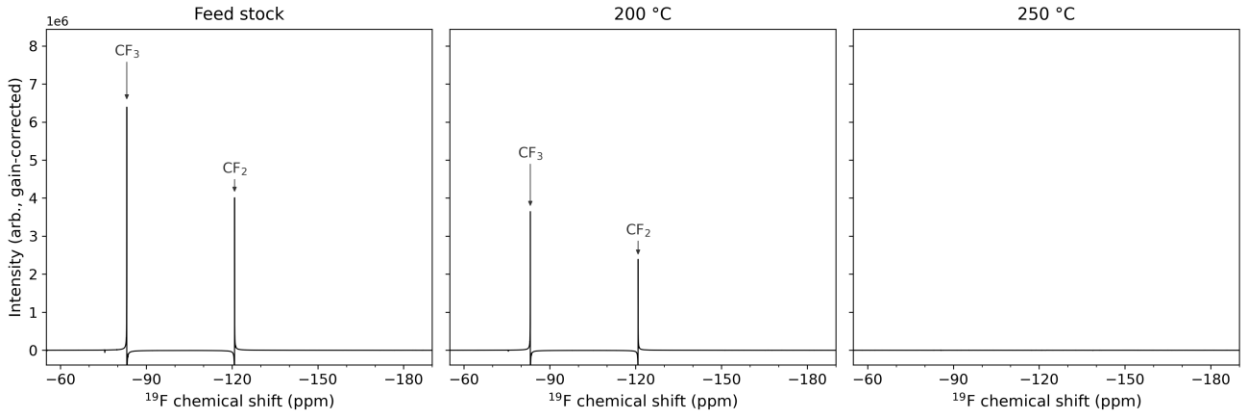

Figure 5.11: Fluorine-19 NMR spectra of PFPrA feed stock and effluent treated at 200 and 250 °C at 0 M NaOH. Panels share a common gain-corrected intensity scale. Parent resonances are labeled CF_3 (-83.2 ppm) and CF_2 (-120.9 ppm). No fluoride resonance appears at any condition, and no fluorinated species are detected between 0 and -200 ppm at 250 °C.

The gas phase confirms the identity of the released PID. Figure 5.12 shows the diagnostic ions of the two-carbon hydrofluorocarbon C_2F_5H in the alkali-free PFPrA decomposition as a function of temperature. The assignment uses m/z 101 for loss of fluorine from the molecular ion, m/z 119 for loss of hydrogen, and m/z 69 and 51 for the trifluoromethyl and difluoromethyl cations. The ratio of all four ions remains unchanged with temperature, indicating the presence of a single compound. Tetrafluoroethylene was not detected in this series. Its ions at m/z 81 and 100 were monitored explicitly and remained below roughly 10^{-4} of the C_2F_5H signal.

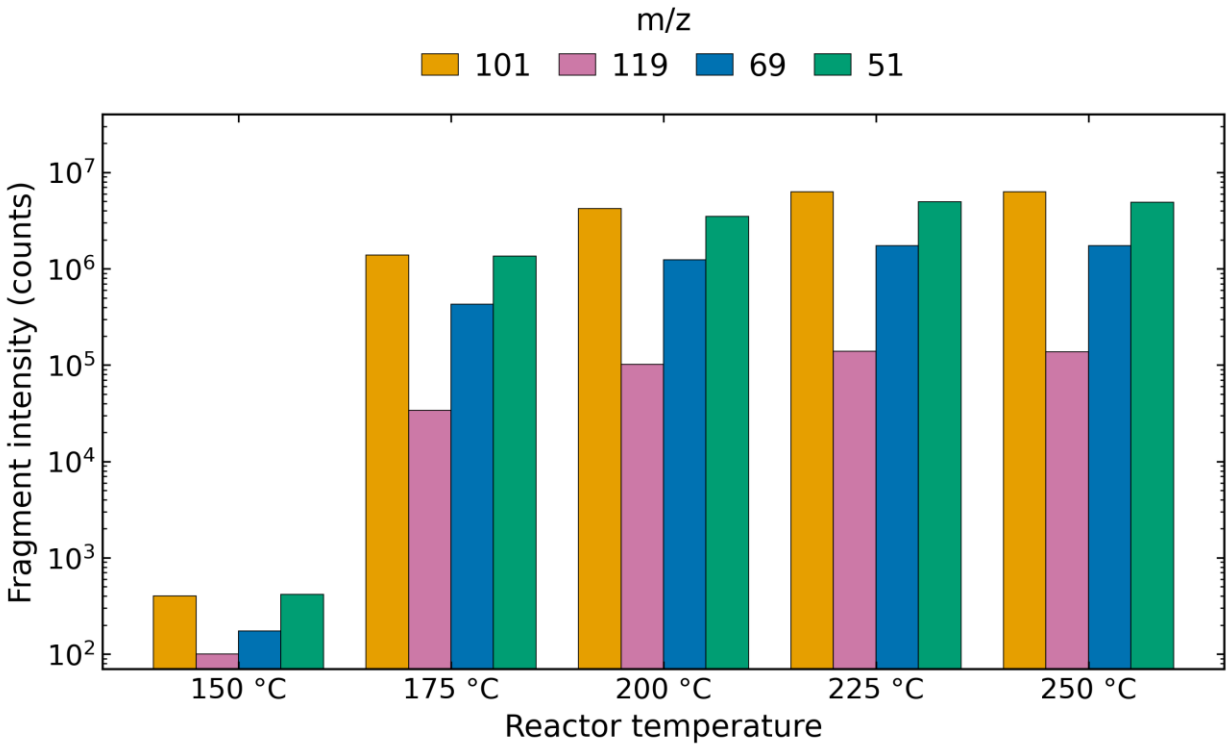

Figure 5.12: Gas-phase GC-MS of the alkali-free PFPrA series (0.05 M PFPrA, 0 M NaOH), showing the four diagnostic fragment ions of C_2F_5H as a function of reactor temperature on a logarithmic scale. The 150 °C bars lie at the plotting floor and represent non-detection.

5.4.2 Product Identification and Carbon Balance

Carbon-13 NMR identifies the organic products, including oxalates. Figure 5.13 shows the spectrum of PFPrA effluent treated at 300 °C in 0.7 M NaOH, with methanol at 49 ppm as internal standard. Two carbon products are resolved above the noise floor: oxalate near 173 ppm and carbonate near 168 ppm. The presence of oxalate establishes that a fraction of the PFPrA carbon is retained as a two-carbon diacid rather than being mineralized completely. Note that oxalates are challenging to resolve by Raman spectroscopy due to their low scattering cross-section. No organofluorine resonances were found within the observed window.

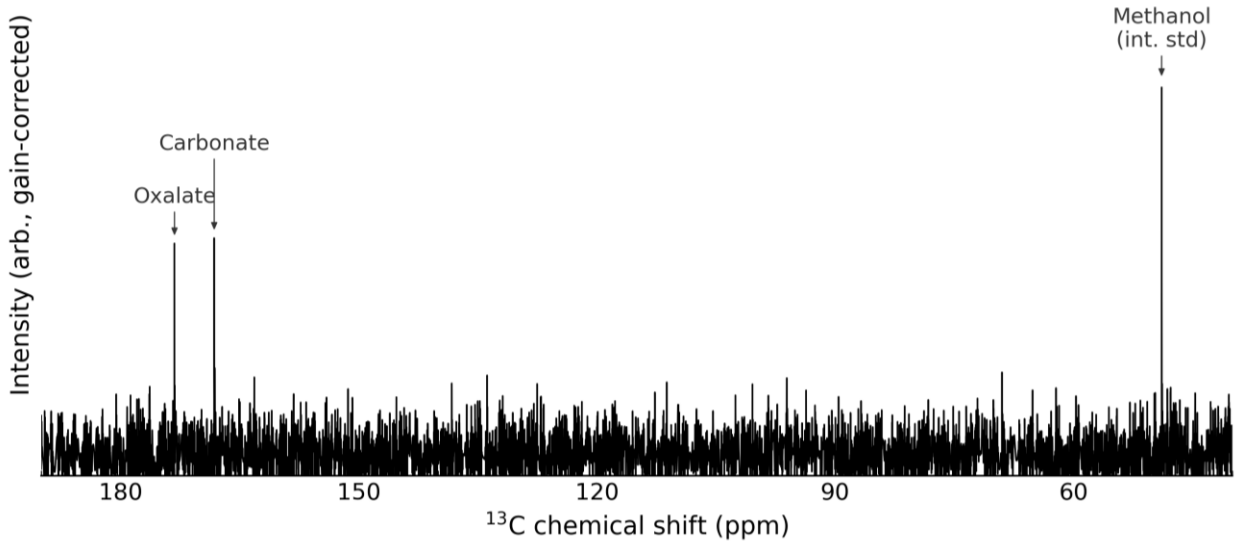

Figure 5.13: Carbon-13 NMR of PFPrA effluent treated at 300 °C in 0.7 M NaOH. Oxalate appears near 173 ppm and carbonate near 168 ppm; methanol at 49 ppm is the internal standard. The spectrum is receiver-gain corrected and wavelet denoised. Only peaks resolved above the noise floor are labeled.

The Raman spectra underlying the quantification are shown in Figure 5.14: the parent band at 1410 cm^{-1} decreases across temperature while carbonate at 1066 cm^{-1} and formate at 1352 cm^{-1} grow in, and the formate assignment is confirmed by deconvolution against a sodium formate standard.

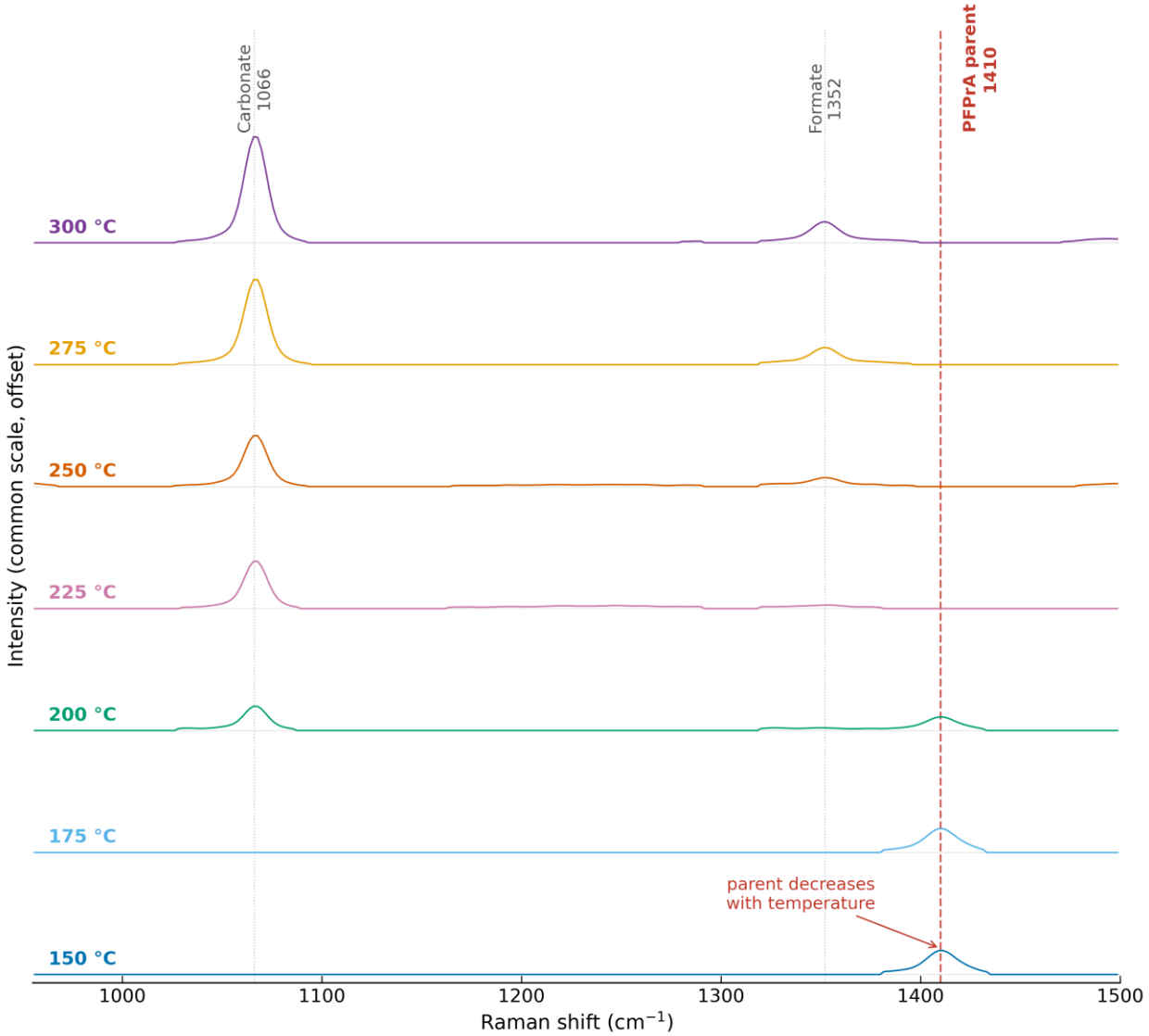

Figure 5.14: Raman spectra of PFPrA products by temperature (0.05 M PFPrA in 0.7 M NaOH). The parent band at 1410 cm^{-1} decreases while carbonate (1066 cm^{-1}) and formate (1352 cm^{-1}) grow in.

The full carbon balance for PFPrA is shown in Figure 5.15, resolving parent PFPrA, carbonate, and the organic-acid products across temperature. At both NaOH loadings carbonate stalls near one-third of the feed carbon through 250 °C.

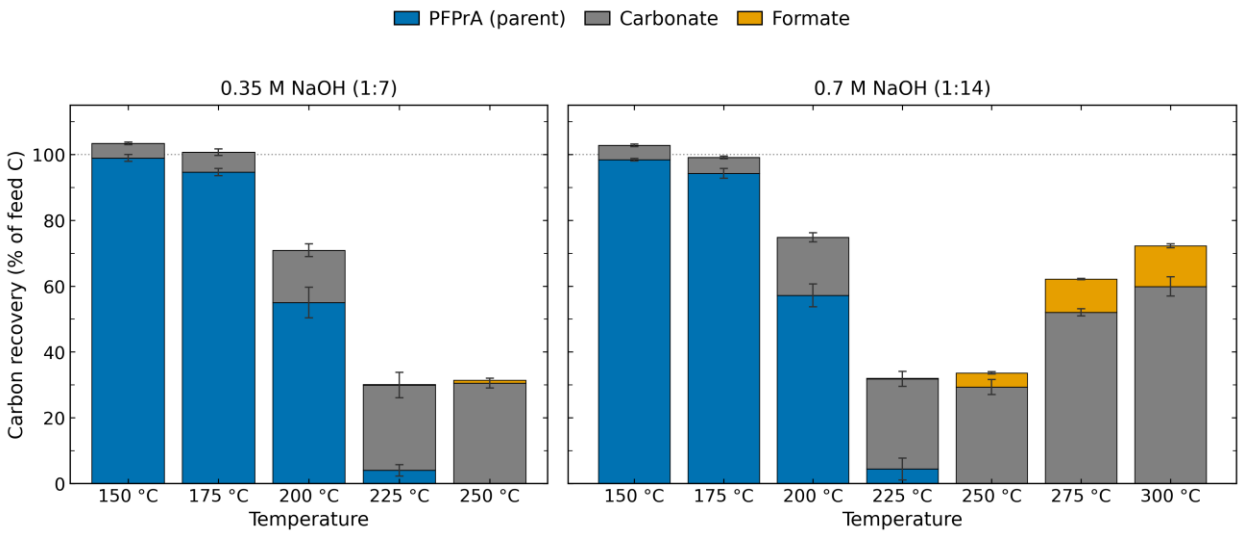

Figure 5.15: Carbon balance for PFPrA degradation at 0.35 M (1:7) and 0.7 M (1:14) NaOH as a function of temperature, expressed as % of feed carbon. Parent is from LC-MS/MS; carbonate and formate are from Raman. Carbonate is near one-third of the feed carbon through 250 °C in both series and rises above that level in the 0.7 M series at 275 and 300 °C, reaching 60% at 300 °C. The gap below 100% is carbon leaving as C_2F_5H gas. Oxalate is identified separately by carbon-13 NMR in Figure 5.13.

The near-stoichiometric series (1x stoichiometric) was run first, at 1:7, the stoichiometric requirement calculated on complete bond scission, and at 1:14, twice that requirement. The corresponding PFPrA defluorination was 17% and 41% at 250 °C, where the PFBA yielded deF% > 96% for the same stoichiometry. To further explore the effect of the NaOH-to-acid ratio, the alkali concentration was kept at 0.7 M NaOH, but the PFPrA concentration was reduced to 0.01 M, yielding an inlet molar PFPrA/NaOH concentration of 1:70, ten times the stoichiometric requirement. Figure 5.16 compares the 1:14 series (2x stoichiometric) to the 1:70 series (10x stoichiometric); the temperature series shows carbon balance and defluorination.

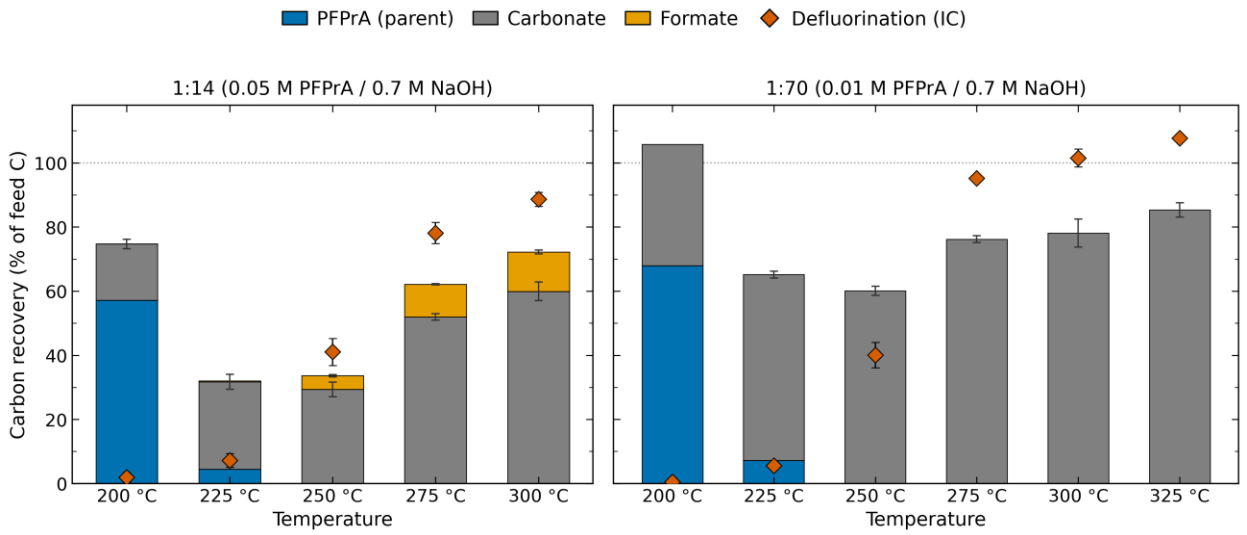

Figure 5.16: Carbon balance and defluorination for the 1:14 and 1:70 PFPrA-to-NaOH series. Bars show parent, carbonate, and formate; markers show defluorination measured by ion chromatography. The 1:14 series covers 200 to 300 °C and the 1:70 series 200 to 325 °C. The 1:70 defluorination reads slightly above 100% at 300 and 325 °C, within the uncertainty of the measurement. C_2F_5H was detected by GC-MS in all series.

At 0.05 M PFPrA in 0.35 and 0.7 M NaOH (1:7 and 1:14), the temperature series show that carbon mineralization is limited to ~30% at T~225-250 °C. Note that under the same stoichiometric conditions, PFBA defluorinated almost completely. Raising the relative NaOH loading or the temperature led to more complete mineralization. Reducing the PFPrA/NaOH ratio to 1:70, ten times the stoichiometric requirement, raises carbon conversion to 60% at 250 °C and to 85% at 325 °C, the highest measured in any series. The plateau of 1/3 carbon conversion is likely to have a mechanistic interpretation. Of the three carbons in PFPrA, the carboxyl carbon (COOH) is cleaved first and released as carbon dioxide on decarboxylation and captured as carbonate in the presence of hydroxide, while the remaining two carbons remain unreacted as C_2F_5H. Raising the temperature enables a different route, since the 1:14 temperature series yields >1/3 C conversion above 250 °C. Carbon conversion increases with both NaOH loading and temperature. Decarboxylation is independent of NaOH, so the dependence lies in the fate of the fragment, not in destruction of the parent. Higher NaOH and higher temperature both speed up that reaction, so more of the fragment is consumed before the effluent leaves the reactor. For the tested residence

time, in every series, at every NaOH-to-acid ratio, C_2F_5H was detected by GC-MS, so the unreacted fraction persists even at the highest base loading tested.

The gas-phase emissions analysis provides a counterpart to the effluent carbon balance. Figure 5.17 shows the four diagnostic fragment ions of C_2F_5H across the same temperature range.

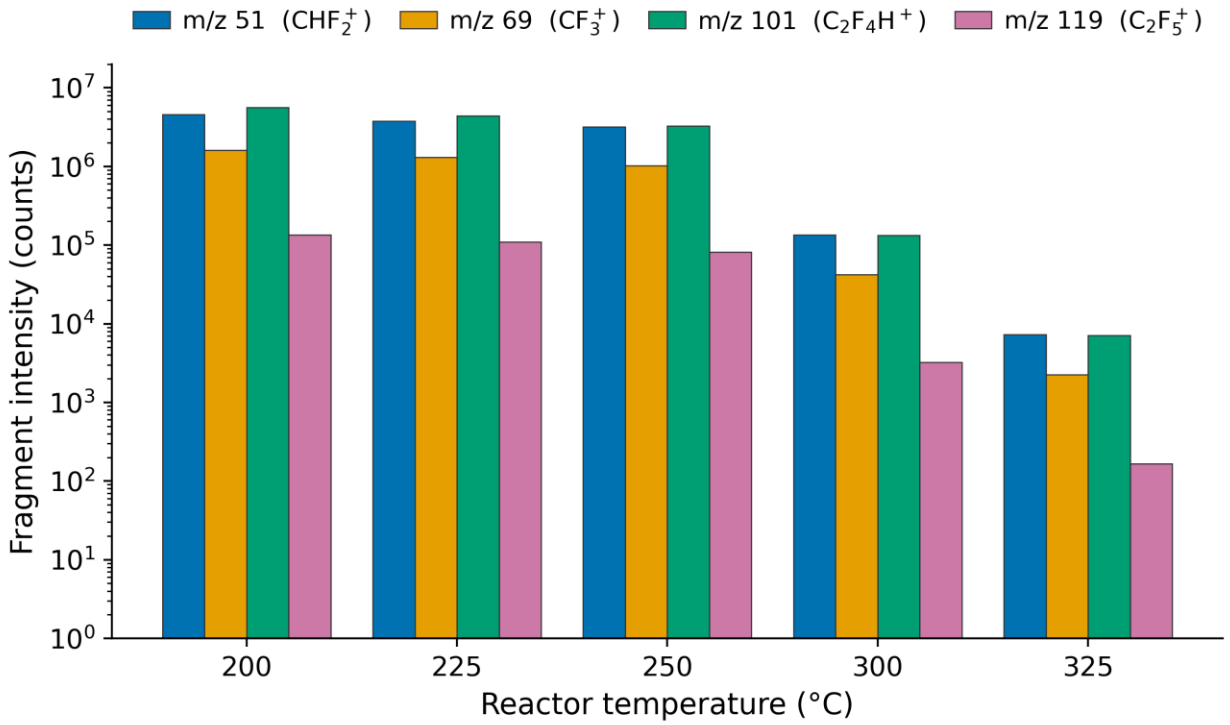

Figure 5.17: Gas-phase GC-MS of the dilute PFPrA series (0.01 M PFPrA, 0.7 M NaOH, a 1:70 ratio), showing the four diagnostic fragment ions of C_2F_5H as a function of reactor temperature on a logarithmic scale.

The peak ratios are similar for all cases, identifying that likely only a single compound is present. Concentrations in the effluent fall rapidly for T > 250 °C. Read together with the carbonate data, the effluent and gas measurements are complementary: carbon that does not appear as C_2F_5H in the gas phase appears instead as carbonate in the liquid, and both transitions occur in the same temperature range. The fate of the two-carbon fragment is therefore set by the competition between molecular-level reaction and the C_2F_5H partitioning from the liquid phase. The critical point of C_2F_5H is T= 66.05°C, P= 3.592 MPa. Since liquid water is highly polar and forms strong hydrogen

bonds, non-polar or weakly polar supercritical fluids behave largely immiscible. The data for these systems at high temperature and high pressure are very limited in the scientific literature and deserve additional investigations.

5.4.3 Kinetics

The apparent activation energies are 132 ± 13 kJ/mol at 0 M, 131 ± 14 kJ/mol at 0.35 M, and 129 ± 12 kJ/mol at 0.7 M NaOH, a narrow range of 129 to 132 kJ/mol with no clear hydroxide dependence. As for PFBA, the absence of a hydroxide dependence places the rate-limiting step of parent-compound destruction at decarboxylation rather than at a hydroxide-mediated step. The comparison with PFBA and with the other literature is made in Section 6.1.

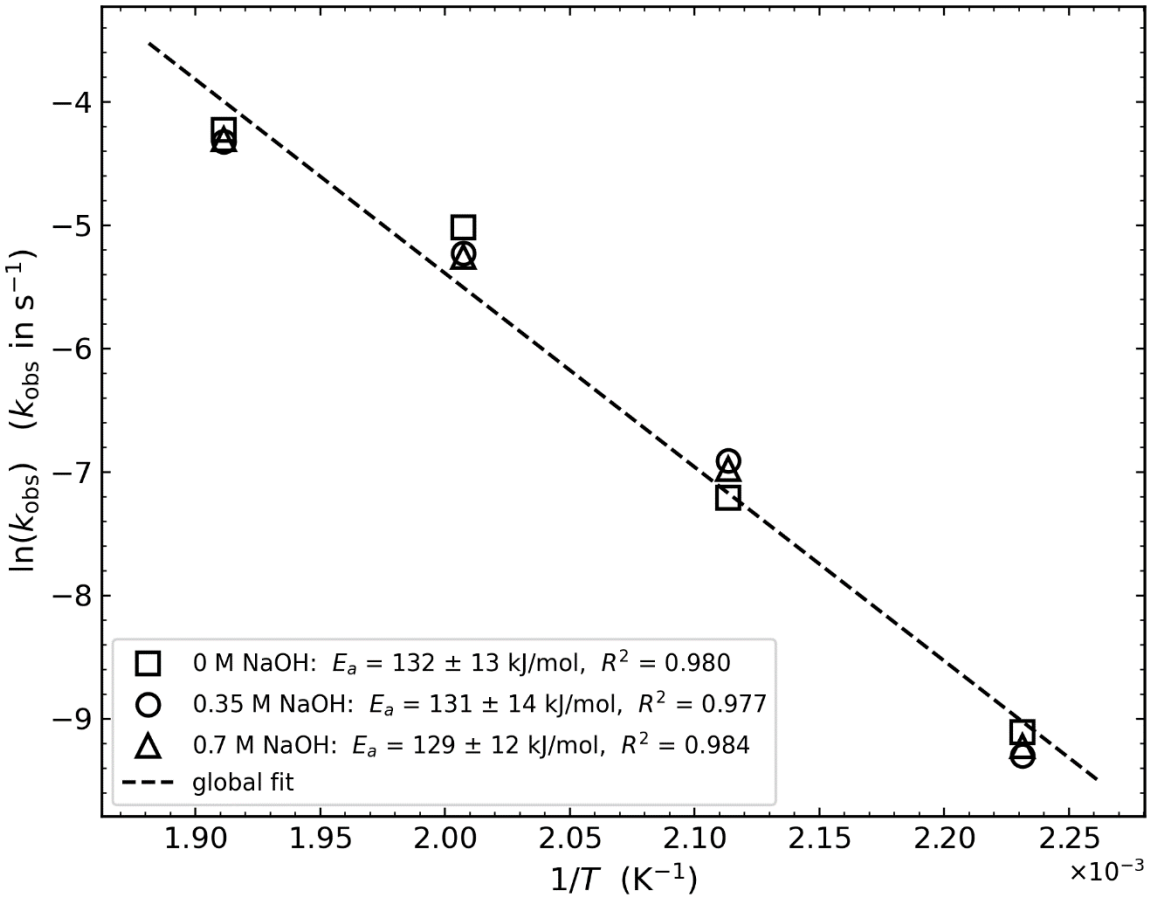

Figure 5.18: Arrhenius analysis of PFPrA destruction at 0 M (squares), 0.35 M (circles), and 0.7 M NaOH (triangles). Apparent activation energies are 132 ± 13, 131 ± 14, and 129 ± 12 kJ/mol, respectively, with no clear hydroxide dependence. The dashed line is the global fit.

5.5 Discussion

The two PFCA are destroyed at relatively mild AH conditions, as the activation energies suggest. Yet PFBA reaches 97 to 98% defluorination at 250 °C, whereas PFPrA reaches ~41%. The difference therefore arises from the behavior of PIDs.

To gain insight into the defluorination trends, base-mediated defluorination chemistry of the fragments that form after decarboxylation was performed using density functional theory; the computational protocol is described in Section 3.5. The calculations quantify the elimination barriers of these fragments and provide a mechanistic explanation for the observed chain-length dependence. The density functional theory analysis of the fragment elimination barriers is

presented first, followed by the comparison of reaction rate against residence time that unifies the two compounds, and finally a proposed step-by-step mechanism consistent with the observed products.

5.5.1 Elimination Barriers of the C_2 and C_3 Fragments

As an initial step in PFCA destruction, decarboxylation removes the carboxyl group of each parent acid as carbon dioxide and produces a perfluoroalkyl species one carbon shorter than the parent compound. PFPrA, a three-carbon acid, yields a two-carbon fragment -- pentafluoroethane (CHF_2CF_3)- and PFBA, a four-carbon acid, yields a three-carbon fragment corresponding to 1H-perfluoropropane (C_3HF_7), referred to here as the C_2 and C_3 fragments. The defluorination of each fragment proceeds by elimination of hydrogen fluoride across adjacent carbon atoms to form the corresponding perfluoroalkene, tetrafluoroethylene for the C_2 fragment and perfluoropropene for the C_3 fragment.

The computed activation free energies are presented in Table 5.1. In the base-assisted (neutral) model, the C_2 fragment has a barrier of 29.9 kcal/mol and the C_3 fragment a barrier of 22.4 kcal/mol, a difference of 7.5 kcal/mol. In the carbanion model, the C_2 fragment has a barrier of 16.8 kcal/mol and the C_3 fragment a barrier of 10.1 kcal/mol, a difference of 6.7 kcal/mol, again with the C_2 fragment having a higher value. This consistency for both independent reaction models indicates a greater stability of the C_2 fragment. Figure 5.19 presents the two profiles. Computed Gibbs free energy profiles for base-mediated fluoride elimination. Left, base-assisted elimination from the neutral 1H-fluoroalkane with hydroxide as the base: CHF_2CF_3 to $CF_2{=}CF_2$ (C2, from PFPrA), C_3HF_7 to $CF_3CF{=}CF_2$ (C3, from PFBA), and CF_3CH_2F to $CHF{=}CF_2$ (R-134a). Right, beta-fluoride elimination from the perfluoroalkyl carbanion: $C_2F_5^-$ to $CF_2{=}CF_2$ and $C_3F_7^-$ to $CF_3CF{=}CF_2$. Brackets give the difference in activation free energy between the C2 and C3

transition states. Product levels in the left panel are schematic; those in the right panel are computed. All values are in kcal/mol at 298.15 K, obtained at the ωB97X-D3/ma-def2-TZVP level with the SMD implicit solvent model for water. R-134a undergoes direct dehydrofluorination without a carbanion intermediate and appears only in the left panel.

Table 5.1: Computed activation free energies (kcal/mol) at 298.15 K.

Fragment / species	Neutral (base-assisted)	Carbanion
C_2 (from PFPrA)	29.9	16.8
C_3 (from PFBA)	22.4	10.1

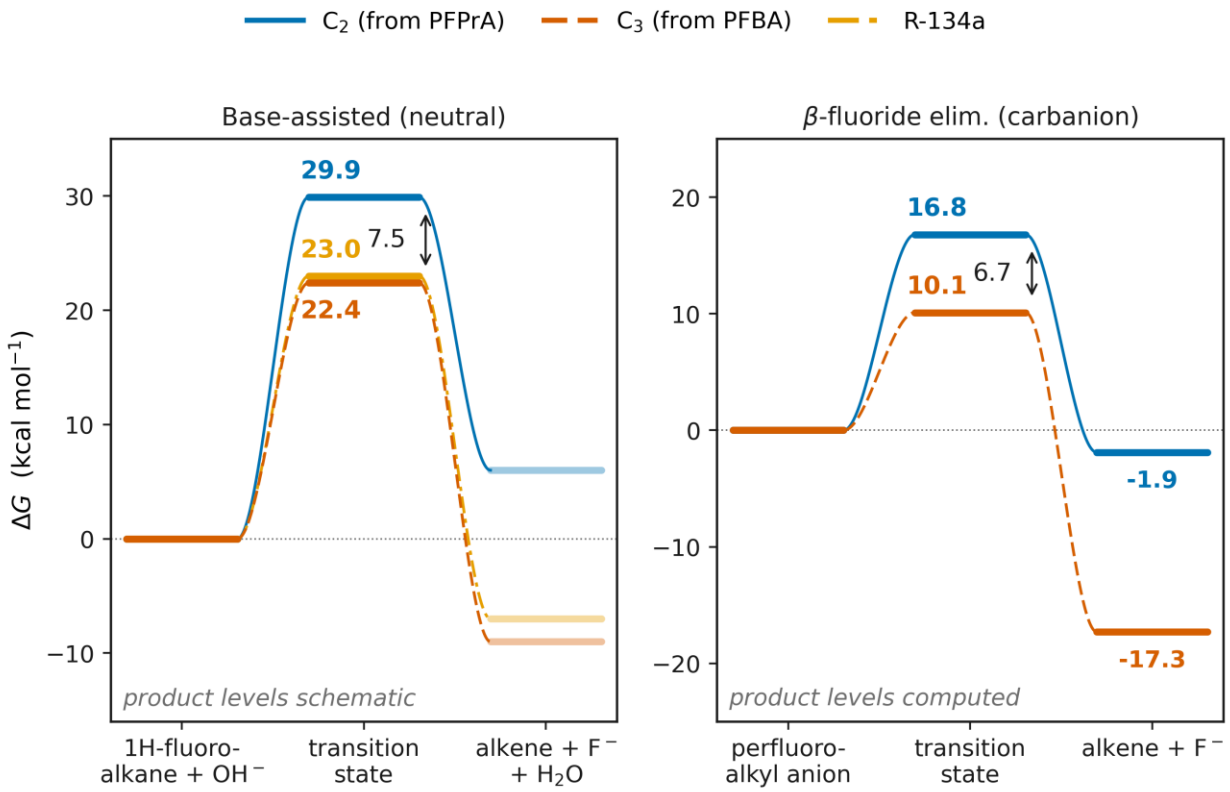

Figure 5.19: Computed Gibbs free energy profiles for base-mediated fluoride elimination. Left, base-assisted elimination from the neutral 1H-fluoroalkane with hydroxide as the base: CHF_2CF_3 to $CF_2{=}CF_2$ (C_2, from PFPrA), C_3HF_7 to $CF_3CF{=}CF_2$ (C_3, from PFBA), and CF_3CH_2F to $CHF{=}CF_2$ (R-134a). Right, beta-fluoride elimination from the perfluoroalkyl carbanion: $C_2F_5^-$ to $CF_2{=}CF_2$ and $C_3F_7^-$ to $CF_3CF{=}CF_2$. Brackets give the difference in activation free energy between the C_2 and C_3 transition states. Product levels in the left panel are schematic; those in the right panel are computed. All values are in kcal/mol at 298.15 K, obtained at the ωB97X-D3/ma-def2-TZVP level with the SMD implicit solvent model for water. R-134a undergoes direct dehydrofluorination without a carbanion intermediate and appears only in the left panel.

5.5.2 Comparison with the Literature

The computed barriers are consistent with independently reported values. The carbanion (R_3C^-) elimination of the C_2 fragment, the beta-fluoride elimination of the pentafluoroethyl anion to tetrafluoroethylene, has been examined by an independent group for conversion of the refrigerant HFC-125 to tetrafluoroethylene; that study, at a comparable level of theory, reported a barrier of 20.8 kcal/mol for this elimination. [91] The calculated value of 16.8 kcal/mol is of the same magnitude and describes the same elementary step. The difference is attributable to solvent rather than to the counterion: that study reports 20.8 kcal/mol with a potassium counterion in toluene, 22.4 kcal/mol in tetrahydrofuran, and 25.4 kcal/mol when the potassium is sequestered, so removing the counterion raises the barrier there, whereas the present calculation carries no counterion and uses an implicit water model that stabilizes the departing fluoride more strongly than a low-polarity solvent. The agreement in both the direction and the approximate magnitude of the barrier values indicates that the method produces physically reasonable results for this class of reaction.

The general behavior of the perfluoroalkyl carbanions computed here is also consistent with established organofluorine chemistry. Perfluoroalkyl carbanions bearing a beta-fluorine are known to be prone to beta-fluoride elimination to form fluorinated alkenes, a recognized and often facile decomposition pathway for such species, and the low carbanion barriers found here, 16.8 and 10.1 kcal/mol for the C_2 and C_3 fragments, are consistent with this reactivity.[76] The mechanistic sequence considered here, decarboxylation to a carbanion followed by fluoride elimination to an alkene, is likewise the pathway reported for the defluorination of PFCAs by Trang et al., who identified the volatile two-carbon fragment as the reason for the poor defluorination of PFPrA.[76] Their assignment is structural: the two-carbon anion lacks the γ-carbon required by the hydroxylation cascade operating in their system. The barriers computed here refine that assignment

to a kinetic one: elimination from the two-carbon fragment is accessible but essentially thermoneutral, and its defluorination rises from 41% to 89% between 250 and 300 °C, so the fragment is a bottleneck that yields to harsher conditions rather than a structural terminus. The present results place that qualitative picture on a quantitative footing and extend it to hydrothermal aqueous conditions.

The computed reaction free energies distinguish the two eliminations thermodynamically as well as kinetically. The C_3 elimination is strongly exergonic, at -17.3 kcal/mol, whereas the C_2 elimination is essentially thermoneutral, at -1.9 kcal/mol, a value inside the expected error of the implicit-solvent treatment for a reaction liberating a fluoride ion. Thermoneutrality implies reversibility: fluoride addition to tetrafluoroethylene to give the pentafluoroethyl anion is established chemistry,[92] so the C_2 elimination may operate close to equilibrium where the C_3 elimination is effectively irreversible. The 15.4 kcal/mol separation between the two reaction free energies exceeds an ordinary alkene substituent effect and was therefore verified by re-optimization of perfluoropropene under tighter convergence criteria and by a twenty-five step conformer scan of the perfluoropropyl carbanion; both checks left the value unchanged (Appendix A.4). The likely physical origin is that the linear perfluoropropyl carbanion produced by PFBA decarboxylation is destabilized relative to its branched isomer, consistent with fluoride addition to perfluoropropene favoring the secondary anion.

The barriers and the reaction free energies track one another: in both models the more exergonic elimination has the lower barrier. This is the Bell-Evans-Polanyi correlation, which Evans and Polanyi derived as an approximation for series in which a lateral centre is varied while the transferred atom is unchanged, and expected to apply generally to such series.[93] The correlation emerged from two independently constructed sets of calculations, the neutral base-assisted set and

the carbanion set, and its appearance across both is internal consistency evidence that the computed asymmetry between the fragments is physical rather than an artifact of either model.

5.5.3 Mechanistic Interpretation: Reaction Rate Against Contact Time

The barrier difference alone does not fully explain the experimental selectivity; the complete picture requires the fate of each fragment after it forms. Following decarboxylation, the perfluoroalkyl fragment can either undergo elimination that leads to defluorination or revert to the neutral 1H-perfluoroalkane, which is released unreacted at depressurization or separates from the reacting media in the reactor. The C_2 fragment presents the higher base-assisted elimination barrier, thus requires longer contact time, so a larger fraction can remain unreacted and be released at depressurization or separate from the liquid as an immiscible phase, leading to low fluoride recovery. The C_3 fragment has a lower barrier (by 7.5 kcal/mol), so re-activation outcompetes phase separation, resulting in significantly higher defluorination compared to PFPrA. The aqueous medium is a single compressed liquid at 25 MPa throughout, so the second phase available to the fragment is its own immiscible phase rather than steam, and the fragment can separate within the heated section or leave at depressurization. The relevant comparison is therefore the reaction rate against the time before the fragment separates or the effluent depressurizes, not a difference in ambient boiling points. This comparison has been applied to the parent compounds: in a sealed reactor at 280 °C, PFCA defluorination rates rise as the chain shortens, and the ordering is assigned to partitioning of the parent between vapor and liquid.[77] This hypothesis does not hold against the presented results, because parent destruction here is essentially completed at T~ 225 - 250 °C at every NaOH loading, including 0 M NaOH, so parent partitioning away from the liquid phase cannot be rate-controlling. Defluorination here must be governed by the fate of the fragment, not of the parent.

This competition is not fixed but responds to reaction conditions. Increasing the hydroxide concentration relative to the fragment favors capture of the fragment as the carbanion before depressurization, and consistent with this, defluorination of PFPrA improved when the hydroxide-to-fragment ratio was raised. This concentration dependence would not be expected if loss of the fragment were unconditional; its observation supports the interpretation of defluorination as a competition between reaction rate and molecular contact time, in which the hydroxide ion reacts with a PID molecule dissolved in the aqueous phase. It also clarifies the role of hydroxide, which is to generate and regenerate the reactive carbanion rather than to participate directly in the fluoride-eliminating step, since the carbanion eliminates fluoride without further assistance.

differ in an important way. Once the carbanion is formed, it has a low elimination barrier, 16.8 and 10.1 kcal/mol, at which point, given sufficient temperature and OH^- species, it rapidly releases the fluoride. The variation in defluorination route occurs at the elimination barrier bottleneck, when the neutral hydrofluorocarbons are present, and the base-assisted barriers are the highest (29.9 and 22.4 kcal/mol). The controlling question is therefore whether hydroxide can re-deprotonate the hydrofluorocarbon and return it to the productive channel faster than the contact time allows, and that comparison, not the carbanion barrier, differs decisively between the C_2 and C_3 fragments. Raising temperature increases defluorination for both fragments but does not close the difference between them. The contribution of fragment partitioning is bounded in Appendix D. The effluent still carries unreacted C_2 fragment.

The PID fragment set is determined by the competition between molecular-level reaction and the PID partitioning from the reactive liquid phase. Both C2 and C3 1H-perfluoroalkanes fragments are in their supercritical state at AH conditions (T> 150 °C, P> 22.1 MPa), e.g., C2F5H -- Tcr= 66°C, Pcr= 3.59 MPa, and C_3F_7H -- Tcr ~102.0 - 105 °C, Pcr= 2.99 MPa. Weakly polar

supercritical fluids have poor miscibility with liquid water and other polar solvents. [94] [95] [96-98] As the less reactive C_2F_5H molecule forms during the decomposition of PFPrA, it must react with hydroxide ions before it separates as an immiscible phase. High temperature and NaOH concentration promote the reaction, while higher PFPrA levels promote separation of the fragment as an immiscible phase.

5.5.4 Proposed Mechanism of PFBA and PFPrA Destruction

Hydrothermal treatment of TFA proceeds by thermal decarboxylation to the trifluoromethyl carbanion and carbon dioxide. The carbanion abstracts a proton from water to give fluoroform. Under alkaline conditions, fluoroform is mineralized to fluoride, formate, and carbonate. Decarboxylation is rate-determining, and the measured rate does not depend on NaOH concentration.[37]

Austin et al. transformed TFA in compressed liquid water at 150 to 250 °C and below 30 MPa, at a residence time of approximately 10 minutes, in the same two reactors used here. Without NaOH, the carbon and fluorine were not recovered in the liquid phase; gas-phase FTIR identified TFA, CO_2, and CHF_3. At a twentyfold excess of NaOH, only CO_2 was identified in the gas. At 0.4 M NaOH, fluoride formed stoichiometrically and the fluorine balance closed at 100 plus or minus 6 percent, which the authors report as indicating that fluoroform reacts with OH- before it can leave the reactor. The liquid products at 200 °C were fluoride, formate, and carbonate, with bicarbonate absent because the effluent pH is well above the second dissociation constant of carbonic acid.[37]

Austin et al. hypothesized that this sequence should hold for longer PFCAs, with decarboxylation yielding the corresponding 1H-perfluoroalkane and NaOH then defluorinating that species. They reported the fate of the longer 1H-perfluoroalkanes in alkaline media as uninvestigated.[37] Here, that hypothesis is tested for the C_3 and C_4 acids. The pathways proposed below are hypothesized

from the products observed in this work together with reactions established in the literature; steps that lack direct support are inferred, and the schemes mark them as proposed.

Figure 5.21 sets out the generalized pathway. TFA, PFPrA, and PFBA share one first step. Thermal scission of the carbon-carboxyl bond gives a perfluoroalkyl carbanion and carbon dioxide, and the rate does not depend on NaOH loading for any of the three acids. Without NaOH, the carbanion is protonated by water to the hydrofluorocarbon $F(CF_2)_nH$. Destruction is complete at that point, and no further fluoride is released. NaOH reopens the sequence. The carbanion then eliminates fluoride by two routes. For n greater than or equal to 2, beta-fluoride elimination gives the perfluoroalkene. For n equal to 1, no beta-fluorine exists, and alpha-elimination gives difluorocarbene. Multiple hydroxide-mediated steps carry each fragment to the products discussed later in this study.

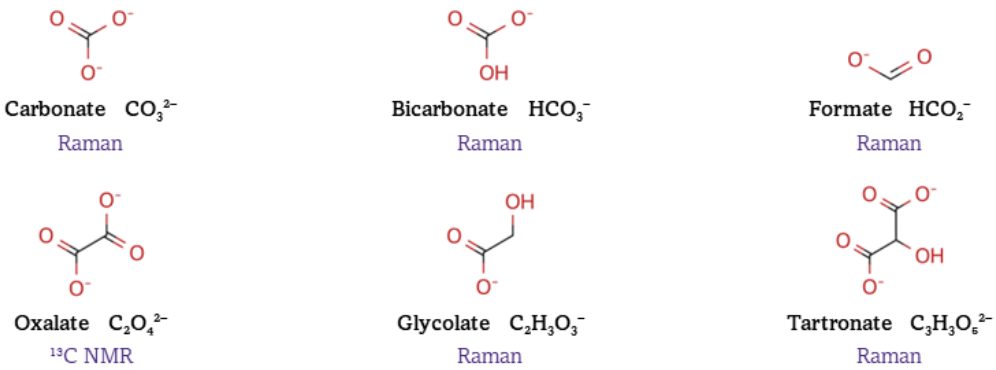

Figure 5.20: Structures of the carbon-containing products identified in this work. Carbonate, bicarbonate, formate, glycolate, and tartronate were quantified by Raman; oxalate was identified by carbon-13 NMR. Each species is drawn as the anion predominant at the pH of these experiments.

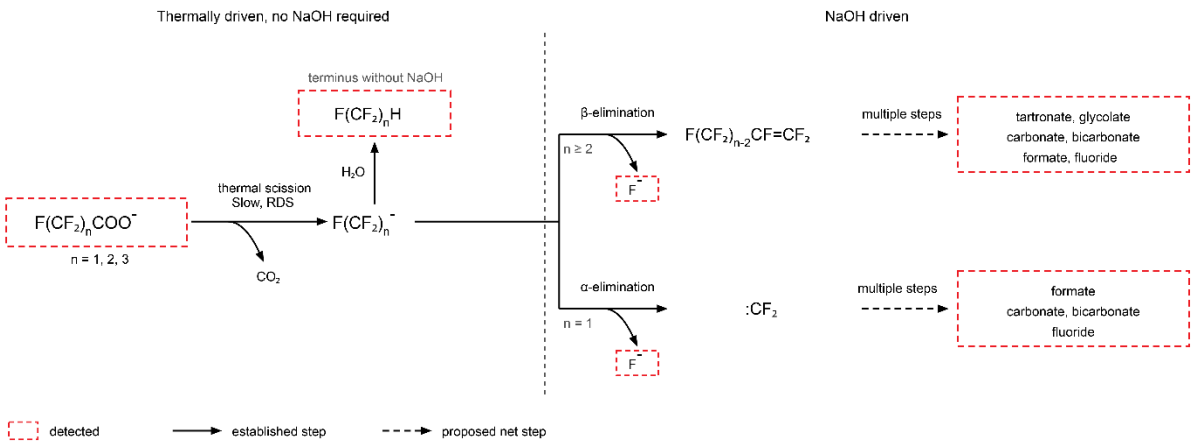

Figure 5.21: Generalized degradation pathway for perfluoroalkyl carboxylates in continuous-flow AH at 25 MPa. Thermal scission of the carbon-carboxyl bond gives a perfluoroalkyl carbanion and carbon dioxide and does not require NaOH. Without NaOH, the carbanion is protonated by water to the hydrofluorocarbon, which is the terminus. With NaOH, the carbanion eliminates fluoride, by beta-elimination to the perfluoroalkene for n greater than or equal to 2 and by alpha-elimination to difluorocarbene for n equal to 1. Here, n equal to 1 is TFA, n equal to 2 is PFPrA, and n equal to 3 is PFBA. Boxed species were detected; species boxed for n equal to 1 are reported by Austin et al..[37] The perfluoroalkene and difluorocarbene were not detected and are proposed intermediates, and the alpha-elimination step is inferred. Oxalate was resolved by carbon-13 NMR at 300 °C in 0.7 M NaOH. Water is the solvent and is omitted from the drawn products.

The one-carbon route is drawn through difluorocarbene, by analogy to the pathway for TFMS in Chapter 4. Austin et al. describe the same net conversion of fluoroform by repeated nucleophilic substitution.[37] The alpha-elimination step is inferred rather than observed. Tartronate, glycolate, and oxalate are reported as carbon-containing products of base-mediated PFCA mineralization.[76, 99]

5.5.5 Shared First Step: Decarboxylation to a Perfluoroalkyl Carbanion

At the operating pH both acids are fully deprotonated, so the reacting species is the carboxylate. Thermally activated decarboxylation cleaves the carbon-carboxyl bond to give a perfluoroalkyl carbanion and carbon dioxide: PFBA gives the perfluoropropyl carbanion $C_3F_7^-$, and PFPrA gives the perfluoroethyl carbanion $C_2F_5^-$. The same two steps are established for the sodium salt of PFBA: pyrolysis of sodium perfluorobutanoate gives perfluoropropene by decarboxylation and fluoride elimination, a route used preparatively for terminal fluoroalkenes.[92] That precedent is thermal rather than aqueous, so it establishes the sequence and not the conditions. The branch

following the carbanion is also documented for halogenated acetates: the intermediate abstracts a proton from the solvent or loses halide, and the ratio depends on structure, with dichlorofluoroacetate giving about 70% of the protonated product where chlorodifluoroacetate gives very little.[92] Decarboxylation is the rate-determining step of destruction, consistent with the absence of a clear hydroxide dependence in the measured activation energies for both acids, and Trang et al. report a computed barrier of 27.7 kcal/mol for the PFCA case with the perfluoroalkyl anion detected directly.[76] The released carbon dioxide does not persist in the alkaline medium; it is captured by hydroxide to carbonate, with the carbonate-bicarbonate speciation set by pH, so this first carbon is accounted for as carbonate from the outset.

5.5.6 The Carbanion Branch Point and the Hydrofluorocarbon Reservoir

The perfluoroalkyl carbanion has two competing fates. In the productive channel it undergoes beta-fluoride elimination to the perfluoroalkene; in the competing channel it is protonated by water to the corresponding hydrofluorocarbon, C_3F_7H from PFBA and C_2F_5H from PFPrA, both of which are unreactive on the residence time and leave at depressurization. The detection of C_3F_7H in the PFBA gas phase and of C_2F_5H in the PFPrA gas phase is the direct experimental signature of this channel.

The hydrofluorocarbons are not chemically inert. Trang et al. showed that the 1H-perfluoroalkane formed on decarboxylation re-enters the degradation cascade, and an independent study converts C_2F_5H to tetrafluoroethylene by base-mediated beta-fluoride elimination of the pentafluoroethyl anion. [76, 91]the computed base-assisted barriers make that competition strongly asymmetric. At 22.4 kcal/mol the C_3 fragment is re-activated by hydroxide on the timescale of the reaction, so most PFBA-derived carbon that transiently forms C_3F_7H returns to the productive channel. At 29.9 kcal/mol the C_2 fragment is not, so a substantial fraction of PFPrA-derived carbon leaves as

C_2F_5H before it can react. This asymmetry, rather than an absolute inertness of either compound, is why PFBA defluorinates nearly completely while PFPrA does not.

The base strength required in the literature supports the same reading. The reported conversion of C_2F_5H to tetrafluoroethylene uses potassium hexamethyldisilazide, a base far stronger than hydroxide, and is run at low temperature to control the reaction. That aqueous hydroxide is sufficient to drive this elimination for the C_3 fragment but not, on the residence times used here, for the C_2 fragment is precisely what a barrier difference of 7.5 kcal/mol predicts. [91]

Both acids were treated at 0.05 M in 0.1 M NaOH at 250 °C to test this asymmetry directly, a sub-stoichiometric NaOH loading at which the degradation cascade stalls and its intermediates accumulate rather than being driven to completion. Under these matched conditions the gas phase of the PFBA experiment contains difluoroethene, eluting at 4.4 minutes and identified by its molecular ion at m/z 64 with the expected loss of fluorine at m/z 45, and trifluoroethene, eluting at 6.7 minutes with its molecular ion at m/z 82 and loss of fluorine at m/z 63. Both are two-carbon species carrying hydrogen. Under the same conditions the PFPrA gas phase contains none of these species, and C_2F_5H is the dominant product. The comparison is given in Appendix E. Their saturated precursor is identified in the same chromatogram: 1,1,1,2-tetrafluoroethane, R-134a, elutes at 10.6 minutes with its molecular ion at m/z 102, a base peak at m/z 83 from loss of fluorine, and the trifluoromethyl fragment at m/z 69, and trifluoroethene is its dehydrofluorination product. That transformation is established over solid catalysts between 300 and 600 °C, where R-134a is barely converted without a catalyst. [100, 101] The base-mediated route at the temperatures used here is inferred from the products observed in this work rather than from that literature. The isomeric trifluoroethanes were excluded: the signal at m/z 84 matches the carbon-13 satellite of m/z 83 in both intensity, at 2.3%, and retention time, so no $C_2H_3F_3$ species is present. That exclusion removes

the saturated precursor that difluoroethene would require on an elimination-only route, so hydrogen must enter and fluorine must leave on the alkene itself in a single net exchange. Formate is a confirmed product here and carries a carbon-bound hydrogen, and the Inconel wall is nickel-bearing, so hydrogen generation at the metal surface cannot be excluded. The trifluoroethene-to-difluoroethene step is therefore drawn as a net hydrodefluorination with the hydrogen source unassigned, and it is the one step in either scheme without direct literature precedent. Where the hydrogen of R-134a itself enters is established by the route below: it is delivered by water, at the carbanion quench that closes the tetrafluoropropanoate sequence.

The presence of difluoroethene and trifluoroethene in the PFBA gas phase shows that the hydrofluorocarbon formed by protonation of the perfluoropropyl carbanion is not removed from the system: hydroxide re-activates it and returns its carbon to the degradation cascade. Re-activation proceeds by deprotonation and beta-fluoride elimination, a step class established for fluorinated substrates in alkaline superheated water at 250 °C.[102] Deprotonation of C_3F_7H at the terminal difluoromethylene gives the perfluoropropyl carbanion, the same intermediate produced by decarboxylation, and elimination returns perfluoropropene. The two olefins do not descend from the hydrofluorocarbon directly.

Saturated perfluoroalkyl groups are characterized by extreme inertness, and perfluorocarbons are essentially inert to hydrolysis unless strongly heated;[92] they resist substitution and elimination at CF_2 and CF_3 positions, and such reactions become accessible only once the carbon is returned to an unsaturated or carbanionic form, so the saturated hydrofluorocarbon is a parking state rather than a precursor. The observed olefins also require hydrogen-rich two-carbon parents: trifluoroethene is the dehydrofluorination product of a tetrafluoroethane and difluoroethene that of a trifluoroethane, neither of which is reachable from pentafluoroethane without two or three further

exchange cycles, each of which must itself pass through an alkene. The two-carbon backbone is instead delivered by the three-carbon alkene through a tetrafluoropropanoate intermediate. Hydroxide adds at the terminal difluoromethylene carbon of perfluoropropene, the site reported for nucleophilic attack on this alkene and the most reactive position toward nucleophiles; the reported case is methoxide, and the extension to hydroxide is an inference. Water quenches the carbanion, and the resulting alpha,alpha-difluoro alcohol, deprotonated at the pH of these experiments, collapses by fluoride elimination to an acyl fluoride that hydrolyzes to 2,3,3,3-tetrafluoropropanoate. Loss of fluoride from the carbanion in place of protonation gives the enol of the same acyl fluoride, so the product is the same on either branch. [92] Tetrafluoropropanoate is an alpha-hydrogen PFCA and decarboxylates by the same chemistry as the parent acids, giving the CF_3CHF carbanion whose water-quenched form is R-134a. The hydrofluorocarbon shunt and the two-carbon series are therefore parallel consequences of the same carbanion chemistry, and the detection of R-134a places the tetrafluoropropanoate hub directly in the observed inventory.

Neither species is present in the PFPrA experiment. At the retention times where difluoroethene and trifluoroethene appear in the PFBA gas phase, the PFPrA chromatogram shows no signal at m/z 64 or m/z 82, and the C_2F_5H envelope does not overlap either retention window, so the comparison is not compromised by co-elution. The same reactor, hydroxide concentration, temperature, feed concentration, and full-scan acquisition method were used for both, and the two runs were acquired on consecutive days. The difference is therefore attributable to the compound rather than to conditions. Taken with the computed barriers, this establishes that the three-carbon hydrofluorocarbon is a reversible reservoir that hydroxide reopens, whereas the two-carbon hydrofluorocarbon is a genuine terminus under every condition examined here. This absence is useful evidence in itself. PFPrA generates a two-carbon fragment directly on decarboxylation, so

if the hydrogen-bearing olefins arose from any two-carbon fragment they should appear in the PFPrA gas phase as readily as in the PFBA gas phase. They do not appear at all. Their absence therefore indicates that the two-carbon fragment of PFPrA is immobilized as C_2F_5H rather than continuing to react, which is the same conclusion reached from the computed barrier difference but obtained from an entirely separate observation. The barrier calculation and the olefin absence are two independent lines of evidence for one claim.

An independent test of the same principle is available by replacing a single fluorine with a hydrogen. The two-carbon fragment released from PFPrA is C_2F_5H, and its hydrogen-bearing analogue, differing by exactly one substitution, is the refrigerant 1,1,1,2-tetrafluoroethane (R-134a), $C_2H_2F_4$. The computed base-assisted elimination barrier falls from 29.9 kcal/mol for C_2F_5H to 23.0 kcal/mol for R-134a, essentially the value computed for the three-carbon fragment. If the barrier governs whether hydroxide can act on a saturated hydrofluorocarbon, then R-134a should defluorinate under conditions where the PFPrA system does not.

Figure 5.22 shows that it does. At twice the stoichiometric hydroxide requirement, defluorination of R-134a reaches 44% at 200 °C and 85% at 225 °C, whereas the PFPrA system reaches 0.4 and 5.1% at the same temperatures and the same hydroxide multiple. The largest separation is at 200 °C, where the two differ by a factor of 110. The comparison is not a like-for-like comparison of molecules: PFPrA is a three-carbon carboxylate that must decarboxylate before any fragment exists, whereas R-134a is the saturated two-carbon species itself. The figure therefore isolates the fate of the two-carbon fragment. The PFPrA defluorination ceiling is set by C_2F_5H rather than by decarboxylation, which the carbon balance and the gas-phase detection of C_2F_5H establish independently, so the contrast is between a fragment that hydroxide cannot re-activate and its hydrogen-bearing analogue, which hydroxide can. The gap narrows above 250 °C and the two are

within 20% of one another by 275 °C, so the substitution shifts the onset temperature by roughly 50 °C rather than changing the eventual endpoint. This is the behavior expected of an activation barrier and not of an inert compound.

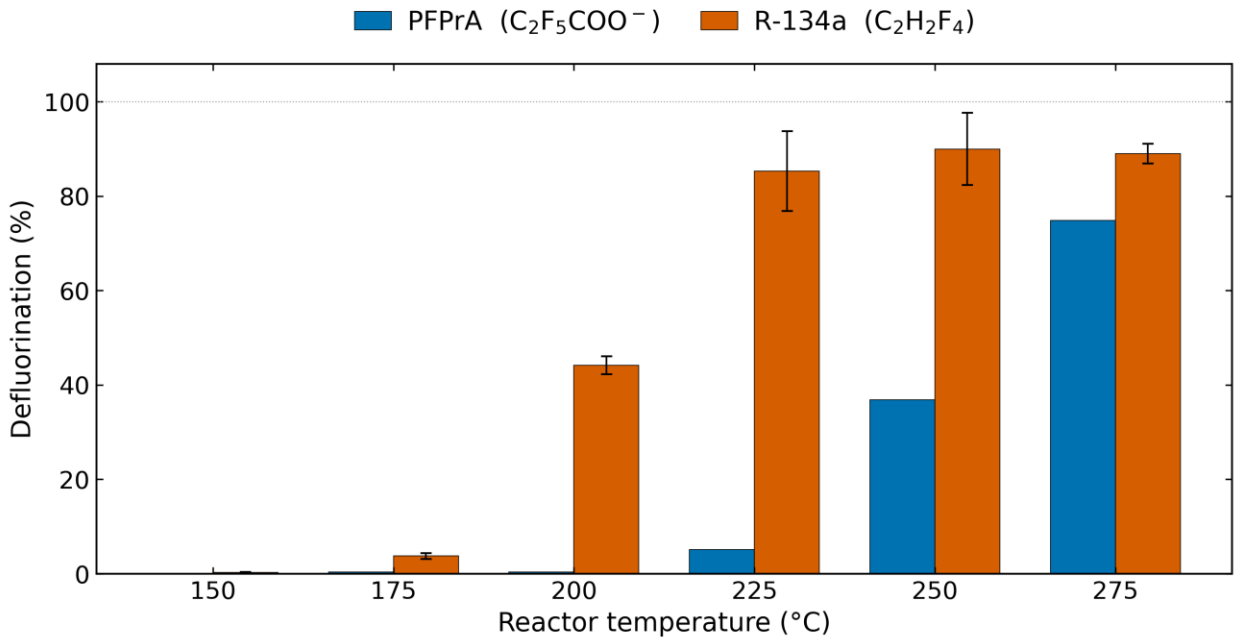

Figure 5.22: Defluorination of PFPrA and of R-134a at twice the stoichiometric hydroxide requirement, from 150 to 275 °C. Stoichiometry assumes complete bond scission, giving 0.7 M NaOH for 0.05 M PFPrA and 0.5 M NaOH for 0.035 M R-134a. Fluoride measured by ion chromatography and referenced to the theoretical maximum. R-134a error bars are the half-range of two independent IC batches; PFPrA values are single determinations and carry no error bars. PFPrA is a three-carbon carboxylate and R-134a a two-carbon saturated hydrofluorocarbon, so the comparison isolates the fate of the two-carbon fragment rather than comparing structurally matched molecules.

The R-134a data are drawn from a separate study and are reported here only for this comparison. R-134a was processed at a feed concentration of 0.035 M with a residence time of approximately 10 minutes, at the stoichiometric hydroxide requirement and at twice that requirement, with fluoride quantified by ion chromatography as for the acids. The values plotted here are those at twice the stoichiometric requirement, matching the basis used for PFPrA. The product distribution, kinetics, and degradation mechanism of R-134a are outside the scope of this dissertation, and it is used here solely as a structural control on the fragment chemistry.

5.5.7 Productive Channel: Elimination, Hydroxylation, and Defluorination

Fluoride elimination from the carbanion gives a perfluoroalkene, perfluoropropene from PFBA and tetrafluoroethylene from PFPrA. Hydroxide then adds to the terminal carbon of the alkene. The steps following decarboxylation in this cascade are computed to be low-barrier or enthalpically barrierless, with decarboxylation rate-limiting at about 28 kcal/mol, in an implicit dimethyl sulfoxide model rather than water.[76] Carbanion intermediates in nucleophilic addition to tetrafluoroethylene were demonstrated by trapping.[92] Water quenches the carbanion, and the resulting alpha,alpha-difluoro alcohol, deprotonated at the pH of these experiments, collapses by fluoride elimination to an acyl fluoride that hydrolyzes to a partially fluorinated carboxylate: 2,3,3,3-tetrafluoropropanoate from perfluoropropene and difluoroacetate from tetrafluoroethylene. For PFBA, base-mediated dehydrofluorination of tetrafluoropropanoate gives trifluoroacrylate. Dehydrofluorination of hydrofluorocarbons is established by strong base in aprotic solvent and over solid catalysts in the gas phase; [91, 101] the aqueous hydroxide version at the temperatures used here is inferred. Hydroxide addition and hydrolysis convert trifluoroacrylate to fluoromalonate, whose remaining carbon-fluorine bond sits alpha to two carboxylates and is displaced by hydroxide to give tartronate. For PFPrA, hydroxide substitution converts difluoroacetate through glyoxylate to oxalate. The terminal products of both sequences are reported. Tartronate, glycolate, and oxalate are identified as carbonaceous by-products of base-mediated PFCA mineralization, and tartronate is assigned specifically to PFBA.[76] Hydrolytic defluorination of difluoroacetate to glyoxylate is documented enzymatically:[103] two consecutive nucleophilic substitutions at the fluorinated carbon proceed through 2-fluoro-2-hydroxyacetate to the geminal diol, which is in equilibrium with glyoxylate in water. That work is at pH 7.5 and 30 °C with a carboxylate nucleophile supplied by the enzyme, so the transfer to hydroxide under alkaline hydrothermal conditions is an extension. The intermediate-by-intermediate routes drawn here remain proposed

rather than established. All eliminated fluorine reports as fluoride ion in solution. The individual fluorine-by-fluorine steps are drawn in the mechanism schemes as net multi-step transformations rather than single elementary steps, because the individual intermediates are not each isolated for these specific chain lengths.[76]

The perfluoroalkene is the one intermediate in this sequence that was not observed directly: no perfluoropropene or tetrafluoroethylene was detected in the gas phase under any condition tested. The alkene is not expected to be seen, and for different reasons in the two cases. Perfluoroalkenes are strongly electrophilic. Unlike hydrocarbon alkenes they invite nucleophilic attack, because the electronegative fluorine substituents deplete electron density at the double bond; hydroxide adds at the difluoromethylene terminus, the most positive site, and fluoride elimination follows under basic conditions. [92] An alkene generated in hot concentrated hydroxide is therefore consumed about as fast as it forms and cannot accumulate to a detectable gas-phase concentration. For PFBA this is the operative explanation, and it is required by the near-complete defluorination observed: the alkene must form and be consumed rather than vented. For PFPrA the explanation is different. There, elimination is the minor branch, so tetrafluoroethylene largely does not form in the first place and the carbon leaves instead as C_2F_5H. Reactivity toward nucleophiles also increases with fluorine substitution, so the perfluorinated alkenes are more readily consumed than the monohydro alkene, which is consistent with trifluoroethylene being detectable in the R-134a system while neither perfluoroalkene is detectable here.

The alkene step is therefore inferred rather than observed in this work, and it draws on three independent lines of published evidence. Trang et al. identified the corresponding perfluoroalkenes computationally and demonstrated that an authentic perfluoroalkene standard was competent for the degradation.[76] Base-mediated beta-fluoride elimination of the pentafluoroethyl anion to

tetrafluoroethylene has been demonstrated directly and reported to proceed without observable byproducts, which establishes that the fully fluorinated case gives the alkene rather than opening an alternative channel.[91] And superheated water with alkaline amendment defluorinates hydrogenated fluoropolymer backbones at 250 °C, within the temperature range used here. [102] None of these is hydrothermal PFCA chemistry exactly, and the extrapolation to the present conditions is an inference rather than a measurement.

5.5.8 The One-Carbon Branch: Trifluoromethyl Cleavage, Difluorocarbene, and Fluoroform

Fluoroform was detected in the gas phase of the sub-stoichiometric PFBA experiment, at 0.05 M acid in 0.1 M NaOH at 250 °C. Its presence requires a one-carbon fluorinated fragment, and the route by which that fragment arises is constrained by the results already presented. It cannot originate from the hydrofluorocarbon reservoir, because the two-carbon hydrofluorocarbon does not reopen on these residence times, and it cannot arise by direct carbon-carbon cleavage of the perfluoroalkyl carbanions, because beta-fluoride elimination from the bare carbanions, at 10.1 and 16.8 kcal/mol, consumes them long before any higher-barrier cleavage can compete. These are carbanion barriers and are not comparable with the base-assisted barriers of 22.4 and 29.9 kcal/mol computed for the neutral hydrofluorocarbons. Fragmentation of the two-carbon carbanion to the trifluoromethyl anion and difluorocarbene has been computed at 43.6 kcal/mol against 20.8 kcal/mol for its beta-fluoride elimination, a gap that makes the cleavage route uncompetitive.[91] The trifluoromethyl anion is instead liberated after hydroxylation, on the PFBA side of the chemistry: enolization and alpha-fluoride substitution of tetrafluoropropanoate give trifluoropyruvate, a trifluoromethyl ketone, and base cleavage of the carbon-carbon bond adjacent to the carbonyl is documented for trifluoromethyl aryl ketones in aqueous alkali, where the ketone is fully hydrated, the reactive species is the hydrate anion, and the leaving group is the trifluoromethyl anion. [104] Trifluoropyruvate is likewise hydrated and is deprotonated at the pH

used here, so the same reactive species is available, but the extension from an aryl ketone to an alpha-keto acid is an inference, and the oxalate co-product follows from the carbon count. The cleavage is slow at ambient temperature, by a factor of 5.3×10^{10} relative to the trichloro analogue at 25 °C, and the present assignment requires it to be accessible at 250 °C. The PFPrA system provides no trifluoromethyl-bearing intermediate on this route, so the one-carbon branch belongs to the PFBA chemistry alone and is drawn only in that scheme.

The chemistry of the one-carbon fragment differs from that of the longer fragments in a way that matters for the carbon balance. The trifluoromethyl anion has no beta carbon, so the beta-fluoride elimination that carries the two- and three-carbon fragments into the productive channel is structurally unavailable to the trifluoromethyl anion. It proceeds instead by alpha-elimination of fluoride to difluorocarbene. Hydrolysis of fluoroform with sodium or potassium hydroxide at 140 °C gives fluoride and formate, with small quantities of carbon monoxide, which is the net transformation drawn here at 250 °C. [105] The carbene is hydrolyzed by hydroxide and water, the route first established for the haloforms.[106] Both sources give carbon monoxide alongside formate. Formate is the species observed in this work; carbon monoxide could not be resolved from air at m/z 28 in the gas-phase method used. The formate is subsequently converted to carbonate, releasing hydrogen. This is the same one-carbon sequence established for TFMS in Chapter 4, where the trifluoromethyl anion is generated directly by carbon-sulfur cleavage and the route from carbene to formate to carbonate is drawn as inferred; the density functional theory in Chapter 4 covers the thermal route only. The one-carbon branch is therefore not a lower-barrier version of the same elimination but a separate mechanism, and that distinction is why fluoroform is mineralized under conditions where the two-carbon hydrofluorocarbon is not.

Fluoroform is diagnostic of this branch rather than a product of the productive channel. It was detected only when hydroxide was sub-stoichiometric, and it is absent once hydroxide is supplied in excess. The branch predicts this pattern: the trifluoromethyl anion is formed under both conditions, and its fate changes. When hydroxide is limiting the anion is protonated and leaves as fluoroform, whereas when hydroxide is plentiful the alpha-elimination route competes successfully and the carbon is carried through to formate and carbonate. Protonation of the trifluoromethyl anion to fluoroform is exergonic by 10.6 kcal/mol, whereas loss of fluoride to difluorocarbene is endergonic by 9.8 kcal/mol, but this protonation is reversible in strong base: hydroxide deprotonates fluoroform back to the trifluoromethyl anion, and the endergonic alpha-elimination is pulled forward because the carbene is consumed irreversibly downstream, so fluoroform is a reservoir in pre-equilibrium with the anion rather than a competing sink.[91] The detection of fluoroform is therefore evidence that the trifluoromethyl anion forms, and its disappearance at full hydroxide is evidence that the one-carbon fragment is mineralized rather than lost. The one-carbon branch differs from the hydrofluorocarbon reservoir here: the two-carbon species persists at every NaOH loading examined. Formate observed in the PFPrA system above 225 °C, quantified by Raman at 1352 cm^{-1}, is accounted for on the two-carbon path, as the reported decomposition product of aqueous oxalate under hydrothermal conditions. [107] Difluorocarbene itself was not observed. It follows from the absence of a beta carbon on the trifluoromethyl anion and from the corresponding pathway established for TFMS, and it is drawn as an inferred step. No first-order saddle exists for fluoride loss from the trifluoromethyl anion: the computed surface rises monotonically toward the dissociation limit, so the alpha-route cannot be placed in the beta-elimination barrier series, and the branch rests on structural and product evidence rather than on a barrier comparison.

5.5.9 Terminal Products and Carbon Fate

For PFBA the oxidative-defluorination cascade converts the perfluoropropyl fragment to tartronate (a three-carbon hydroxy-acid), which is retained as the dominant organic product. A minor fraction decarboxylates to glycolate, a two-carbon hydroxy-acid that is also a terminal product. The one-carbon head-group pool appears as carbonate or bicarbonate depending on pH. This is consistent with the products identified in the present work, glycolate, tartronate, carbonate, and bicarbonate, and with the glycolate and tartronate assignments confirmed by carbon-13 NMR in Figure 5.5. The carbon balance for the four-carbon parent distributes between two products: the decarboxylation carbon becomes carbonate, and the three-carbon perfluoropropyl-derived backbone becomes tartronate, which is retained rather than converted to carbonate.[76]

For PFPrA the two-carbon backbone is conserved from the carbanion through tetrafluoroethylene and difluoroacetate to glyoxylate and oxalate. In the present experiments carbonate is the dominant carbon product and oxalate is resolved by carbon-13 NMR only at 300 °C in 0.7 M NaOH, so oxalate is treated here as an intermediate rather than a terminus. Aqueous oxalate degrades fastest at low pH, and at the pH used here it is present essentially entirely as the dianion,[107] so it is expected to persist longer than the other intermediates drawn. The rise of carbonate above the one-third ceiling only above 250 °C is consistent with that persistence. The proposed carbon fate for the retained fraction of PFPrA is mineralization to carbonate, with difluoroacetate and glyoxylate short-lived and oxalate the longest-lived of the three, while the fraction lost to the hydrofluorocarbon reservoir leaves as C_2F_5H. Formate, observed above 225 °C, enters this accounting through the two-carbon backbone as a decomposition product of oxalate, and has been reported to be more stable than oxalate under hydrothermal conditions.[107] This two-exit picture is what produces the observed one-third carbonate ceiling: of three carbons, one is released as carbon

dioxide on decarboxylation and captured as carbonate, and of the remaining two-carbon fragment, the portion that is not quenched to volatile C_2F_5H is mineralized.[76]

5.5.10 Reconciling the Fluorine and Carbon Balances

The two balances describe two different atoms taking two different exits and should be closed independently. Carbon retained in solution is driven to carbonate, while carbon and fluorine lost to the protonation channel leave as hydrofluorocarbon gas that is inert on the residence times used here. A defluorination value below 100% is therefore not evidence of an incomplete mechanism; it reflects the fraction of carbanion quenched to the hydrofluorocarbon before beta-elimination can compete. A complete accounting requires that the aqueous organic and carbonate carbon plus the hydrofluorocarbon off-gas carbon equal the parent carbon, and that the aqueous fluoride plus the off-gas carbon-fluorine equal the parent fluorine. The near-complete defluorination of PFBA and the ceiling-limited defluorination of PFPrA are the two limiting cases of this single accounting, differing only in how much fragment is released unreacted.

The proposed pathways are summarized in the mechanism schemes of Figure 5.23, Figure 5.24 and Figure 5.25. Solid arrows denote steps established in cited work or computed in this work; dashed arrows denote proposed net transformations that comprise several elementary steps; boxed species, including fluoride, denote detection in this work; and curved arrows mark every fluoride-releasing step, with the boxed fluoride counts along each branch summing to the fluorine content of the parent acid.

For PFBA, decarboxylation gives the perfluoropropyl carbanion and carbon dioxide, which is captured as carbonate. The carbanion is either protonated by water to C_3F_7H or eliminates beta-fluoride to perfluoropropene, and at a base-assisted elimination barrier of 22.4 kcal/mol the hydrofluorocarbon is re-activated by hydroxide on the reaction timescale. Hydroxide addition,

water quench, and alkoxide collapse convert perfluoropropene to 2,3,3,3-tetrafluoropropanoate, the hub of the scheme, from which three routes lead onward: dehydrofluorination and hydrolysis along the spine, the three-carbon backbone route, through trifluoroacrylate and fluoromalonate to tartronate, the dominant retained product, which in a minor branch decarboxylates to a terminal glycolate; decarboxylation and quench to R-134a, which dehydrofluorinates to trifluoroethene and then, by net hydrodefluorination, to difluoroethene, reaching the terminal glycolate; and cleavage of the derived trifluoromethyl ketone to the trifluoromethyl anion, which is quenched to fluoroform or hydrolyzed through difluorocarbene to formate and carbonate.

For PFPrA the same first step gives the perfluoroethyl carbanion and carbon dioxide, again captured as carbonate. The carbanion is protonated by water to C_2F_5H or eliminates beta-fluoride to tetrafluoroethylene, but at a base-assisted barrier of 29.9 kcal/mol, 7.5 kcal/mol above the corresponding C_3 fragment, aqueous hydroxide does not re-activate C_2F_5H on the residence times used here. Hydroxide addition, water quench, and alkoxide collapse convert tetrafluoroethylene to difluoroacetate, which hydroxide substitution carries through glyoxylate to oxalate and on to carbonate. Tetrafluoroethylene is inferred rather than observed, and its absence reflects the elimination branch being minor rather than the alkene being consumed. Glyoxylate sets the two-carbon product. It is carried mainly to oxalate under strong base and can also disproportionate to glycolate and oxalate by a Cannizzaro reaction, so both follow from the same intermediate without an added hydride donor. The PFPrA series resolves oxalate, consistent with the solvothermal report that glyoxylate without a methanol hydride donor is carried mainly to oxalate.[99] The PFBA series resolves glycolate, which the disproportionation supplies and which decarboxylation of tartronate supplies additionally through a three-carbon route absent for PFPrA. The difference follows from the backbone length and the operating conditions, not from a different fragment chemistry.

Two points of provenance apply to the schemes. Glycolate was resolved by Raman deconvolution at 0.5 M NaOH and 250 °C only, and tartronate was quantified by Raman deconvolution against the calibration of Appendix B. The trifluoroethene to difluoroethene step has no direct literature precedent and is the one hypothesis step in either scheme.

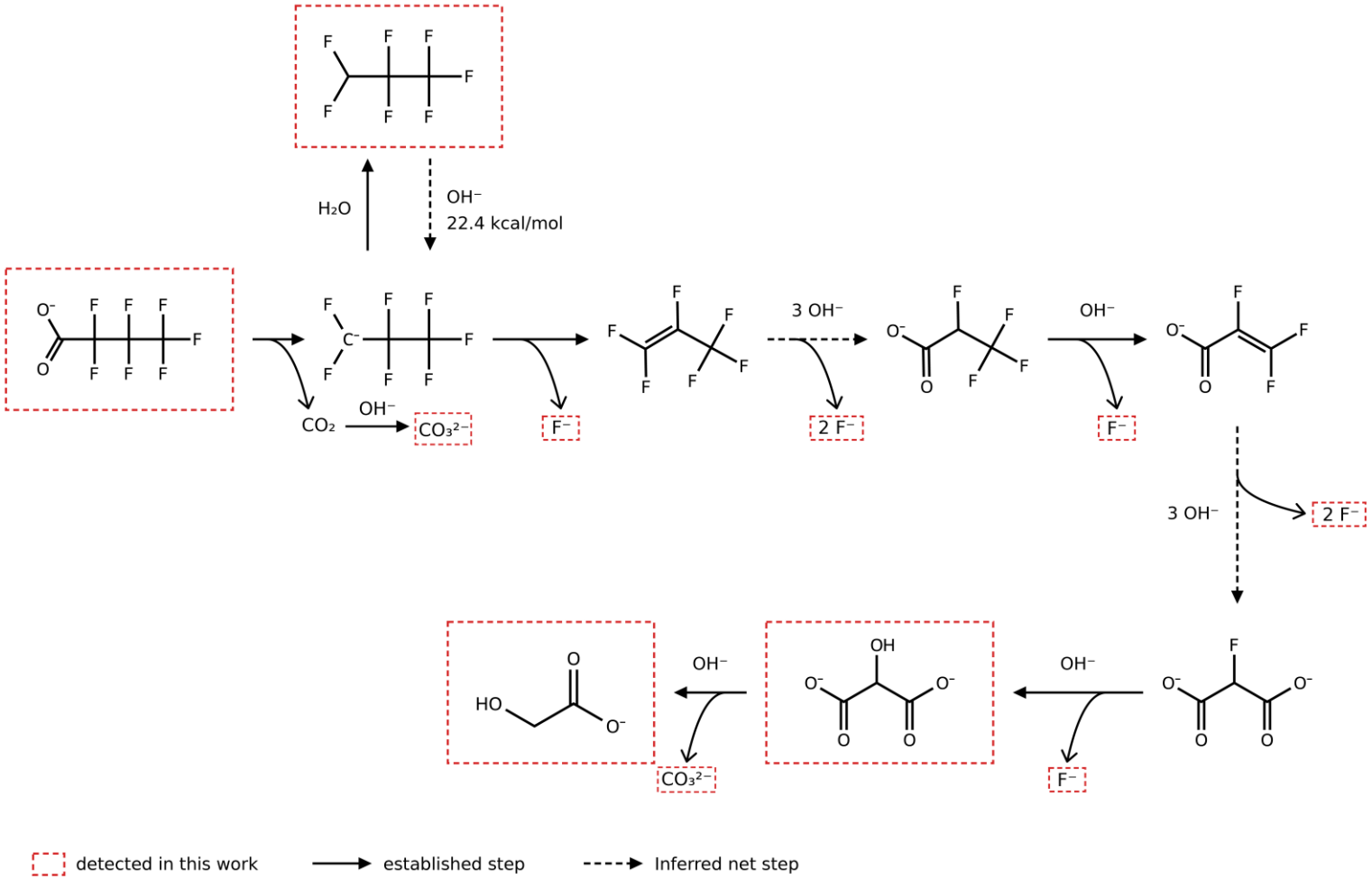

Figure 5.23: PFBA destruction at 25 MPa: the three-carbon spine and the hydrofluorocarbon reservoir. Boxed species were detected in this work. The computed base-assisted elimination barrier is shown on the re-activation arrow. Water is the solvent and is omitted from the drawn products. Perfluoropropene, 2,3,3,3-tetrafluoropropanoate, trifluoroacrylate, and fluoromalonate were not detected and are proposed intermediates.

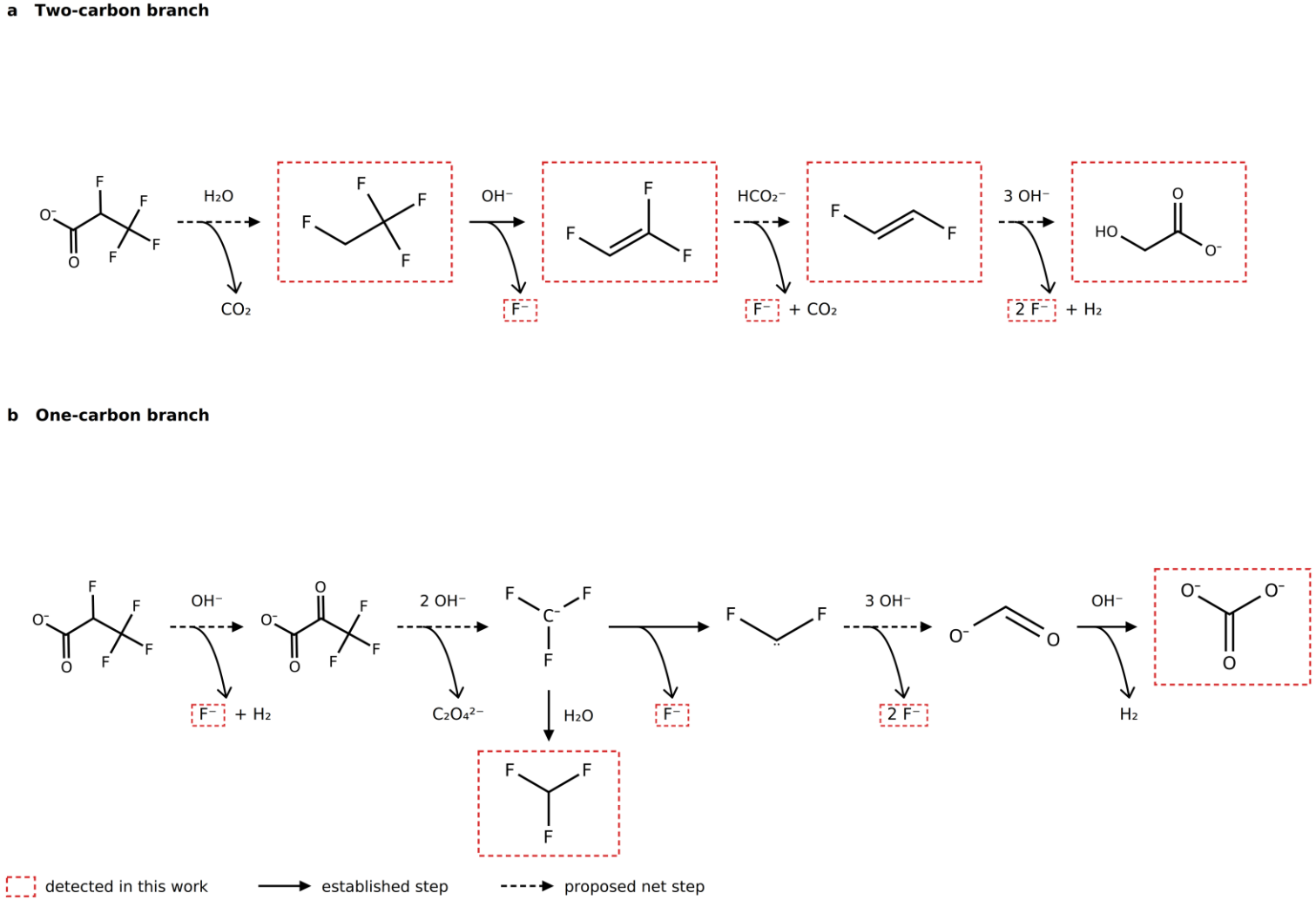

Figure 5.24: Branches from 2,3,3,3-tetrafluoropropanoate in the PFBA scheme. (a) Two-carbon branch, reaching the terminal glycolate. (b) One-carbon branch: cleavage of trifluoropyruvate liberates the trifluoromethyl anion, which is either quenched to fluoroform or loses fluoride to difluorocarbene and is carried on to carbonate. The gases were detected only at sub-stoichiometric hydroxide (0.05 M PFBA, 0.1 M NaOH, 250 °C) and are consumed at 0.5 and 1 M NaOH. Trifluoropyruvate, the trifluoromethyl anion, difluorocarbene, and formate were not detected and are proposed intermediates.

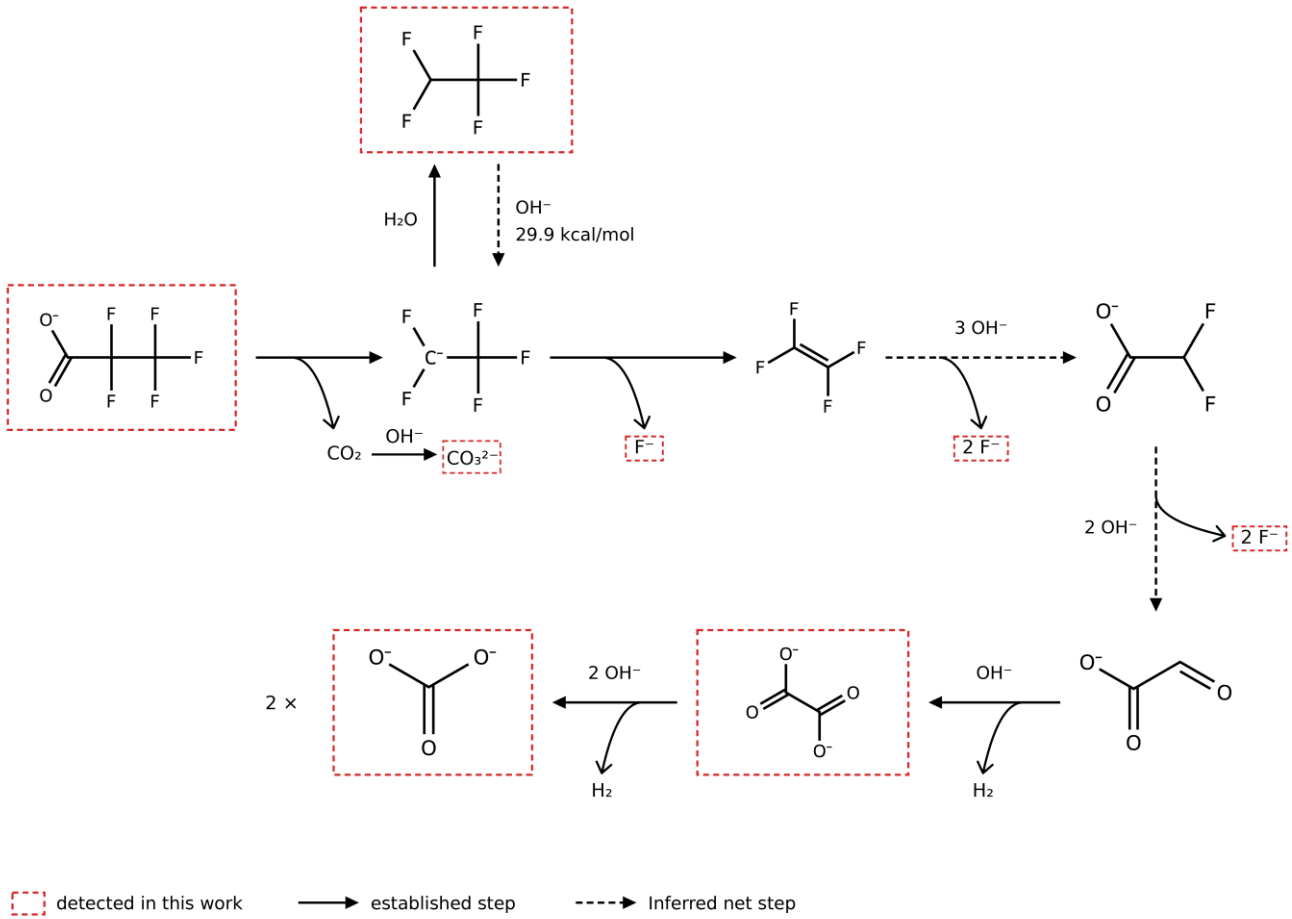

Figure 5.25: PFPrA destruction at 25 MPa. C_2F_5H was detected by GC-MS in every condition tested; boxed fluoride counts sum to the five fluorines of the parent. Computed base-assisted elimination barriers are shown on the re-activation arrows here and in the PFBA scheme: re-activation of C_2F_5H is not competitive on the residence times used at 250 °C but becomes so above 275 °C. Tetrafluoroethylene, difluoroacetate, and glyoxylate were not detected and are proposed intermediates. No route to a one-carbon fluorinated fragment exists, so no fluoroform branch is drawn. Water is the solvent and is omitted from the drawn products.

5.6 Summary

Under conventional single-phase alkaline hydrolysis, PFBA and PFPrA are destroyed with comparable activation energies, 97 to 122 kJ/mol and 129 to 132 kJ/mol respectively, with no clear hydroxide dependence. PFBA defluorinates nearly completely, while PFPrA plateaus at 41% at 250 °C. PFBA yields glycolate, tartronate, carbonate, bicarbonate, and the volatile C_3F_7H; PFPrA yields carbonate, oxalate and formate, and the volatile fragment C_2F_5H is detected in the gas phase. Density functional theory establishes that the two-carbon fragment from PFPrA has an elimination barrier that is 7.5 kcal/mol higher than the three-carbon fragment from PFBA. The two-carbon fragment reacts too slowly to be consumed within the allowed contact time before phase separation occurs and gas-phase PID leaves the reactor unreacted. That defluorination is governed by the balance of kinetic rates of decomposition products and their miscibility in the reactive aqueous media. On the bulk fluid level, this competition can be influenced by operating temperature, alkali levels, and concentration of the PIDs produced during PFCA decomposition.

Chapter 6: Synthesis and Conclusions

6.1 Cross-Compound Comparison

Three compounds spanning head-group chemistry and chain length were examined: the ultrashort-chain PFSA (TFMS), and the ultrashort-chain (PFPrA) and short-chain (PFBA) PFCAs. Transformation of the parent compound and release of its fluorine as fluoride are multi-step compound-specific processes involving multi-phase reactions and phase transitions.

For the PFCAs, parent destruction exceeds 99.9% at T~ 225 -250 °C. PFBA mineralization approaches completion by 225 to 250 °C. For PFPrA, defluorination depends on NaOH concentration, temperature, and PFPrA flow rates. This behavior was examined for the alkali-free case, which establishes that scission of the parent proceeds thermally and does not require alkali amendment. Defluorination behaves in the opposite way. It remains at background without NaOH for both acids and rises steeply with base, reaching 97 to 98% for PFBA by 225 to 250 °C but only 41% for PFPrA at 250 °C at comparable NaOH loading, with PFPrA requiring 275 to 300 °C to reach 78 and 89% defluorination. The apparent activation energies for destruction overlap between the two acids in two of the three fitted pairs, whereas defluorination at 250 °C differs by a factor of 2-3x. Due to differences in the activation energy of PFCA decomposition fragments, defluorination is governed by the balance of the kinetic rates of decomposition products and their miscibility in the reactive aqueous media. On the bulk fluid level, this competition can be influenced by operating temperature, alkali levels, and concentration of the PIDs produced during PFCA decomposition.

TFMS shows a similar separation, with the limitation at the other step. Conventional treatment leaves approximately 13% of the parent unconverted even at 5 M NaOH, so the limitation is alkaline demand, not accessibility. Both expanded regimes address that demand by exploiting the

phase behavior of the medium rather than by raising the reagent dose: SIM-AH by raising the critical point to 406.6 °C and 29.7 MPa through addition of 3 wt% NaCl, and DAH by lowering the pressure into the two-phase region so that hydroxide concentrates in the residual liquid. SIM-AH reached DRE above 99.9% with 2 M NaOH, a 2.5-fold reduction in alkali demand relative to conventional operation at 5 M NaOH, and DAH reached DRE above 99.99% with 0.5 M NaOH, a 10-fold reduction.

6.1.1 Destruction Kinetics Across the Series

The apparent activation energies for parent destruction are collected in Table 6.1, with trifluoroacetic acid measured previously in the same reactor and the one literature value available for a long-chain PFCA.

Table 6.1: Apparent activation energies for the destruction of fluorinated compounds under hydrothermal conditions. Carbon counts exclude the head-group carbon. The TFMS value is for carbon-sulfur cleavage; all other values are for decarboxylation. The PFOA value is a defluorination rate constant measured in a batch reactor and is not directly comparable to the destruction values.

Compound	Carbons	Quantity measured	Ea (kJ/mol)	Source
PFOA	7	Defluorination, batch	146	Literature
PFBA	3	Destruction	97 to 122	This work
PFPrA	2	Destruction	129 to 132	This work
TFA	1	Destruction	191 ± 8	Same reactor
TFMS*	1	Destruction	145 to 208	This work

*The TFMS activation energy depends on NaOH concentration, because cleavage of the carbon-sulfur bond requires hydroxide. The PFCA values are for thermal decarboxylation and show no dependence on NaOH.

Across the PFCAs measured in this reactor, the barrier rises from 97 to 122 kJ/mol for PFBA and 129 to 132 kJ/mol for PFPrA to 191 ± 8 kJ/mol for TFA.[37] Two of the three PFBA fits overlap the PFPrA values within their fitted uncertainties, so the two acids are not cleanly separated on destruction kinetics. The PFCAs are destroyed under relatively mild conditions, and they differ in the decomposition fragment. TFA, with a single perfluorinated carbon remaining after decarboxylation, has higher activation energy than both longer chain PFCAs.

The 146 kJ/mol reported for PFOA is an activation energy for defluorination, measured as a second-order rate constant in 1.2 mol/kg NaOH between 513 and 573 K, not for parent destruction, so it is not directly comparable with the destruction barriers measured here. It is of the same order, which supports the general trends that these are thermal barriers of similar magnitude rather than processes separated by orders of magnitude.[77] It is not, however, a good data point for this comparison. It was obtained by second-order kinetics in a batch reactor at 240 to 300 °C, and it describes defluorination rather than parent compound destruction. These can be driven by different processes with different rate-limiting steps, so the PFOA value is reported here as a literature anchor and not as chain-length dependence extending to eight carbons.

The TFMS range of 145 to 208 kJ/mol is comparable to the 191 ± 8 kJ/mol of TFA, the one-carbon carboxylate, and of the same order as the longer PFCAs, despite corresponding to a different elementary step, the cleavage of a carbon-sulfur bond rather than a carbon-carboxyl bond. This comparison matters because it shows that the recalcitrance of the PFSAs under alkaline hydrolysis is not a matter of an intrinsically higher barrier to breaking the head group off. It follows instead from the NaOH dependence: TFA destruction shows no dependence on NaOH concentration, confirming purely thermal decarboxylation, whereas TFMS destruction depends on NaOH, so the reaction requires base, not heat alone.

This comparison has two limits. The measurements span different temperature windows, 150 to 250 °C for the PFCAs and 350 to 400 °C for TFMS, so the barriers are not obtained over a common range and an Arrhenius fit extrapolated outside its window may not be reliable. The TFMS values also show a wider spread than the carboxylate values, 145 to 208 kJ/mol against fitted uncertainties of 13 to 23 kJ/mol at each individual hydroxide concentration, so the range reflects variation between NaOH concentrations rather than the precision of any one fit.

6.2 Mechanistic Insights

After the head group is removed, the fragment either eliminates fluoride or is protonated to a hydrofluorocarbon. For TFMS, density functional theory established heterolytic carbon-sulfur bond cleavage as the rate-determining step, with nucleophilic substitution by hydroxide controlling degradation under alkaline conditions and thermal heterolysis becoming competitive only when hydroxide is limited. Fluoroform detected at 400 °C in the absence of base is the experimental signature of that competing route.

For the PFCAs the same branch explains the chain-length difference. Decarboxylation is thermally driven and produces a perfluoroalkyl fragment, which either eliminates beta-fluoride and continues toward mineralization or is protonated to a volatile hydrofluorocarbon. The computed base-assisted elimination barriers for those hydrofluorocarbons are 22.4 kcal/mol for the three-carbon fragment and 29.9 kcal/mol for the two-carbon fragment. That difference of 7.5 kcal/mol is decisive. Hydroxide re-activates the three-carbon fragment and returns its carbon to the cascade, whereas the two-carbon fragment is not re-activated at that temperature: at 250 °C it leaves the reactor as pentafluoroethane, and re-activation becomes competitive only some 50 °C higher, where defluorination reaches 78% at 275 °C and 89% at 300 °C at unchanged NaOH loading. Both hydrofluorocarbons were detected in the gas phase, and at 250 °C the addition of 1 M NaOH suppressed the three-carbon species by more than two orders of magnitude across all five diagnostic ions while leaving the two-carbon species unchanged.

Two further observations support this trend. Under sub-stoichiometric hydroxide the PFBA system yields difluoroethene and trifluoroethene, hydrogen-bearing two-carbon species that can only arise if hydroxide re-activates the hydrofluorocarbon and the resulting cascade stalls for want of base; neither appears in the PFPrA system under matched conditions. And replacing a single fluorine

with hydrogen on the two-carbon fragment lowers the computed barrier from 29.9 to 23.0 kcal/mol, essentially the value of the three-carbon fragment, with a corresponding restoration of defluorination measured experimentally; the same species is detected as an intermediate in the

The liquid-phase products are consistent with this framework. PFBA yields tartronate as the dominant organic product above 200 °C, together with glycolate, carbonate, and bicarbonate at lower pH. PFPrA yields carbonate as the dominant product with formate above 225 °C and oxalate as a transient intermediate, and no tartronate or glycolate at any condition, consistent with a shorter backbone that cannot support a three-carbon hydroxy-acid.

6.3 Engineering and Economic Implications

The alkali reductions of Chapter 4 matter because alkaline demand drives three downstream costs. Sodium hydroxide is consumed stoichiometrically rather than catalytically, so it appears in the reagent cost, in the corrosion duty on the reactor, and in the neutralization and total dissolved solids burden of the effluent. Reducing the demand 2.5-fold under SIM-AH and 10-fold under DAH therefore acts on all three at once. No quantitative cost or life-cycle analysis was performed in this work, and the reductions reported here are chemical rather than economic.

Two constraints apply to scale-up. Both expanded regimes were designed to remain subcritical, which keeps inorganic salts in solution and avoids the precipitation and plugging that constrain supercritical processes, but DAH deliberately operates in the two-phase region and its hydroxide enrichment is transient and local to the reactor, so it cannot be verified in the effluent and must be inferred from destruction and product data. For the ultrashort- and short-chain PFCAs, temperature is the effective variable, not NaOH loading. At 250 °C the two-carbon fragment is not defluorinated within the residence time, so additional NaOH raises cost without a proportional gain in defluorination. Raising the temperature to 275 to 300 °C recovers the fragment at

unchanged NaOH loading. Suppressing gas-phase PID emissions requires consuming the fragment within the contact time, through longer residence time or higher temperature.

6.4 Conclusions

Four conclusions follow from this work.

- Destruction and defluorination are separate processes under hydrothermal alkaline conditions. The parent compound is broken thermally, and fluoride is released only when NaOH is available to act on the fragment that scission produces. Reporting destruction efficiency alone therefore overstates what has been achieved.

- The extent of defluorination for the ultrashort- and short-chain PFCAs is governed by the elimination barrier of that fragment, not by chain length as such. The 7.5 kcal/mol difference between the two-carbon and three-carbon fragments shifts the onset of defluorination by roughly 50 °C, so that at 250 °C the three-carbon fragment is essentially fully defluorinated while the two-carbon fragment is below 40%.

- The two compound classes are limited at different steps, and the difference is where NaOH is required rather than how hard the molecule is to break. For the PFCAs, scission of the head group is thermal and proceeds without base; NaOH is required only afterwards, to re-activate the fragment that scission releases, so the limitation is downstream of destruction and shows up as incomplete defluorination. For TFMS, cleavage of the carbon-sulfur bond requires NaOH, so the limitation is the alkaline demand of the first step. The apparent activation energies are of the same order across the series, with TFMS at 145 to 208 kJ/mol comparable to the one-carbon carboxylate TFA, so the difference is not an intrinsically higher barrier at the head group but the dependence on NaOH. The gas phase reflects the

same difference in where base is required. For the PFCAs the parent is destroyed almost completely, so the saturated hydrofluorocarbons C_3F_7H and C_2F_5H carry a large fraction of the fluorine out of the reactor unless NaOH re-activates them within the residence time. For TFMS the head group does not cleave without base, so the parent largely survives and only minor fluoroform forms by the competing thermal route when NaOH is limited.

- For the most recalcitrant PFSA the limitation is alkaline demand rather than accessibility. Delaying or exploiting the phase transition of the medium rather than raising the reagent dose reduces that demand 2.5- to 10-fold while retaining destruction efficiency above 99.9%.

6.5 Future Work

Five directions remain open: two from the expanded regimes, two from the fragment chemistry, and one from the schemes themselves.

The first is to apply SIM-AH and DAH beyond TFMS. Both regimes were developed on the most recalcitrant compound of the PFSA class and achieved high destruction at reduced alkali loading. Neither has been applied to any other compound. The next step is to run them on PFOS and on the other regulated PFSAs, and then on the real streams that AH is meant to treat: aqueous film-forming foam, foam-fractionation concentrate, spent granular activated carbon, and contaminated groundwater. Whether the alkali reduction survives a mixed feed determines whether the regimes transfer beyond the single-compound case reported here. Sodium chloride was chosen here because its phase behavior is well described, but other non-volatile salts would shift the critical point differently, and choosing the salt becomes a way to tune the operating window.

The second is to measure what DAH does inside the reactor. The hydroxide enrichment is inferred from destruction and product data, because the enriched liquid never leaves the hot zone as a separate stream. Sampling the two phases directly, or measuring conductivity in situ, would replace that inference with a number. A reactor built around the phase split rather than one that merely tolerates it could go further, drawing off the water-rich vapor, condensing it, and returning the concentrated liquid to the inlet. That design also raises the questions this work did not address: how the alloys hold up at high salt and high alkali, how the dissolved solids are managed downstream, and what the whole process costs per unit of PFAS destroyed.

The third is to close the gas loop for the short-chain acids. The two-carbon fragment partitions as C_2F_5H because it reacts more slowly than the residence time allows. This is a residence-time limitation as much as a chemical limitation. Recycling the off-gas to the reactor inlet, extending the residence time, and raising the temperature each increase the NaOH exposure of the fragment before depressurization. Raising the temperature recovers the fragment in the PFPrA system, where defluorination reaches 89% at 300 °C at unchanged NaOH loading. The same reasoning points to a second use for the process. Refrigerants such as R-134a and R-125 are being phased out under the Kigali Amendment, and they enter this cascade one step below the acids, so a single AH process could co-destroy both streams and recover fluoride.

The fourth is to turn the barrier into a screening tool. Whether a compound defluorinates depends on the fragment its head group releases, and the barrier for that fragment is obtained from a pair of calculations of the kind reported in Appendix A. Computing those barriers across the sulfonamides, the fluorotelomers, and the ether acids would give a map of which PFAS classes alkaline hydrolysis can mineralize, and at what temperature, before reactor testing.

The fifth is to confirm the proposed intermediates. Several species in the schemes are inferred rather than observed. Running authentic standards of tetrafluoropropanoate and fluoromalonate under these conditions would show whether they behave as the schemes require. Sub-stoichiometric hydroxide proved a useful way to stall the cascade and trap its intermediates as gases, and the same approach applies to other PFAS classes. One step, the net hydrodefluorination of trifluoroethene to difluoroethene, has no literature precedent and no assigned hydrogen source. Isotopic labeling of formate would establish whether formate supplies the hydrogen, and would distinguish that route from hydrogen generated at the reactor wall. Together, these directions share a single aim: to develop hydrothermal alkaline hydrolysis into a general, fluoride-recovering treatment for the ultrashort- and short-chain PFAS that current methods leave behind.

References

(1) Kurwadkar, S.; Dane, J.; Kanel, S. R.; Nadagouda, M. N.; Cawdrey, R. W.; Ambade, B.; Struckhoff, G. C.; Wilkin, R. Per- and polyfluoroalkyl substances in water and wastewater: A critical review of their global occurrence and distribution. *The Science of the total environment* **2022**, *809*, 151003-151003. DOI: 10.1016/j.scitotenv.2021.151003.
(2) Kucharzyk, K. H.; Darlington, R.; Benotti, M.; Deeb, R.; Hawley, E. Novel treatment technologies for PFAS compounds: A critical review. *Journal of environmental management* **2017**, *204* (Pt 2), 757-764. DOI: 10.1016/j.jenvman.2017.08.016.
(3) Vatankhah, H.; Anderson, R. H.; Ghosh, R.; Willey, J.; Leeson, A. A review of innovative approaches for onsite management of PFAS-impacted investigation derived waste. *Water research (Oxford)* **2023**, *247*, 120769. DOI: 10.1016/j.watres.2023.120769.
(4) Agency, U. S. E. P. *PFAS National Primary Drinking Water Regulation*; Federal Information & News Dispatch, LLC, Washington, 2024. https://www.federalregister.gov/documents/2024/04/26/2024-07773/pfas-national-primary-drinking-water-regulation.
(5) Zhi, Y.; Lu, X.; Munoz, G.; Yeung, L. W. Y.; De Silva, A. O.; Hao, S.; He, H.; Jia, Y.; Higgins, C. P.; Zhang, C. Environmental Occurrence and Biotic Concentrations of Ultrashort-Chain Perfluoroalkyl Acids: Overlooked Global Organofluorine Contaminants. *Environmental science & technology* **2024**, *58* (49), 21393-21410. DOI: 10.1021/acs.est.4c04453.
(6) Ateia, M.; Maroli, A.; Tharayil, N.; Karanfil, T. The overlooked short- and ultrashort-chain poly- and perfluorinated substances: A review. *Chemosphere (Oxford)* **2019**, *220*, 866-882. DOI: 10.1016/j.chemosphere.2018.12.186.
(7) Smalling, K. L.; Romanok, K. M.; Bradley, P. M.; Morriss, M. C.; Gray, J. L.; Kanagy, L. K.; Gordon, S. E.; Williams, B. M.; Breitmeyer, S. E.; Jones, D. K.; et al. PFAS in United States tapwater: Comparison of underserved private-well and public-supply exposures and associated health implications. *Environment international* **2023**, *178*, 108033. DOI: 10.1016/j.envint.2023.108033.
(8) Gagliano, E.; Sgroi, M.; Falciglia, P. P.; Vagliasindi, F. G. A.; Roccaro, P. Removal of poly- and perfluoroalkyl substances (PFAS) from water by adsorption: Role of PFAS chain length, effect of organic matter and challenges in adsorbent regeneration. *Water research (Oxford)* **2020**, *171*, 115381. DOI: 10.1016/j.watres.2019.115381.
(9) Hao, S.; Reardon, P. N.; Choi, Y. J.; Zhang, C.; Sanchez, J. M.; Higgins, C. P.; Strathmann, T. J. Hydrothermal Alkaline Treatment (HALT) of Foam Fractionation Concentrate Derived from PFAS-Contaminated Groundwater. *Environmental Science & Technology* **2023**, *57* (44), 17154-17165. DOI: 10.1021/acs.est.3c05140.
(10) Padhye, L. P.; Kah, M.; Leitao, E. M.; Bowles, K.; Nathanail, P.; Cousins, I. T.; Figuière, R.; Clarke, B. O.; Partington, J. M.; Alghamdi, W.; et al. The PFAS roadmap–Navigating a path together to improved management. *Sustainability Science and Technology* **2026**, *3* (1), 012501. DOI: 10.1088/2977-3504/ae286f.
(11) Guelfo, J. L.; Higgins, C. P. Subsurface Transport Potential of Perfluoroalkyl Acids at Aqueous Film-Forming Foam (AFFF)-Impacted Sites. *Environmental science & technology* **2013**, *47* (9), 4164-4171. DOI: 10.1021/es3048043.
(12) Scheurer, M.; Nödler, K.; Freeling, F.; Janda, J.; Happel, O.; Riegel, M.; Müller, U.; Storck, F. R.; Fleig, M.; Lange, F. T.; et al. Small, mobile, persistent: Trifluoroacetate in the water cycle

– Overlooked sources, pathways, and consequences for drinking water supply. *Water research (Oxford)* **2017**, *126*, 460-471. DOI: 10.1016/j.watres.2017.09.045.
(13) Scott, B. F.; Macdonald, R. W.; Kannan, K.; Fisk, A.; Witter, A.; Yamashita, N.; Durham, L.; Spencer, C.; Muir, D. C. G. Trifluoroacetate Profiles in the Arctic, Atlantic, and Pacific Oceans. *Environmental science & technology* **2005**, *39* (17), 6555-6560. DOI: 10.1021/es047975u.
(14) Miao, X.; Ma, W.; Tian, Y.; Luo, H.; Xing, Y.; Zhan, L.; Pan, Y.; Sheng, N.; Dai, J. Environmental Occurrence, Source Identification, and Health Hazards of Ultrashort-Chain PFAS in the Yangtze River Delta. *Environmental science & technology* **2025**, *59* (47), 25138-25150. DOI: 10.1021/acs.est.5c09274.
(15) Buck, R. C.; Franklin, J.; Berger, U.; Conder, J. M.; Cousins, I. T.; de Voogt, P.; Jensen, A. A.; Kannan, K.; Mabury, S. A.; van Leeuwen, S. P. J. Perfluoroalkyl and polyfluoroalkyl substances in the environment: Terminology, classification, and origins. *Integrated environmental assessment and management* **2011**, *7* (4), 513-541. DOI: 10.1002/ieam.258.
(16) Interstate Technology and Regulatory Council. *PFAS Technical and Regulatory Guidance Document and Fact Sheets PFAS-1*. 2022. https://pfas-1.itrcweb.org/ (accessed August 1, 2026).
(17) Yang, S.; Fernando, S.; Holsen, T. M.; Yang, Y. Inhibition of Perchlorate Formation during the Electrochemical Oxidation of Perfluoroalkyl Acid in Groundwater. *Environmental science & technology letters* **2019**, *6* (12), 775-780. DOI: 10.1021/acs.estlett.9b00653.
(18) Radjenovic, J.; Duinslaeger, N.; Avval, S. S.; Chaplin, B. P. Facing the Challenge of Poly- and Perfluoroalkyl Substances in Water: Is Electrochemical Oxidation the Answer? *Environmental science & technology* **2020**, *54* (23), 14815-14829. DOI: 10.1021/acs.est.0c06212.
(19) Singh, R. K.; Fernando, S.; Baygi, S. F.; Multari, N.; Thagard, S. M.; Holsen, T. M. Breakdown Products from Perfluorinated Alkyl Substances (PFAS) Degradation in a Plasma-Based Water Treatment Process. *Environmental science & technology* **2019**, *53* (5), 2731-2738. DOI: 10.1021/acs.est.8b07031.
(20) Vecitis, C. D.; Wang, Y.; Cheng, J.; Park, H.; Mader, B. T.; Hoffmann, M. R. Sonochemical Degradation of Perfluorooctanesulfonate in Aqueous Film-Forming Foams. *Environmental science & technology* **2010**, *44* (1), 432-438. DOI: 10.1021/es902444r.
(21) McIntyre, H.; Minda, V.; Hawley, E.; Deeb, R.; Hart, M. Coupled photocatalytic alkaline media as a destructive technology for per- and polyfluoroalkyl substances in aqueous film-forming foam impacted stormwater. *Chemosphere (Oxford)* **2022**, *291* (Pt 1), 132790. DOI: 10.1016/j.chemosphere.2021.132790.
(22) Zhang, H.; Chen, J.-X.; Qu, J.-P.; Kang, Y.-B. Photocatalytic low-temperature defluorination of PFASs. *Nature (London)* **2024**, *635* (8039), 610-617. DOI: 10.1038/s41586-024-08179-1.
(23) Wang, N.; Lv, H.; Zhou, Y.; Zhu, L.; Hu, Y.; Majima, T.; Tang, H. Complete Defluorination and Mineralization of Perfluorooctanoic Acid by a Mechanochemical Method Using Alumina and Persulfate. *Environmental science & technology* **2019**, *53* (14), 8302-8313. DOI: 10.1021/acs.est.9b00486.
(24) Zhang, K.; Huang, J.; Yu, G.; Zhang, Q.; Deng, S.; Wang, B. Destruction of Perfluorooctane Sulfonate (PFOS) and Perfluorooctanoic Acid (PFOA) by Ball Milling. *Environmental science & technology* **2013**, *47* (12), 6471-6477. DOI: 10.1021/es400346n.
(25) Krause, M. J.; Thoma, E.; Sahle-Damesessie, E.; Crone, B.; Whitehill, A.; Shields, E.; Gullett, B. Supercritical Water Oxidation as an Innovative Technology for PFAS Destruction. *Journal of environmental engineering (New York, N.Y.)* **2022**, *148* (2), 1-8. DOI: 10.1061/(ASCE)EE.1943-7870.0001957.

(26) Li, J.; Austin, C.; Moore, S.; Pinkard, B. R.; Novosselov, I. V. PFOS destruction in a continuous supercritical water oxidation reactor. *Chemical engineering journal (Lausanne, Switzerland : 1996)* **2023**, *451*, 139063. DOI: 10.1016/j.cej.2022.139063.
(27) Marrone, P. A.; Hong, G. T. Corrosion control methods in supercritical water oxidation and gasification processes. *The Journal of Supercritical Fluids* **2009**, *51* (2), 83-103. DOI: http://dx.doi.org/10.1016/j.supflu.2009.08.001.
(28) Pinkard, B. R.; Shetty, S.; Stritzinger, D.; Bellona, C.; Novosselov, I. V. Destruction of perfluorooctanesulfonate (PFOS) in a batch supercritical water oxidation reactor. *Chemosphere (Oxford)* **2021**, *279*, 130834. DOI: 10.1016/j.chemosphere.2021.130834.
(29) Austin, C.; Li, J.; Moore, S.; Purohit, A.; Pinkard, B. R.; Novosselov, I. V. Destruction and defluorination of PFAS matrix in continuous-flow supercritical water oxidation reactor: Effect of operating temperature. *Chemosphere (Oxford)* **2023**, *327*, 138358. DOI: 10.1016/j.chemosphere.2023.138358.
(30) Yang, J.; Wang, S.; Li, Y.; Tang, X.; Wang, Y.; Xu, D.; Guo, Y. Effect of salt deposit on corrosion behavior of Ni-based alloys and stainless steels in supercritical water. *The Journal of supercritical fluids* **2019**, *152*, 104570. DOI: 10.1016/j.supflu.2019.104570.
(31) Wu, B.; Hao, S.; Choi, Y.; Higgins, C. P.; Deeb, R.; Strathmann, T. J. Rapid Destruction and Defluorination of Perfluorooctanesulfonate by Alkaline Hydrothermal Reaction. *Environmental Science & Technology Letters* **2019**, *6* (10), 630-636. DOI: 10.1021/acs.estlett.9b00506.
(32) Hao, S.; Choi, Y.-J.; Wu, B.; Higgins, C. P.; Deeb, R.; Strathmann, T. J. Hydrothermal Alkaline Treatment for Destruction of Per- and Polyfluoroalkyl Substances in Aqueous Film-Forming Foam. *Environmental Science & Technology* **2021**, *55* (5), 3283-3295. DOI: 10.1021/acs.est.0c06906.
(33) Hao, S.; Choi, Y. J.; Deeb, R. A.; Strathmann, T. J.; Higgins, C. P. Application of Hydrothermal Alkaline Treatment for Destruction of Per- and Polyfluoroalkyl Substances in Contaminated Groundwater and Soil. *Environmental Science & Technology* **2022**, *56* (10), 6647-6657. DOI: 10.1021/acs.est.2c00654.
(34) Soker, O.; Hao, S.; Trewyn, B. G.; Higgins, C. P.; Strathmann, T. J. Application of Hydrothermal Alkaline Treatment to Spent Granular Activated Carbon: Destruction of Adsorbed PFASs and Adsorbent Regeneration. *Environmental science & technology letters* **2023**, *10* (5), 425-430. DOI: 10.1021/acs.estlett.3c00161.
(35) Pinkard, B. R.; Austin, C.; Purohit, A. L.; Li, J.; Novosselov, I. V. Destruction of PFAS in AFFF-impacted fire training pit water, with a continuous hydrothermal alkaline treatment reactor. *Chemosphere (Oxford)* **2023**, *314*, 137681. DOI: 10.1016/j.chemosphere.2022.137681.
(36) Pinkard, B.; Smith, S. M.; Vorarath, P.; Smrz, T.; Schmick, S.; Dressel, L.; Bryan, C.; Czerski, M.; de Marne, A.; Halevi, A.; et al. Degradation and Defluorination of Ultra Short-, Short-, and Long-Chain PFASs in High Total Dissolved Solids Solutions by Hydrothermal Alkaline Treatment□Closing the Fluorine Mass Balance. *ACS ES&T engineering* **2024**, *4* (11), 2810-2818. DOI: 10.1021/acsestengg.4c00378.
(37) Austin, C.; Purohit, A. L.; Thomsen, C.; Pinkard, B. R.; Strathmann, T. J.; Novosselov, I. V. Hydrothermal Destruction and Defluorination of Trifluoroacetic Acid (TFA). *Environmental Science & Technology* **2024**, *58* (18), 8076-8085. DOI: 10.1021/acs.est.3c09404.
(38) Li, J.; Pinkard, B. R.; Wang, S.; Novosselov, I. V. Review: Hydrothermal treatment of per- and polyfluoroalkyl substances (PFAS). *Chemosphere (Oxford)* **2022**, *307* (Pt 2), 135888. DOI: 10.1016/j.chemosphere.2022.135888.

(39) Driesner, T.; Heinrich, C. A. The system H2O–NaCl. Part I: Correlation formulae for phase relations in temperature–pressure–composition space from 0 to 1000°C, 0 to 5000bar, and 0 to 1 XNaCl. *Geochimica et cosmochimica acta* **2007**, *71* (20), 4880-4901. DOI: 10.1016/j.gca.2006.01.033.
(40) Driesner, T. The system H2O–NaCl. Part II: Correlations for molar volume, enthalpy, and isobaric heat capacity from 0 to 1000°C, 1 to 5000bar, and 0 to 1 XNaCl. *Geochimica et cosmochimica acta* **2007**, *71* (20), 4902-4919. DOI: 10.1016/j.gca.2007.05.026.
(41) Hao, S.; Payton, B.; Soker, O.; Ellis, A.; Brooks, S.; Reardon, P.; Vyas, S.; Popovs, I.; Novosselov, I.; Higgins, C. P.; et al. Mineralization of Trifluoromethanesulfonate via Subcritical Hydrothermal Reaction: Reaction Mechanism and Transformation Pathways. *Environmental science & technology* **2026**, *60* (26), 18878-18889. DOI: 10.1021/acs.est.6c00018.
(42) Barzen-Hanson, K. A.; Field, J. A. Discovery and Implications of C2 and C3 Perfluoroalkyl Sulfonates in Aqueous Film-Forming Foams and Groundwater. *Environmental science & technology letters* **2015**, *2* (4), 95-99. DOI: 10.1021/acs.estlett.5b00049.
(43) O'Hagan, D. Understanding organofluorine chemistry. An introduction to the C–F bond. *Chemical Society reviews* **2008**, *37* (2), 308-319. DOI: 10.1039/B711844A.
(44) Haukås, M.; Berger, U.; Hop, H.; Gulliksen, B.; Gabrielsen, G. W. Bioaccumulation of per- and polyfluorinated alkyl substances (PFAS) in selected species from the Barents Sea food web. *Environmental pollution (1987)* **2007**, *148* (1), 360-371. DOI: 10.1016/j.envpol.2006.09.021.
(45) Steenland, K.; Fletcher, T.; Stein, C. R.; Bartell, S. M.; Darrow, L.; Lopez-Espinosa, M.-J.; Barry Ryan, P.; Savitz, D. A. Review: Evolution of evidence on PFOA and health following the assessments of the C8 Science Panel. *Environment international* **2020**, *145*, 106125. DOI: 10.1016/j.envint.2020.106125.
(46) Grandjean, P.; Andersen, E. W.; Budtz-Jørgensen, E.; Nielsen, F.; Mølbak, K.; Weihe, P.; Heilmann, C. Serum Vaccine Antibody Concentrations in Children Exposed to Perfluorinated Compounds. *JAMA : the journal of the American Medical Association* **2012**, *307* (4), 391-397. DOI: 10.1001/jama.2011.2034.
(47) Lin, H.; Niu, J.; Liang, S.; Wang, C.; Wang, Y.; Jin, F.; Luo, Q.; Huang, Q. Development of macroporous Magnéli phase Ti4O7 ceramic materials: As an efficient anode for mineralization of poly- and perfluoroalkyl substances. *Chemical engineering journal (Lausanne, Switzerland : 1996)* **2018**, *354*, 1058-1067. DOI: 10.1016/j.cej.2018.07.210.
(48) Schaefer, C. E.; Andaya, C.; Burant, A.; Condee, C. W.; Urtiaga, A.; Strathmann, T. J.; Higgins, C. P. Electrochemical treatment of perfluorooctanoic acid and perfluorooctane sulfonate: Insights into mechanisms and application to groundwater treatment. *Chemical engineering journal (Lausanne, Switzerland : 1996)* **2017**, *317*, 424-432. DOI: 10.1016/j.cej.2017.02.107.
(49) Asadi Zeidabadi, F.; Banayan Esfahani, E.; Moreira, R.; McBeath, S. T.; Foster, J.; Mohseni, M. Structural dependence of PFAS oxidation in a boron doped diamond-electrochemical system. *Environmental research* **2024**, *246*, 118103. DOI: 10.1016/j.envres.2024.118103.
(50) Stratton, G. R.; Dai, F.; Bellona, C. L.; Holsen, T. M.; Dickenson, E. R. V.; Mededovic Thagard, S. Plasma-Based Water Treatment: Efficient Transformation of Perfluoroalkyl Substances in Prepared Solutions and Contaminated Groundwater. *Environmental science & technology* **2017**, *51* (3), 1643-1648. DOI: 10.1021/acs.est.6b04215.
(51) Nau-Hix, C.; Multari, N.; Singh, R. K.; Richardson, S.; Kulkarni, P.; Anderson, R. H.; Holsen, T. M.; Mededovic Thagard, S. Field Demonstration of a Pilot-Scale Plasma Reactor for the Rapid Removal of Poly- and Perfluoroalkyl Substances in Groundwater. *ACS ES&T water* **2021**, *1* (3), 680-687. DOI: 10.1021/acsestwater.0c00170.

(52) Vecitis, C. D.; Park, H.; Cheng, J.; Mader, B. T.; Hoffmann, M. R. Treatment technologies for aqueous perfluorooctanesulfonate (PFOS) and perfluorooctanoate (PFOA). *Frontiers of environmental science & engineering* **2009**, *3* (2), 129-151. DOI: 10.1007/s11783-009-0022-7.
(53) Bentel, M. J.; Yu, Y.; Xu, L.; Li, Z.; Wong, B. M.; Men, Y.; Liu, J. Defluorination of Per- and Polyfluoroalkyl Substances (PFASs) with Hydrated Electrons: Structural Dependence and Implications to PFAS Remediation and Management. *Environmental science & technology* **2019**, *53* (7), 3718-3728. DOI: 10.1021/acs.est.8b06648.
(54) Cui, J.; Gao, P.; Deng, Y. Destruction of Per- and Polyfluoroalkyl Substances (PFAS) with Advanced Reduction Processes (ARPs): A Critical Review. *Environmental science & technology* **2020**, *54* (7), 3752-3766. DOI: 10.1021/acs.est.9b05565.
(55) Liu, Z.; Bentel, M. J.; Yu, Y.; Ren, C.; Gao, J.; Pulikkal, V. F.; Sun, M.; Men, Y.; Liu, J. Near-Quantitative Defluorination of Perfluorinated and Fluorotelomer Carboxylates and Sulfonates with Integrated Oxidation and Reduction. *Environmental science & technology* **2021**, *55* (10), 7052-7062. DOI: 10.1021/acs.est.1c00353.
(56) Yang, N.; Guan, Y.; Yang, S.; Ma, Q.; Olive, C.; Fernando, S.; Zhang, W.; Holsen, T. M.; Yang, Y. PFAS Destruction and Near-Complete Defluorination of Undiluted Aqueous Film-Forming Foams at Ambient Conditions by Piezoelectric Ball Milling. *Environmental science & technology* **2025**, *59* (3), 1854-1863. DOI: 10.1021/acs.est.4c07906.
(57) McDonough, J. T.; Kirby, J.; Bellona, C.; Quinnan, J. A.; Welty, N.; Follin, J.; Liberty, K. Validation of supercritical water oxidation to destroy perfluoroalkyl acids. *Remediation (New York, N.Y.)* **2022**, *32* (1-2), 75-90. DOI: 10.1002/rem.21711.
(58) Chiang, S.-Y. D.; Saba, M.; Leighton, M.; Ballenghien, D.; Hatler, D.; Gal, J.; Deshusses, M. A. Supercritical water oxidation for the destruction of spent media wastes generated from PFAS treatment. *Journal of hazardous materials* **2023**, *460*, 132264-132264. DOI: 10.1016/j.jhazmat.2023.132264.
(59) Webb, H.; Rosansky, S.; Al-Dirani, S. M.; Dasu, K.; Scheitlin, C. G.; Davis, J.; Chiques, L. PFAS destruction using supercritical water oxidation (SCWO) at Peterson Space Force Base. *Journal of hazardous materials letters* **2025**, *6*, 100156. DOI: 10.1016/j.hazl.2025.100156.
(60) Kriksunov, L. B.; Macdonald, D. D. Corrosion in Supercritical Water Oxidation Systems: A Phenomenological Analysis. *Journal of the Electrochemical Society* **1995**, *142* (12), 4069-4073. DOI: 10.1149/1.2048464.
(61) Song, Y.; Li, Z.; Zhu, Q.; Huang, Z.; Cheng, Z. Precipitation Behavior of Salts in Supercritical Water: Experiments and Molecular Dynamics Simulations. *Processes* **2022**, *10* (2), 423. DOI: 10.3390/pr10020423.
(62) Aleksandrov, K.; Gehrmann, H.-J.; Hauser, M.; Mätzing, H.; Pigeon, D.; Stapf, D.; Wexler, M. Waste incineration of Polytetrafluoroethylene (PTFE) to evaluate potential formation of per- and Poly-Fluorinated Alkyl Substances (PFAS) in flue gas. *Chemosphere (Oxford)* **2019**, *226*, 898-906. DOI: 10.1016/j.chemosphere.2019.03.191.
(63) Gehrmann, H.-J.; Taylor, P.; Aleksandrov, K.; Bergdolt, P.; Bologa, A.; Blye, D.; Dalal, P.; Gunasekar, P.; Herremanns, S.; Kapoor, D.; et al. Mineralization of fluoropolymers from combustion in a pilot plant under representative european municipal and hazardous waste combustor conditions. *Chemosphere (Oxford)* **2024**, *365*, 143403. DOI: 10.1016/j.chemosphere.2024.143403.
(64) de La Tour, C. C. Exposé de quelques résultats obtenu par l'action combinée de la chaleur et de la compression sur certains liquides, tels que l'eau, l'alcool, l'éther sulfurique et l'essence de pétrole rectifiée. *Ann. chim. phys* **1822**, *21* (2), 127.

(65) Andrews, T. XVIII. The Bakerian Lecture.—On the continuity of the gaseous and liquid states of matter. *Philosophical Transactions of the Royal Society of London* **1869**, (159), 575-590. DOI: 10.1098/rstl.1869.0021 (accessed 3/14/2026).
(66) Poliakoff, M.; Licence, P. Supercritical fluids: green solvents for green chemistry? *Philosophical Transactions of the Royal Society A: Mathematical, Physical and Engineering Sciences* **2015**, *373* (2057). DOI: 10.1098/rsta.2015.0018 (accessed 3/14/2026).
(67) Savage, P. E. Organic Chemical Reactions in Supercritical Water. *Chemical reviews* **1999**, *99* (2), 603-622. DOI: 10.1021/cr9700989.
(68) Peterson, A. A.; Vogel, F.; Lachance, R. P.; Fröling, M.; Antal, J. M. J.; Tester, J. W. Thermochemical biofuel production in hydrothermal media: A review of sub- and supercritical water technologies. *Energy & environmental science* **2008**, *1* (1), 32-65. DOI: 10.1039/b810100k.
(69) Wagner, W.; Pruß, A. The IAPWS Formulation 1995 for the Thermodynamic Properties of Ordinary Water Substance for General and Scientific Use. *Journal of physical and chemical reference data* **2002**, *31* (2), 387-535. DOI: 10.1063/1.1461829.
(70) Fernández, D. P.; Goodwin, A. R. H.; Lemmon, E. W.; Levelt Sengers, J. M. H.; Williams, R. C. A Formulation for the Static Permittivity of Water and Steam at Temperatures from 238 K to 873 K at Pressures up to 1200 MPa, Including Derivatives and Debye–Hückel Coefficients. *Journal of physical and chemical reference data* **1997**, *26* (4), 1125-1166. DOI: 10.1063/1.555997.
(71) Driesner, T.; Seward, T. M.; Tironi, I. G. Molecular dynamics simulation study of ionic hydration and ion association in dilute and 1 molal aqueous sodium chloride solutions from ambient to supercritical conditions. *Geochimica et cosmochimica acta* **1998**, *62* (18), 3095-3107. DOI: 10.1016/S0016-7037(98)00207-5.
(72) Davis, D. S. Vapor Pressure Nomographs for Aqueous Sodium Hydroxide Solutions. *Industrial and engineering chemistry* **1942**, *34* (9), 1131-1132. DOI: 10.1021/ie50393a027.
(73) Anderko, A.; Pitzer, K. S. Equation-of-state representation of phase equilibria and volumetric properties of the system NaCl-H2O above 573 K. *Geochimica et cosmochimica acta* **1993**, *57* (8), 1657-1680. DOI: 10.1016/0016-7037(93)90105-6.
(74) Corti, H. R.; Simonson, J. M. Densities and Apparent Molar Volumes of NaOH(aq) to the Temperature 623 K and Pressure to 30 MPa. *Journal of solution chemistry* **2006**, *35* (8), 1057-1074. DOI: 10.1007/s10953-006-9054-9.
(75) Bischoff, J. L.; Pitzer, K. S. Liquid-vapor relations for the system NaCl-H 2 O; summary of the P-T-x surface from 300 degrees to 500 degrees C. *American journal of science (1880)* **1989**, *289* (3), 217-248. DOI: 10.2475/ajs.289.3.217.
(76) Trang, B.; Li, Y.; Xue, X.-S.; Ateia, M.; Houk, K. N.; Dichtel, W. R. Low-temperature mineralization of perfluorocarboxylic acids. *Science (American Association for the Advancement of Science)* **2022**, *377* (6608), 839-845. DOI: 10.1126/science.abm8868.
(77) Endo, J.; Funazukuri, T. Hydrothermal alkaline defluorination rate of perfluorocarboxylic acids (PFCAs). *Journal of Chemical Technology & Biotechnology* **2023**, *98* (5), 1215-1221.
(78) Pinkard, B. R.; Gorman, D. J.; Rasmussen, E. G.; Kramlich, J. C.; Reinhall, P. G.; Novosselov, I. V. Kinetics of formic acid decomposition in subcritical and supercritical water – a Raman spectroscopic study. *International Journal of Hydrogen Energy* **2019**, *44* (60), 31745-31756. DOI: https://doi.org/10.1016/j.ijhydene.2019.10.070.
(79) Belsky, A. J.; Maiella, P. G.; Brill, T. B. Spectroscopy of Hydrothermal Reactions 13. Kinetics and Mechanisms of Decarboxylation of Acetic Acid Derivatives at 100−260 °C under 275 bar. *The journal of physical chemistry. A, Molecules, spectroscopy, kinetics, environment, & general theory* **1999**, *103* (21), 4253-4260. DOI: 10.1021/jp984122d.

(80) Auerbach, I.; Verhoek, F. H.; Henne, A. L. Kinetic studies on the decarboxylation of sodium trifluoroacetate in ethylene glycol. *Journal of the American Chemical Society* **1950**, *72* (1), 299-300.
(81) Lin, Y.-S.; Li, G.-D.; Mao, S.-P.; Chai, J.-D. Long-Range Corrected Hybrid Density Functionals with Improved Dispersion Corrections. *Journal of chemical theory and computation* **2013**, *9* (1), 263-272. DOI: 10.1021/ct300715s.
(82) Zheng, J.; Xu, X.; Truhlar, D. G. Minimally augmented Karlsruhe basis sets. *Theoretical chemistry accounts* **2011**, *128* (3), 295-305. DOI: 10.1007/s00214-010-0846-z.
(83) Marenich, A. V.; Cramer, C. J.; Truhlar, D. G. Universal Solvation Model Based on Solute Electron Density and on a Continuum Model of the Solvent Defined by the Bulk Dielectric Constant and Atomic Surface Tensions. *The journal of physical chemistry. B* **2009**, *113* (18), 6378-6396. DOI: 10.1021/jp810292n.
(84) Neuwald, I. J.; Hübner, D.; Wiegand, H. L.; Valkov, V.; Borchers, U.; Nödler, K.; Scheurer, M.; Hale, S. E.; Arp, H. P. H.; Zahn, D. Ultra-Short-Chain PFASs in the Sources of German Drinking Water: Prevalent, Overlooked, Difficult to Remove, and Unregulated. *Environmental science & technology* **2022**, *56* (10), 6380-6390. DOI: 10.1021/acs.est.1c07949.
(85) Björnsdotter, M. K.; Yeung, L. W. Y.; Kärrman, A.; Jogsten, I. E. Ultra-Short-Chain Perfluoroalkyl Acids Including Trifluoromethane Sulfonic Acid in Water Connected to Known and Suspected Point Sources in Sweden. *Environmental science & technology* **2019**, *53* (19), 11093-11101. DOI: 10.1021/acs.est.9b02211.
(86) Xia, X.; Zheng, Y.; Tang, X.; Zhao, N.; Wang, B.; Lin, H.; Lin, Y. Correction to "Nontarget Identification of Novel Per- and Polyfluoroalkyl Substances in Cord Blood Samples". *Environmental science & technology* **2022**, *56* (24), 18080-18080. DOI: 10.1021/acs.est.2c08543.
(87) Cai, P.; Chen, T.; Zhan, M.; Ma, X.; Takaoka, M.; Sun, C.; Li, X. Synergetic degradation of PFOS by HALT conditions enhanced by Fe-based amorphous alloys. *Journal of hazardous materials* **2025**, *486*, 137015. DOI: 10.1016/j.jhazmat.2024.137015.
(88) Pinkard, B. R.; Gorman, D. J.; Rasmussen, E. G.; Maheshwari, V.; Kramlich, J. C.; Reinhall, P. G.; Novosselov, I. V. Raman Spectroscopic Data from Formic Acid Decomposition in Subcritical and Supercritical Water. *Data in Brief* **2020**, 105312.
(89) Pinkard, B. R.; Shetty, S.; Kramlich, J. C.; Reinhall, P. G.; Novosselov, I. V. Hydrolysis of Dimethyl Methylphosphonate (DMMP) in Hot-Compressed Water. *The Journal of Physical Chemistry A* **2020**, *124* (41), 8383-8389. DOI: 10.1021/acs.jpca.0c05104.
(90) Pinkard, B. R.; Kramlich, J. C.; Novosselov, I. V. Gasification Pathways and Reaction Mechanisms of Primary Alcohols in Supercritical Water. *ACS Sustainable Chemistry & Engineering* **2020**, *8* (11), 4598-4605. DOI: 10.1021/acssuschemeng.0c00445.
(91) Iwasaki, H.; Hoshiya, N.; Kishikawa, Y.; Escorihuela, J.; Shibata, N. Repurposing HFC-125 to tetrafluoroethylene: A step toward a more sustainable fluoropolymer feedstock strategy. *iScience* **2025**, *28* (6), 112580. DOI: 10.1016/j.isci.2025.112580.
(92) Chambers, R. D. *Fluorine in organic chemistry*; Blackwell Pub., 2004.
(93) Evans, M. G.; Polanyi, M. Inertia and driving force of chemical reactions. *Transactions of the Faraday Society* **1938**, *34*, 11. DOI: 10.1039/tf9383400011.
(94) Abbott, A. P.; Eardley, C. A. Solvent properties of liquid and supercritical 1, 1, 1, 2-tetrafluoroethane. *The Journal of Physical Chemistry B* **1998**, *102* (43), 8574-8578.
(95) Sabirzyanov, A. N.; Il'in, A. P.; Akhunov, A. b. R.; Gumerov, F. M. Solubility of water in supercritical carbon dioxide. *High Temperature* **2002**, *40* (2), 203-206.

(96) Feng, J.; Lau, A.; Novosselov, I. V. HKUST-1 MOF Nanoparticles: Non-classical Crystallization Route in Supercritical CO2. *Nanoscale* **2024**, 10.1039/D4NR03070B. DOI: 10.1039/D4NR03070B.
(97) Lau, A.; Feng, J.; Bossmann, S. H.; Sebastian, D.; Sorensen, C. M.; Novosselov, I. V. Continuous flow synthesis of MOF/nanocarbon composites. *Nanoscale* **2026**, 10.1039/D6NR00739B. DOI: 10.1039/D6NR00739B.
(98) Rasmussen, E. G.; Kramlich, J.; Novosselov, I. V. Scalable Continuous Flow Metal–Organic Framework (MOF) Synthesis Using Supercritical CO2. *ACS Sustainable Chemistry & Engineering* **2020**, *8* (26), 9680-9689. DOI: 10.1021/acssuschemeng.0c01429.
(99) Strijckmans, N.; Stuyck, W.; Hooyberghs, F.; Coppée, T.; Hulaj, G.; Lauwers, A.; O'Rourke, G.; Ameloot, R.; Chanut, N.; De Vos, D. E. A generic solvothermal defluorination method for carboxylate and sulfonate PFAS. *Chemical science (Cambridge)* **2026**. DOI: 10.1039/D6SC03001G.
(100) Han, T. U.; Yoo, B.-S.; Kim, Y.-M.; Hwang, B.; Sudibya, G. L.; Park, Y.-K.; Kim, S. Catalytic conversion of 1,1,1,2-tetrafluoroethane (HFC-134a). *The Korean journal of chemical engineering* **2018**, *35* (8), 1611-1619. DOI: 10.1007/s11814-018-0051-7.
(101) Jia, W.; Liu, M.; Lang, X.; Hu, C.; Li, J.; Zhu, Z. Catalytic dehydrofluorination of 1,1,1,2-tetrafluoroethane to synthesize trifluoroethylene over a modified NiO/Al 2 O 3 catalyst. *Catalysis science & technology* **2015**, *5* (6), 3103-3107. DOI: 10.1039/C5CY00211G.
(102) Hamaura, J.; Honma, R.; Hori, H.; Manseri, A.; Ameduri, B. Efficient fluoride recovery from poly(vinylidene fluoride), poly(vinylidene fluoride-co-hexafluoropropylene) copolymer and poly(ethylene-co-tetrafluoroethylene) copolymer using superheated water with alkaline reagent. *European polymer journal* **2023**, *182*, 111724. DOI: 10.1016/j.eurpolymj.2022.111724.
(103) Khusnutdinova, A. N.; Batyrova, K. A.; Brown, G.; Fedorchuk, T.; Chai, Y. S.; Skarina, T.; Flick, R.; Petit, A. P.; Savchenko, A.; Stogios, P.; et al. Structural insights into hydrolytic defluorination of difluoroacetate by microbial fluoroacetate dehalogenases. *The FEBS journal* **2023**, *290* (20), 4966-4983. DOI: 10.1111/febs.16903.
(104) Guthrie, J. P.; Cossar, J. Alkaline cleavage of trihaloacetophenones. *Canadian journal of chemistry* **1990**, *68* (9), 1640-1642. DOI: 10.1139/v90-255.
(105) Miloserdov, F. M.; Grushin, V. V. Alcoholysis of fluoroform. *J. Fluorine Chem.* **2014**, *167*, 105-109.
(106) Hine, J. Carbon dichloride as an intermediate in the basic hydrolysis of chloroform. A mechanism for substitution reactions at a saturated carbon atom. *Journal of the American Chemical Society* **1950**, *72* (6), 2438-2445. DOI: 10.1021/ja01162a024.
(107) Crossey, L. J. Thermal degradation of aqueous oxalate species. *Geochimica et cosmochimica acta* **1991**, *55* (6), 1515-1527. DOI: 10.1016/0016-7037(91)90124-N.
(108) Sander, R. Compilation of Henry's law constants (version 5.0.0) for water as solvent. *Atmospheric chemistry and physics* **2023**, *23* (19), 10901-12440. DOI: 10.5194/acp-23-10901-2023.
(109) Wagner, W.; Pruß, A. The IAPWS Formulation 1995 for the Thermodynamic Properties of Ordinary Water Substance for General and Scientific Use. *Journal of Physical and Chemical Reference Data* **2002**.
(110) Apfelbaum, E. M. The Line of Ideal Isothermal Compressibility. *The journal of physical chemistry. B* **2022**, *126* (15), 2912-2920. DOI: 10.1021/acs.jpcb.2c01247.

Appendix A. Cartesian Coordinates and Absolute Energies

This appendix reports the optimized Cartesian coordinates and absolute energies for every stationary point used in the computational analysis of the two-carbon and three-carbon fragments. All values were obtained with ORCA 6.1.1 at the wB97X-D3 / ma-def2-TZVP level with the def2/J auxiliary basis and the RIJCOSX approximation, using the SMD implicit solvent model with water as the solvent. Thermochemical quantities were evaluated at 298.15 K and 1 atm from analytical frequency calculations. Coordinates are given in angstroms and absolute energies in hartrees.

A.1 Absolute Energies

Table A.1. Absolute electronic energies, enthalpies, and Gibbs free energies in hartrees, with the number of imaginary vibrational frequencies for each stationary point.

Stationary point	Atoms	E	H	G	n(imag)
C2 reactant complex, CHF2CF3 with hydroxide	10	−652.10324146	−652.04502134	−652.08961751	0
C2 base-assisted elimination transition state	10	−652.05170266	−651.99600107	−652.04199971	1
C2F5- carbanion minimum	7	−575.61975694	−575.59018965	−575.62766099	0
C2F5- beta-fluoride elimination transition state	7	−575.59119259	−575.56273404	−575.60086470	1
Tetrafluoroethylene, CF2=CF2	6	−475.60403798	−475.57612478	−475.61000860	0
C3 reactant complex, C3HF7 with hydroxide	13	−889.93424451	−889.86211157	−889.91099900	1
C3 base-assisted elimination transition state	13	−889.89531759	−889.82556188	−889.87589210	2
C3F7- carbanion minimum	10	−813.45135580	−813.40662844	−813.45051731	0
C3F7- beta-fluoride elimination transition state	10	−813.43370907	−813.39026942	−813.43439821	1
Hexafluoropropene, CF3CF=CF2	9	−713.45833708	−713.41615771	−713.45616832	1
R-134a reactant complex, CF3CH2F with hydroxide	10	−552.84190902	−552.77727326	−552.81798380	1
R-134a base-assisted elimination transition state	10	−552.80114247	−552.73872851	−552.78237172	1
Fluoride ion, F-	1	−100.00657416	−100.00421368	−100.02073273	0

A.2 Derived Quantities

Table A.2. Quantities derived from Table A.1, in kcal per mole. A conversion factor of 627.509 kcal per mole per hartree was used. The first column follows directly from the Gibbs free energies of Table A.1. The second applies the low-frequency correction described in Section A.4 and is the value reported in the main text.

Quantity	Definition	From Table A.1	Corrected
C2 base-assisted elimination barrier	G(C2 TS) − G(C2 complex)	29.9	29.9
C3 base-assisted elimination barrier	G(C3 TS) − G(C3 complex)	22.0	22.4
C2 carbanion elimination barrier	G(C2 anion TS) − G(C2F5−)	16.8	16.8
C3 carbanion elimination barrier	G(C3 anion TS) − G(C3F7−)	10.1	10.1
R-134a base-assisted elimination barrier	G(R-134a TS) − G(R-134a complex)	22.3	23.0
C2 elimination reaction free energy	G(C2F4) + G(F−) − G(C2F5−)	−1.9	−1.9
C3 elimination reaction free energy	G(C3F6) + G(F−) − G(C3F7−)	−16.6	−17.3

A.3 Notes on the Stationary Points

Each transition state was confirmed by the presence of an imaginary vibrational frequency corresponding to carbon-fluorine bond cleavage, and, in the base-assisted pathway, to the associated proton transfer. The magnitudes of these reaction-coordinate modes are 451.6 and 493.0 cm^{-1} for the C2 and C3 base-assisted transition states, 494.6 and 520.1 cm^{-1} for the C2 and C3 carbanion transition states, and 431.5 cm^{-1} for the R-134a base-assisted transition state.

The reactant complexes for the base-assisted pathway, including that of R-134a, were obtained by constrained optimization in which the separation between the hydroxide oxygen and the acidic hydrogen was held at 1.80 angstroms. They are therefore constrained stationary points rather than fully relaxed minima. The constraint was applied so that the hydroxide would remain positioned for proton abstraction rather than migrating to an unreactive hydrogen-bonded arrangement.

Four structures carry additional small imaginary frequencies that do not correspond to a reaction coordinate. The C3 reactant complex has a mode at 15.9 cm^{-1}, the R-134a reactant complex has a mode at 25.9 cm^{-1}, the C3 base-assisted transition state has a second mode at 50.5 cm^{-1} alongside its reaction-coordinate mode, and hexafluoropropene has a mode at 18.5 cm^{-1} corresponding to hindered rotation of the trifluoromethyl group. The modes in the two reactant complexes correspond to libration of the constrained hydroxide. The treatment of these modes is described in Section A.4.

The fluoride ion is monatomic and therefore has no vibrational modes. Its Gibbs free energy comprises the electronic energy together with translational contributions only.

A.4 Verification of the Reaction Free Energies

Because the difference between the two elimination reaction free energies in Table A.2 is larger than would be expected from a simple alkene substituent effect, two additional calculations were carried out to test whether it arises from a deficiency in either structure.

Hexafluoropropene was re-optimized with tighter convergence criteria and a finer integration grid to test whether the imaginary mode noted above could be removed. The mode persisted, at 18.5 cm-1 compared with 18.3 cm^{-1} previously, which identifies it as a genuine hindered rotation of the trifluoromethyl group rather than an artifact of incomplete optimization. The Gibbs free energy changed by 0.006 kcal per mole between the two optimizations, so the reported reaction free energy is unaffected. The value in Table A.1 is taken from the tighter optimization.

The $C_3F_7^-$ carbanion was subjected to a relaxed dihedral scan through a full rotation about the bond joining the carbanion carbon to the adjacent carbon, in twenty-five steps, to test whether the optimized structure occupied a local rather than a global minimum. The profile showed the three-fold periodicity expected for rotation about a substituted carbon-carbon bond, with rotational barriers of approximately 4.8 kcal per mole. The lowest point located on the scan lay 0.016 kcal per mole above the optimized reference structure, which is within the numerical precision of the method. The optimized structure is therefore the global minimum for this conformational coordinate, and the reported reaction free energy does not arise from a poorly chosen conformer.

Treatment of low-frequency modes

ORCA omits imaginary modes from the vibrational partition function. The four spurious modes noted above are therefore absent from the reported entropies, and the corresponding Gibbs free energies are too high. At 298.15 K a mode of this magnitude contributes between 1.4 and 2.1 kcal per mole to minus T times S, offset by approximately 0.6 kcal per mole of zero-point and thermal vibrational energy, giving a net effect on the Gibbs free energy of between 0.8 and 1.5 kcal per mole per mode.

Thermochemical quantities were therefore recomputed with each spurious mode restored as its absolute value and treated with the same quasi-rigid-rotor harmonic-oscillator scheme of Grimme that ORCA applies by default to all real modes. No mode is discarded in any structure, and the same treatment is applied throughout, so the correction is not specific to the structures that exhibited imaginary frequencies. Partition functions were reconstructed from the reported

frequencies, rotational constants, molecular masses and symmetry numbers, and the implementation was verified by reproducing the ORCA Gibbs free energies of Table A.1 to within 0.001 kcal per mole for every structure before the correction was applied.

The effect is largest where a spurious mode appears on only one side of a reaction. In the C3 base-assisted profile both the reactant complex and the transition state carry such a mode, so the corrections partly cancel and the barrier rises by 0.32 kcal per mole. In the R-134a profile only the reactant complex is affected and the barrier rises by 0.66 kcal per mole. The C3 elimination reaction free energy becomes more negative by 0.75 kcal per mole because only hexafluoropropene is affected. The C2 profiles and both carbanion profiles contain no spurious modes and are unchanged. The difference between the C2 and C3 base-assisted barriers therefore decreases from 7.9 to 7.5 kcal per mole, the difference between the carbanion barriers is unchanged at 6.7 kcal per mole, and the difference in elimination reaction free energy increases from 14.6 to 15.4 kcal per mole.

As a check on the sensitivity of this treatment, the quasi-harmonic approximation of Ribeiro and co-workers was applied as an alternative, in which every frequency below 100 cm-1 in every structure is raised to 100 cm-1. That scheme gives barrier differences of 7.5 and 6.7 kcal per mole and a reaction free energy difference of 15.1 kcal per mole, in agreement with the values above. The residual uncertainty associated with the treatment of low-frequency modes is therefore of order 0.3 kcal per mole, an order of magnitude smaller than the differences on which the conclusions of this chapter rest.

A.5 Cartesian Coordinates

Coordinates are given in angstroms. For each structure the absolute Gibbs free energy in hartrees and the imaginary frequency, where one is present, are repeated for convenience.

C2 fragment, base-assisted pathway

C2 reactant complex, CHF2CF3 with hydroxide

C2HF5 with OH-, charge -1; 10 atoms; G = -652.08961751 Eh

Atom	X	Y	Z
C	-0.779100	0.259600	0.083400
F	-0.974900	0.990700	1.210300
F	-1.202100	1.005700	-0.968300
C	0.728800	0.032100	-0.074800
F	1.406900	1.180400	-0.133900
F	0.974000	-0.651700	-1.194000

F	1.195800	-0.672200	0.957600
H	-1.333500	-0.696100	0.139900
O	-1.974300	-2.372900	0.273600
H	-2.625300	-3.055400	0.455500

C2 base-assisted elimination transition state

C2HF5 with OH-, charge -1; 10 atoms; G = -652.04199971 Eh; imaginary frequency: -451.6 cm-1

Atom	X	Y	Z
C	-0.712696	0.332586	0.097386
F	-1.070291	0.945703	1.247671
F	-1.347079	0.911874	-0.946196
C	0.600320	-0.021607	-0.062562
F	1.753735	1.471680	-0.227065
F	0.969468	-0.560994	-1.200440
F	1.239923	-0.531698	0.963735
H	-1.419873	-1.641948	0.236438
O	-1.825318	-2.526852	0.319930
H	-2.771888	-2.358545	0.320402

C2 fragment, carbanion pathway

C2F5- carbanion minimum

C2F5-, charge -1; 7 atoms; G = -575.62766099 Eh

Atom	X	Y	Z
C	-0.796908	-0.217624	0.070385
F	-1.099246	0.468084	1.279687
F	-1.345359	0.655384	-0.909838
C	0.698205	0.014879	-0.077792
F	1.116921	1.306398	-0.020020
F	1.136833	-0.459625	-1.259303
F	1.376182	-0.633882	0.888053

C2F5- beta-fluoride elimination transition state

C2F5-, charge -1; 7 atoms; G = -575.60086470 Eh; imaginary frequency: -494.6 cm-1

Atom	X	Y	Z
C	-0.741407	-0.072285	0.077472
F	-1.212826	0.344857	1.282079
F	-1.458672	0.526019	-0.909918
C	0.622906	-0.116536	-0.079590
F	1.439988	1.528811	-0.035412
F	1.096331	-0.449171	-1.263264
F	1.340307	-0.628080	0.899804

Tetrafluoroethylene, CF2=CF2

C2F4, neutral; 6 atoms; G = -475.61000860 Eh

Atom	X	Y	Z
C	-0.658036	0.000000	0.000001
C	0.658037	0.000000	0.000000
F	-1.382040	1.095130	0.000000
F	-1.382039	-1.095130	-0.000001
F	1.382039	1.095130	-0.000001
F	1.382039	-1.095130	0.000001

C3 fragment, base-assisted pathway

C3 reactant complex, C3HF7 with hydroxide

C3HF7 with OH-, charge -1; 13 atoms; G = -889.91099900 Eh; imaginary frequency: -15.9 cm-1

Atom	X	Y	Z
C	1.301300	-0.116900	-0.265500
F	1.435600	1.106400	-0.842200
F	2.381600	-0.302500	0.539900
C	0.066200	-0.099700	0.647100
F	0.193500	0.838800	1.605900
F	-0.023000	-1.304900	1.245600
C	-1.281200	0.152700	-0.077700
F	-1.452600	-0.730100	-1.057200
F	-1.328300	1.377300	-0.590600
F	-2.283200	0.022700	0.788500
H	1.260900	-0.923600	-1.038600
O	1.246300	-2.295800	-2.203400
H	0.545400	-2.750800	-1.729300

C3 base-assisted elimination transition state

C3HF7 with OH-, charge -1; 13 atoms; G = -889.87589210 Eh; imaginary frequency: -493.0, -50.5 cm-1

Atom	X	Y	Z
C	1.297457	0.066303	-0.125953
F	1.423814	1.172624	-0.902031
F	2.476783	-0.156960	0.511357
C	0.139034	-0.104278	0.598777
F	-0.128923	1.025758	1.928724
F	0.108058	-1.208546	1.352272
C	-1.204451	0.171236	-0.083174
F	-1.363949	-0.595656	-1.174965
F	-1.320641	1.438609	-0.474456
F	-2.217286	-0.112713	0.734352
H	1.183117	-1.632174	-1.325393
O	1.283658	-2.433178	-1.878174
H	0.385828	-2.657424	-2.138836

C3 fragment, carbanion pathway

C3F7- carbanion minimum

C3F7-, charge -1; 10 atoms; G = -813.45051731 Eh

Atom	X	Y	Z
C	1.246872	-0.117778	-0.498939
F	1.442320	1.277566	-0.682323
F	2.366240	-0.463614	0.309412
C	0.094689	-0.194044	0.493632
F	0.241577	0.572995	1.624902
F	-0.023923	-1.477288	0.928409
C	-1.282010	0.193451	-0.096682
F	-1.590871	-0.571182	-1.143779
F	-1.311803	1.466852	-0.486286
F	-2.240335	0.027757	0.822345

C3F7- beta-fluoride elimination transition state

C3F7-, charge -1; 10 atoms; G = -813.43439821 Eh; imaginary frequency: -520.1 cm-1

Atom	X	Y	Z
C	1.226726	-0.092120	-0.363693
F	1.411317	1.133302	-0.940417
F	2.420793	-0.480041	0.180770
C	0.110775	-0.253871	0.441976
F	0.045755	0.674438	1.881946
F	0.026839	-1.457253	1.029260
C	-1.247078	0.199677	-0.105811
F	-1.550469	-0.437479	-1.248282
F	-1.276786	1.506654	-0.362458
F	-2.225116	-0.078592	0.757401

Hexafluoropropene, CF3CF=CF2

C3F6, neutral; 9 atoms; G = -713.45616832 Eh; imaginary frequency: -18.5 cm-1

Atom	X	Y	Z
C	-0.017256	0.022671	-0.000059
C	1.303879	-0.001899	0.000046
C	2.117681	-1.271563	0.000013
F	-0.724655	1.115015	-0.000022
F	-0.756113	-1.052817	-0.000203
F	1.993409	1.138405	0.000218
F	3.416045	-0.980500	-0.000214
F	1.865246	-2.030701	1.074927
F	1.864887	-2.030852	-1.074704

R-134a, base-assisted pathway

R-134a reactant complex, CF3CH2F with hydroxide

C2H2F4 with OH-, charge -1; 10 atoms; G = -552.81798380 Eh; imaginary frequency: -25.9 cm-1

Atom	X	Y	Z
C	-0.779000	0.298000	0.113000
H	-0.907000	0.910000	1.006000
F	-1.225000	1.014000	-0.990000
C	0.692000	0.016000	-0.073000
F	1.428000	1.134000	-0.183000
F	0.934000	-0.714000	-1.173000
F	1.159000	-0.671000	0.980000
H	-1.324000	-0.659000	0.184000
O	-2.008000	-2.318000	0.327000
H	-2.515000	-3.135000	0.337000

R-134a base-assisted elimination transition state

C2H2F4 with OH-, charge -1; 10 atoms; G = -552.78237172 Eh; imaginary frequency: -431.5 cm-1

Atom	X	Y	Z
C	-0.721844	0.320236	0.078462
H	-1.081706	0.740175	1.007235
F	-1.343642	0.847521	-1.044309
C	0.599143	0.006182	-0.071375
F	1.710580	1.417918	-0.140170
F	1.026842	-0.496483	-1.223320
F	1.205938	-0.573727	0.954827
H	-1.406208	-1.576682	0.263077

O	-1.792073	-2.477687	0.339498
H	-2.742028	-2.332452	0.364073

Shared species

Fluoride ion, F-

F-, charge -1; 1 atom; G = -100.02073273 Eh

Atom	X	Y	Z
F	0.000000	0.000000	0.000000

Appendix B. Analytical Calibration Curves

Quantification of liquid-phase products relies on two calibrated methods. Carbonate, bicarbonate, formate, tartronate, and trifluoromethanesulfonic acid (TFMS) were quantified by Raman spectroscopy, in which each standard spectrum was processed through the same baseline correction and non-negative least squares deconvolution used for the reactor samples, and the fitted amplitude of the species basis function was regressed against the prepared concentration. Fluoride was quantified by ion chromatography with conductivity detection, regressing integrated peak area against the concentration of the calibration standards. Every calibration is linear across the range used, with coefficients of determination from 0.9952 to 0.9999. Only the coefficient of determination is annotated on each panel; the fitted slopes and intercepts are collected in Table B.1.

Because the standards are processed identically to the samples, the calibration slope carries the full processing chain rather than a band height alone. Concentrations reported in the results chapters are obtained by inverting the fits given below. Where a fitted amplitude falls at or below zero the concentration is reported as zero rather than extrapolated, since the intercepts are not constrained to pass through the origin.

B.1 Calibration Curves and Fit Parameters

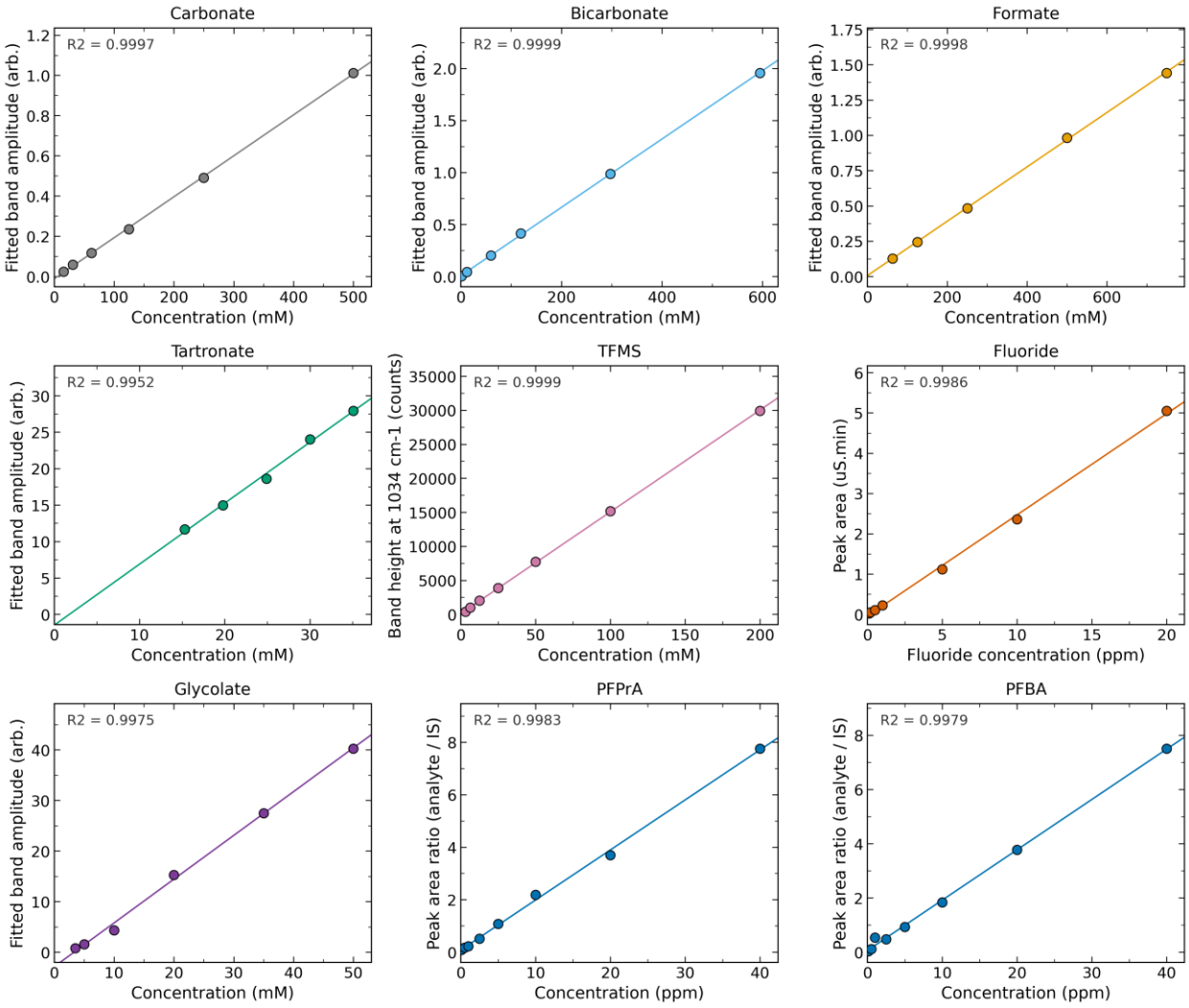

Figure B.1: Calibration curves for the species quantified in this work. Points are prepared standards; lines are least squares fits. Only the coefficient of determination is shown; full fit parameters are in Table B.1. The Raman panels for carbonate, bicarbonate, formate, tartronate, TFMS and glycolate plot the fitted basis-function amplitude from the deconvolution against concentration. The fluoride panel plots the integrated ion-chromatography peak area. The PFPrA and PFBA panels plot the LC-MS/MS peak-area ratio of analyte to the $^{13}C_4$-PFBA internal standard. Standards were sodium carbonate, sodium bicarbonate, sodium formate, tartronic acid, sodium glycolate, trifluoromethanesulfonic acid, sodium fluoride, perfluoropropanoic acid, and perfluorobutanoic acid.

Table B.1. Calibration parameters. Raman fits relate the fitted basis-function amplitude to concentration in mM; the fluoride fit relates peak area in microsiemens times minutes to concentration in ppm.

Species	Method and band	Standard	Range	Slope	Intercept	R^2	n
Carbonate	Raman, 1066 cm^{-1}	Sodium carbonate	15.6 - 500 mM	2.0366×10^{-3}	-1.1199×10^{-2}	0.9997	6
Bicarbonate	Raman, 1016 cm^{-1}	Sodium bicarbonate	0.12 - 595 mM	3.2832×10^{-3}	7.2243×10^{-3}	0.9999	7
Formate	Raman, 1352 cm^{-1}	Sodium formate	62.5 - 750 mM	1.9233×10^{-3}	6.5656×10^{-3}	0.9998	5
Tartronate	Raman, 940 cm^{-1}	Tartronic acid	15.3 - 35.1 mM	8.3691×10^{-1}	-1.49356	0.9952	5
TFMS	Raman, 1034 cm^{-1}	Trifluoromethanesulfonic acid	3.1 - 200 mM	149.547	106.807	0.9999	7
Fluoride	IC, conductivity	Sodium fluoride	0.1 - 20 ppm	2.5110×10^{-1}	-4.2850×10^{-2}	0.9986	7

B.2 Band Assignments

A linear calibration establishes that the fitted amplitude scales with concentration, but it does not by itself establish which band is being fitted. The spectra of the standards themselves are given below for that purpose. Carbonate is a single band at 1066 cm^{-1}. Bicarbonate gives 1016 and 1363 cm^{-1}. Formate gives 1352 and 1380 cm^{-1}. Tartronate gives 940, 1354, and 1437 cm^{-1} within this window. TFMS gives a strong sulfonate band at 1034 cm^{-1} and a weaker band at 1229 cm^{-1}.

Two congested regions are highlighted in the figure. The first has a direct consequence for what can be quantified. Formate scatters at 1352 cm^{-1} and tartronate at 1354 cm^{-1}, a separation of about 2 cm^{-1}, which is far below the resolution needed to separate them. The two species therefore cannot be quantified independently in the same sample. Formate is reported here only for PFPrA, where no tartronate band at 840 or 940 cm^{-1} is observed and the 1352 cm^{-1} feature can be assigned unambiguously. For PFBA, where tartronate is the dominant product, no formate concentration is reported, and the feature near 1354 cm^{-1} in those spectra is attributed to tartronate together with a parent contribution rather than to formate. The second congested region spans 1016 to 1066 cm^{-1}, where bicarbonate, TFMS, and carbonate all scatter. These three are separated by 18 to 32 cm^{-1}, which is comparable to the observed band widths, so quantification in samples containing more than one of them relies on the deconvolution using the full band shape rather than on peak height at a single position.

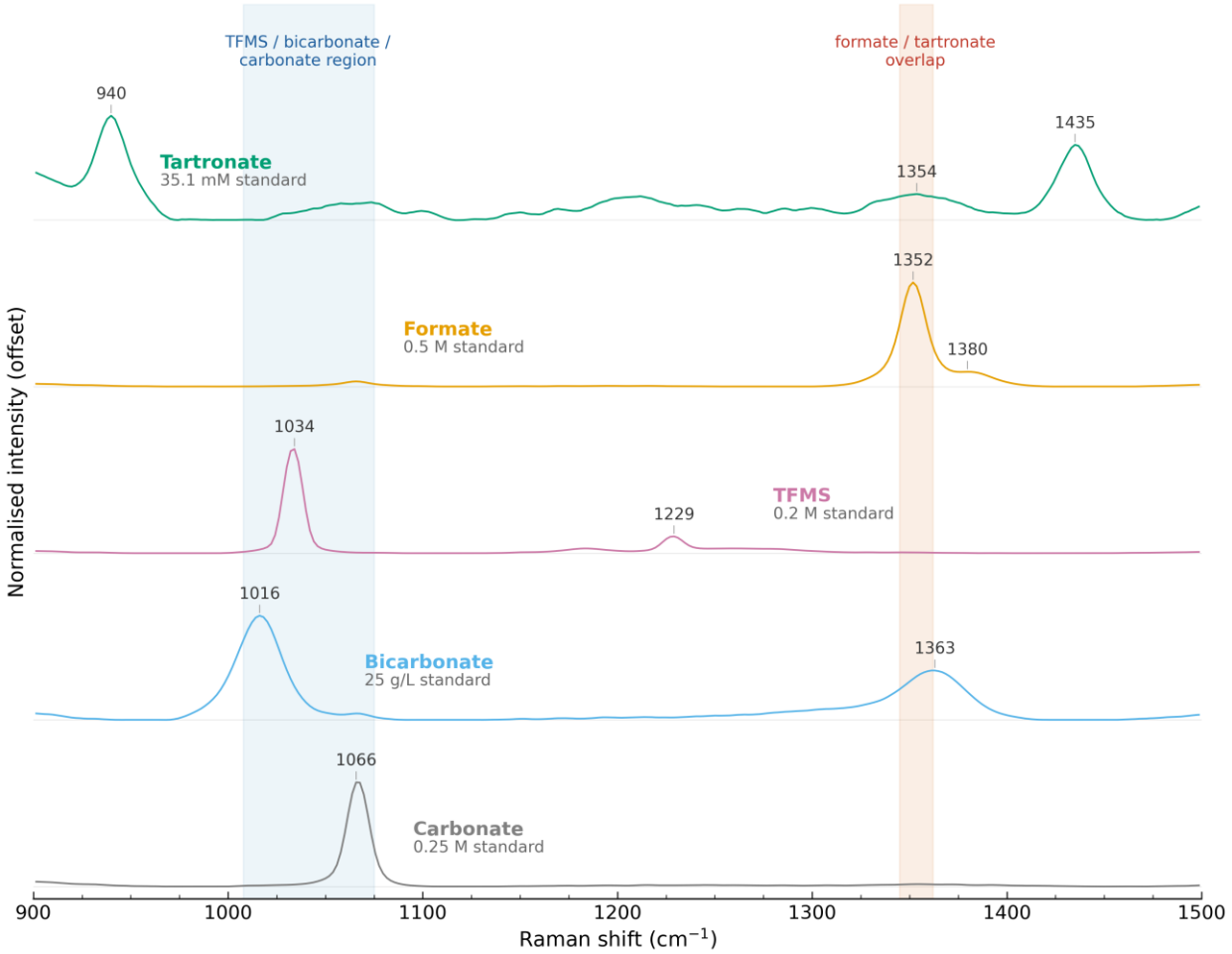

Figure B.2: Raman spectra of the calibration standards over the 900 to 1500 cm^{-1} window used throughout this work, baseline corrected, normalised, and offset for clarity. Band positions are annotated in cm^{-1}. The first shaded region marks the near coincidence of the formate band at 1352 cm^{-1} and the tartronate band at 1354 cm^{-1}, which prevents independent quantification of the two species in the same sample. The second marks the region where bicarbonate, TFMS, and carbonate all scatter.

All spectra in this appendix are processed over the same 900 to 1500 cm^{-1} window used for the sample spectra in the results chapters, so band positions and relative intensities are directly comparable. There are three limitations. First, glycolate has a weak Raman cross-section; although a glycolate standard was prepared and calibrated at 918 cm^{-1} with a coefficient of determination of 0.9975, the band rises above the detection limit only at 0.5 M NaOH and 250 °C, so glycolate is quantified at that single condition and falls below detection elsewhere. Second, the tartronate calibration spans the narrowest concentration range of the set, 15.3 to 35.1 mM, and its coefficient of determination is correspondingly the lowest of the set at 0.9952, so tartronate concentrations

reported near or above the top of that range rely on extrapolation of the fit. Third, the tartronate basis used in the

Appendix C. Construction of the H_2O-NaCl Phase Diagram

The pressure-temperature phase diagram at fixed 3 wt% NaCl bulk composition, corresponding to a mole fraction of 0.00944, was constructed from the correlation formulae of Driesner and Heinrich for phase relations in the H_2O-NaCl system. [39] All equations, parameter values, and notation follow that work. The correlations are valid from 0 to 1000 °C, from 0 to 5000 bar, and across the full composition range. The diagram computed here underlies Figures 4.2 and 4.3.

C.1 Critical Curve

The critical pressure as a function of temperature was computed from Equation 5b of the correlation, valid between the critical temperature of pure water, 373.976 °C, and 500 °C, taking the critical pressure of pure water as 220.549 bar.

$$P_{\mathrm{crit}} = P_{\mathrm{crit}}^{\mathrm{H2O}} + \sum_{n=8}^{11} c_n (T - T_{\mathrm{crit}}^{\mathrm{H2O}})^{cnA} \tag{C.1}$$

The critical composition was computed from Equation 7a.

$$X_{\mathrm{crit}} = \sum_{i=1}^{7} d_i (T - T_{\mathrm{crit}}^{\mathrm{H2O}})^i \tag{C.2}$$

The critical point of the 3 wt% isopleth was located by solving the critical composition relation for the temperature at which it equals 0.00944, which gives 406.6 °C and 297 bar, or 29.7 MPa. The system was operated at 30.0 MPa, just above this pressure, to hold single-phase compressed-liquid conditions in the SIM-AH regime.

C.2 Three-Phase and Coexistence Boundaries

The three-phase vapor-liquid-halite curve was computed from Equation 10, with the sodium chloride triple-point temperature taken as 800.7 °C.

$$P_{\mathrm{VLH}} = \sum_{i=0}^{10} f_i (T / T_{\mathrm{triple,NaCl}})^i \tag{C.3}$$

This curve is univariant in the binary system, having three phases and two components, so it does not depend on bulk composition. At 400 °C the vapor-halite boundary falls at approximately 17.7 MPa, which sets the lower pressure bound for stable two-phase operation in the DAH regime.

The liquid branch of the vapor-liquid coexistence surface was computed from Equation 11.

$$X_{\mathrm{NaCl}}^{\mathrm{VL,liq}} = X_{\mathrm{crit}} + g_0\sqrt{(P_{\mathrm{crit}} - P)} + g_1(P_{\mathrm{crit}} - P) + g_2(P_{\mathrm{crit}} - P)^2 \qquad \text{(C.4)}$$

The leading coefficient of that expression was fixed by boundary conditions: above the critical temperature of pure water the liquid branch passes through the halite liquidus composition at the three-phase pressure, and below it the branch reaches zero NaCl at the boiling pressure of pure water. A smooth Hermite interpolation was applied across a 10 °C window centred on the critical temperature of pure water to join the two limits. The vapor branch above the critical point was obtained from the distribution-coefficient formalism of Equations 12 through 17.

A modified distribution coefficient K' is defined as (Equation 14 of the correlation):

$$\log_{10} K' = \log_{10}(x_{\mathrm{l}}/x_{\mathrm{v}}) + \log_{10}(P_{\mathrm{NaCl}}/P) \qquad \text{(C.5)}$$

where x_{l} and x_{v} are the liquid and vapor compositions, and P_{NaCl} is the sublimation pressure of halite (Equation 2 and Table 3 of the correlation; $b_{\mathrm{subl}} = 1.18061 \times 10^4$). A normalized coefficient $\bar{K}$ is obtained via Equation 15 of the correlation:

$$\log_{10} \bar{K} = [\log_{10} K' - \log_{10} X_{\mathrm{NaCl,sat}}^{\mathrm{L}}|_{P\mathit{NaCl}}] \,/\, [\log_{10}(P_{\mathrm{NaCl}}/P_{\mathrm{crit}}) - \log_{10} X_{\mathrm{NaCl,sat}}^{\mathrm{L}}|_{P\mathit{NaCl}}] \qquad \text{(C.6)}$$

where $X_{\mathrm{NaCl,sat}}^{\mathrm{L}}|_{P\mathit{NaCl}}$ is the halite liquidus composition evaluated at $P = P_{\mathrm{NaCl}}$ as a metastable extension (Section 3.7.2 of that work). A normalized pressure is defined as (Equation 16 of the correlation):

$$\bar{P} = (P - P_{\mathrm{NaCl}}) \,/\, (P_{\mathrm{crit}} - P_{\mathrm{NaCl}}) \qquad \text{(C.7)}$$

The normalized distribution coefficient is fitted as (Equation 17 of the correlation):

$$\log_{10} \bar{K} = 1 + j_0(1 - \bar{P})^{j1} + j_2(1 - \bar{P}) + j_3(1 - \bar{P})^2 - (1 + j_0 + j_2 + j_3)(1 - \bar{P})^3 \qquad \text{(C.8)}$$

with temperature-dependent parameters j_0 through j_3 from Table 8 of the correlation. The vapor composition $X_{NaCl}^{VL,vap}$ is recovered by inverting Equations C.6 and C.5 successively. The V branch was obtained by solving $X_{NaCl}^{VL,vap}(T, P) = 0.00944$ for P at each temperature above T_{CP}. All boundaries were solved numerically for pressure at each temperature using Brent's method.

C.3 Phase Region Nomenclature

The low-density phase is designated V* below 22.1 MPa and SC* above it, reflecting the supercritical transport properties of the water-rich phase above the critical pressure of pure water. The convention is applied to both the two-phase and the halite-bearing regions. The single-phase fluid region above the vapor branch at temperatures beyond the critical point is designated F, following Driesner and Heinrich. [39]

C.4 Validation

The computed boundaries were checked against the Driesner phase equilibrium code at fourteen test conditions chosen to probe the critical point, the vapor branch, and the vapor-halite boundary. The computed phase assemblage agreed with the code at every condition, with no discrepancies (Table C.1).

Table C.1. Validation of computed phase boundaries against the Driesner phase equilibrium code at 3 wt% NaCl (mole fraction 0.00944).

T (°C)	P (bar)	Test purpose	Predicted	Code output
415	250	SC*+L* past CP	V+L	V+L
420	280	SC*+L* past CP	V+L	V+L
430	300	SC*+L* past CP	V+L	V+L
440	350	SC*+L* past CP	V+L	V+L
430	340	Below V branch	V+L	V+L
430	370	Above V branch	Single phase	Single phase
440	370	Below V branch	V+L	V+L
440	400	Above V branch	Single phase	Single phase
450	400	Below V branch	V+L	V+L
450	420	Above V branch	Single phase	Single phase
380	250	L* region	Single phase	Single phase
400	150	Below VLH	V+H	V+H
400	100	Below VLH	V+H	V+H
440	220	Below VLH	V+H	V+H

Appendix D. Fragment Partitioning

An alternative explanation for the incomplete defluorination of PFPrA is that its two-carbon fragment, CHF_2CF_3, partitions from the aqueous phase before reacting. For this to account for the contrast with PFBA, the two-carbon fragment would have to be lost more readily than the three-carbon fragment that PFBA produces. Three lines of evidence bound the contribution of that route: the reported partitioning does not support the required ordering, the operating pressure is above the threshold for a second phase at the concentrations used, and the temperature and NaOH dependence of the defluorination does not follow an equilibrium partitioning limitation.

Reported air–water partitioning data for the 1H-fluoroalkane fragments at 298 K are given in Table D.1. The entries are Henry solubility constants derived from measurements made between 283 and 343 K.[108] The values for the one- and two-carbon fragments are from the same study, so that comparison is internal to one set of measurements rather than assembled across laboratories.

Table D.1: Aqueous partitioning of the 1H-fluoroalkane fragments at 298 K.

Fragment	Formula	H_s^{cp} (mol m^{-3} Pa^{-1})	Solubility at 1 bar (mM)	Basis
C_1	CHF_3	1.3×10^{-4}	13	measured, 283–343 K
C_2	CHF_2CF_3	3.5×10^{-5}	3.5	measured, 283–343 K
C_3 (branched isomer)	CF_3CHFCF_3	1.4×10^{-5}	1.5	measured; not the fragment formed here

No measured constant exists for $CHF_2CF_2CF_3$, the three-carbon fragment formed here. The tabulated C3 value is for the branched isomer CF_3CHFCF_3, produced at commodity scale as a fire-suppression agent. Taking the branched isomer as a proxy, the three-carbon fragment is less soluble than the two-carbon fragment, the partitioning explanation; inverting the ordering would require the linear isomer to be more soluble than the branched isomer by a factor of at least 2.5.

The two-carbon fragment is a factor of 3.6 less soluble than the one-carbon fragment at 298 K. The temperature dependence of the two constants is nearly parallel over the measured range: both fall by a factor of approximately 3.5 between 298 and 343 K, and their ratio changes only from 3.6 to 2.8. The relative ordering is therefore not an artifact of the reference temperature, although the measurements do not extend to reaction conditions.

The partitioning data are measured against a gas phase, which is not present in the heated section. The reactor operates at 25.0 MPa, held by the back-pressure regulator, while the saturation pressure of water is 3.98 MPa at 250 °C and 8.59 MPa at 300 °C; the operating pressure also exceeds the critical pressure of water,[109] 22.06 MPa, so no vapor–liquid boundary is crossed at any subcritical temperature. The bulk fluid is therefore a single compressed liquid from the pump through the hot zone and the cooling section. The one- and two-carbon fragments are nonpolar and above their critical temperatures at reaction conditions, 26.1 and 66.0 °C respectively, so a fragment that leaves solution forms a fluorocarbon-rich phase that is poorly miscible with water.[110] The remaining route to a second phase is demixing of the water–fluoroalkane binary, and the concentrations are below that threshold by more than an order of magnitude. This bulk estimate does not fix the local state, since the fragment concentration near a decomposing parent exceeds the bulk average. Demixing is therefore a competing loss channel that fast reaction can outrun, not a route excluded by an equilibrium margin. The fragment forms dissolved and exposed to NaOH. It can react and defluorinate, or separate from the water as this immiscible phase and leave unreacted, with any fraction still dissolved released at the back-pressure regulator on depressurization.

Fluoride recovery is then set by the base-assisted elimination against the contact time. A fragment that does not react within the contact time separates or is released on depressurization and is not

recovered as fluoride. Two observations distinguish this from a partitioning limitation. At unchanged NaOH loading, PFPrA defluorination increases from 41% at 250 °C to 78% at 275 °C and 89% at 300 °C, the direction opposite to that expected if fragment volatility limited recovery, and defluorination also increases with NaOH loading at fixed temperature. Neither response is available to a fragment that has left the liquid. The same contrast appears outside hydrothermal conditions: in NaOH-amended water–DMSO at 80 to 120 °C and ambient pressure, PFBA gives quantitative fluoride recovery while PFPrA gives 3.9 ± 1.6%, with CF_3CF_2H identified in the headspace.[76] A partitioning mechanism specific to the phase behavior of this reactor does not account for the same deficit in a system with neither elevated pressure nor a back-pressure regulator.

The barrier difference computed above accounts for the observation directly. Base-assisted elimination from CHF_2CF_3 has a barrier of 29.9 kcal/mol against 22.4 kcal/mol for $CHF_2CF_2CF_3$, and the C_2 elimination is essentially thermoneutral where the C_3 elimination is strongly exergonic. The two-carbon fragment is lost not because it separates more readily than the others, since it does not, but because it reacts too slowly to be consumed before it separates.

Appendix E. Gas-Phase Intermediates at Sub-Stoichiometric Hydroxide

The gas phase of both acids was analysed by full-scan GC-MS at a sub-stoichiometric hydroxide loading, at which the cascade stalls and its intermediates accumulate. The two experiments used the same reactor, the same acid and NaOH concentrations, the same temperature, and the same acquisition method. The minor products of PFBA are given below; none of them was detected in the PFPrA experiment.

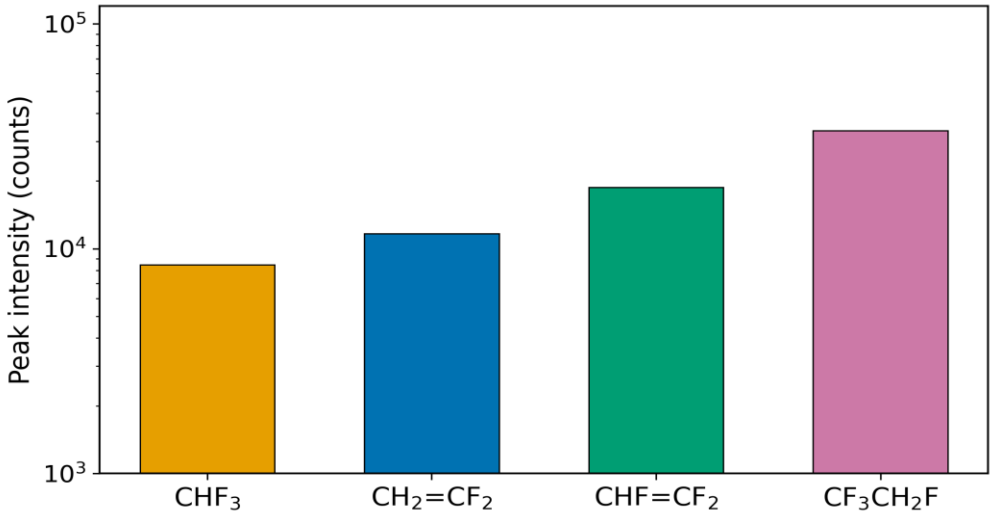

Figure E.1: Minor gas-phase products of PFBA detected by full-scan GC-MS at sub-stoichiometric hydroxide, 0.05 M PFBA in 0.1 M NaOH at 250 °C. Peak intensity of the quantifying ion: m/z 51 for CHF_3, 64 for $CH_2{=}CF_2$, 82 for $CHF{=}CF_2$, and 83 for CF_3CH_2F. The three two-carbon species carry hydrogen, so their formation requires that hydroxide reopened the saturated fragment. None of them is present for PFPrA under matched conditions. C_3F_7H is omitted because it is the dominant peak and exceeds this scale.